

MINI-/MICRO-SCALE FREE SURFACE PROPULSION

by

Junqi Yuan

B.S. in Thermal Engineering, Shanghai Jiao Tong University, 2002

M.S. in Thermal Engineering, Shanghai Jiao Tong University, 2005

Submitted to the Graduate Faculty of
Swanson School of Engineering in partial fulfillment
of the requirements for the degree of
Doctor of Philosophy

University of Pittsburgh

2015

UNIVERSITY OF PITTSBURGH
SWANSON SCHOOL OF ENGINEERING

This dissertation was presented

by

Junqi Yuan

It was defended on

January 29, 2015

and approved by

Minking K. Chyu, PhD, Leighton and Mary Orr Chair Professor,
Department of Mechanical Engineering and Materials Science

Laura Schaefer, PhD, Professor,

Department of Mechanical Engineering and Materials Science

Youngjae Chun, PhD, Assistant Professor,

Department of Industrial Engineering, Department of Bioengineering

Dissertation Director: Sung Kwon Cho, PhD, Associate Professor,

Department of Mechanical Engineering and Materials Science

Copyright © by Junqi Yuan

2015

MINI-/MICRO-SCALE FREE SURFACE PROPULSION

Junqi Yuan, PhD

University of Pittsburgh, 2015

This work reports theoretical studies and experimental proofs of the propulsion of mini-/micro-scale floating objects that propel on air-liquid interface by using two different principles. The devices are extremely simple and do not include any moving parts.

The first principle takes advantage of three-phase contact line oscillation that is activated by AC electrowetting on dielectric (EWOD) to propel the floating object. The capillary wave that is generated by the free surface oscillation is visualized by using the Free-Surface Synthetic Schlieren (FS-SS) method. A 3-D flow field sketch is constructed based on the flow visualizations and PIV measurements. The flow field and trajectories of seeded particles suggest that Stokes drift is the responsible mechanism for the propulsion. The propulsion speed of the floating object highly depends on the amplitude, frequency, and shape of the EWOD signal. These phenomena are also explained by the measured oscillation amplitudes and Stokes drift relations. Additionally, it is shown that a wider EWOD electrode generates a faster propelling speed. Finally, with stacked planar receiver coils and an amplitude modulated signal, a wirelessly powered AC EWOD propulsion is realized.

The second principle of floating object propulsion is the Cheerios effect, which is also generally known as lateral capillary force. Four common physical configurations (interactions between two infinite vertical walls, two vertical circular cylinders, two spheres, and a sphere and a vertical wall) are reviewed. Through theoretical analysis, it has been revealed that not the wettability of the surface but the slope angle of the object is the most important parameter for the

Cheerios effect. A general rule for this effect is that the lateral capillary force is attractive if the slope angles of the interacting objects have the same sign, otherwise the force is repulsive. In addition to the surface wettability, the size and the density of floating spheres are also important for the slope angle. Active control of the Cheerios effect is achieved by implementing EWOD and dielectrowetting methods to adjust the surface wettability. By sequentially activating micro-fabricated EWOD/dielectrowetting electrodes, linear translations of floating objects in the small scale channel are accomplished. A continuous rotational motion of the floating rod is achieved in a circular container by the EWOD method.

TABLE OF CONTENTS

NOMENCLATURE.....	XIV
1.0 INTRODUCTION.....	1
1.1 PROPULSION OF NATURAL CREATURES	1
1.1.1 $Mg/(\gamma Pc) > 1$	2
1.1.2 $Mg/(\gamma Pc) < 1$	3
1.2 BIO-INSPIRED DEVICES.....	6
2.0 AC EWOD PROPULSION	11
2.1 ELECTROWETTING ON DIELECTRIC (EWOD).....	11
2.1.1 EWOD principle.....	11
2.1.2 AC EWOD	14
2.2 EXPERIMENTAL SETUP.....	17
2.3 PROPULSION AND MECHANISM.....	19
2.3.1 Propulsion test.....	19
2.3.2 Flow visualizations and propulsion mechanism.....	22
2.3.3 Stokes drift and parameter effects	27
2.3.3.1 Effect of signal frequency	28
2.3.3.2 Effect of signal amplitude.....	30
2.3.3.3 Effect of EWOD signal shape.....	32

2.3.3.4	Effect of electrode width.....	34
2.4	WIRELESS PROPULSION	35
2.4.1	Wireless EWOD	36
2.4.2	Experiment	38
2.5	SUMMARY	41
3.0	PROPULSION BY CHEERIOS EFFECT	43
3.1	THEORETICAL MODELS	44
3.1.1	Model of two infinite vertical plates	46
3.1.2	Model of two vertical cylinders.....	52
3.1.2.1	Cylinders spaced at a small or moderate separation	53
3.1.2.2	Cylinders spaced at a large separation	56
3.1.3	Model of two floating spherical particles.....	60
3.1.4	Model of floating spherical particle and vertical wall.....	64
3.1.4.1	Fixed contact angle at the wall.....	68
3.1.4.2	Fixed contact line at the wall.....	70
3.2	ELECTROWETTING-ASSISTED CHEERIOS EFFECT.....	75
3.2.1	Theory validation	75
3.2.2	EWOD-assisted propulsion	82
3.3	DIELECTROWETTING-ASSISTED CHEERIOS EFFECT	88
3.4	SUMMARY	94
4.0	CONCLUSION REMARKS	97
	BIBLIOGRAPHY	100

LIST OF FIGURES

Figure 1. Side and top view images of a basilisk lizard running across free surface[7].....	2
Figure 2. Flow generated by the stroke of a water strider[4]. (a) & (b) Side and top view images of a stroke; (c) Schematic illustration of the flow structures generated by the driving stroke.3	3
Figure 3. Meniscus climbing behavior of the water lily leaf beetle[28].	5
Figure 4. Artificial water-walkers. Re is the Reynolds number.	6
Figure 5. Bio-inspired water walkers. (a), [35]; (b), [4]; (c), [36]; (d), [3]; (e), [37]; (f), [38].....	7
Figure 6. Principle of electrowetting on dielectric. (a) Schematic configuration. The dashed line represents the droplet original shape; the solid line denotes the droplet shape after actuation. (b) Snapshots of basic electrowetting demonstration on a sessile drop.	12
Figure 7. Equivalent circuit diagram for sessile droplet EWOD setup.....	13
Figure 8. Contact angle of a sessile droplet under DC or AC electrowetting[53]. The rectangular and circular symbols correspond to the cases of DC and AC ($f = 10$ kHz), respectively. The solid line represents the Lippmann-Young equation (Eqn. (2-3)).	13
Figure 9. Patterns of droplet oscillation that are obtained by overlapping more than 50 images at 100 V for resonance frequencies[59].	15
Figure 10. Frequency dependence of flow pattern under AC electrowetting[53].	16
Figure 11. EWOD electrode at vertical wall. θ_0 is the initial contact angle at the wall; θ denotes the contact angle after DC signal applied. Another electrode without dielectric layer covered is inserted into water to form a closed electric circuit.....	17
Figure 12. Illustration of AC EWOD propulsion. The EWOD and bare ground electrodes are installed at the stern and bottom of the boat, separately.	18
Figure 13. (a) EWOD electrode configuration; (b) Fabricated boat with EWOD and ground electrodes installed. The inset shows the side and bottom of the boat. (c) Experimental setup of AC EWOD propulsion.	19

Figure 14. AC EWOD propulsion in stationary water. Two snapshots before and after actuation are overlapped to compare the positions. (a) Linear motion; (b) Rotation; (c) Steering. A boat with a rectangular shape (30 (L) × 10 (W) × 10 (H) mm ³) is used for (b)&(c).	20
Figure 15. AC EWOD propulsion in a wave tank. (a) Wave tank and stepper motor; (b) Snapshot superposition of boat propulsion on wave surface. A standing wave is generated in the water tank. Dashed lines show overlapped profiles of the standing wave.....	21
Figure 16. Visualization of surface waves close to the EWOD electrode by FS-SS method (f = 10 Hz, V = 100 VRMS).	22
Figure 17. (a) Surface flow visualization (top view, exposure time = 0.6 s); (b) Trajectories of two particle tracers in the center plane behind the boat recorded by a high-speed camera. The amplitude of the wave is not scaled. The inset shows magnified and digitized traces.	23
Figure 18. Velocity field measurement: (a) PIV measurement in the centerline of the wake; (b) PIV measurement 10 mm downstream from the EWOD electrode (boat stern).	24
Figure 19. 3-D flow field sketch based on the measurements.	25
Figure 20. (a) Oscillation amplitude of the contact line vs. EWOD frequency (the broken line is a power series fit, V _{total} = 100 VRMS, h = 10 mm, b = 10 mm with sinusoidal EWOD signal); (b) Boat speed vs. frequency (the broken line is a curve fit by Eqn. (2-10), V _{total} = 100 VRMS, h = 10 mm, b = 10 mm with sinusoidal EWOD signal); (c) Response of the contact line to an EWOD step voltage; and (d) Positions of the contact line when an AC EWOD is applied. The right figure is the magnified image to show the position and movement of the contact lines.	28
Figure 21. (a) Oscillation amplitude of the contact line vs. EWOD voltage V _{total} (the broken line is a Fourier series fit, f = 100 Hz, h = 10mm, b = 10 mm with sinusoidal EWOD signal); (b) Boat speed vs. signal voltage (the broken line is a curve fit by Eqn. (2-10), f = 100 Hz, h = 10mm, b = 10 mm with sinusoidal EWOD signal); and (c) Contact angle saturations for two sinusoidal signals with different amplitude.....	31
Figure 22. (a) Oscillation amplitude of the contact line for three signal shapes vs. frequency. (V _{total} = 100 VRMS, h = 10 mm, b = 10 mm); and (b) Boat speed for three signal shapes vs. frequency. The lines are curve fits by Eqn. (2-10).....	33
Figure 23. Effect of electrode width. (Sinusoidal signal, V _{total} = 100 VRMS, h = 10 mm)	34
Figure 24. Sketch of wireless AC EWOD propulsion system.	35
Figure 25. Wireless EWOD principle[83]. (a) Schematic of EWOD wireless powering using inductive coupling; (b) The receiver coil and the transmitter coil; (c) Voltage at the receiver.....	36
Figure 26. Planar type wireless EWOD[84]. (a) Planar type receiver together with EWOD electrodes; (b) Voltage at the receiver side without droplet.	37

Figure 27. (a) Microfabrication process flow of planar coils on PCB. Cu layer (15 μm) on top of 1.5 mm of board thickness is patterned by photolithography process and wet-etched. (b) A photo of fabricated planar coils. (c) A photo of transmitter coil. The wire (diameter $\sim 250 \mu\text{m}$) is wound around air-cored ferrite rings. 38

Figure 28. Boat for wireless EWOD propulsion. (a) EWOD electrodes and ground electrode installed on boat; (b) Photo of wireless EWOD boat with receiver circuit installed. 39

Figure 29. An equivalent electric circuit using magnetic induction. L_{tr} and C_{tr} is the inductance and capacitance of the transmitter. L_{re} and C_{re} is the inductance and capacitance of the receiver. 39

Figure 30. Photo of wireless boat propulsion setup. 40

Figure 31. Snapshot superposition of wireless EWOD propulsion. The inset represents the signal applied to wireless boat. 40

Figure 32. Configuration of two infinite vertical plates partially submerged in liquid[86]. The contact angles on the two plates are θ_1 and θ_2 . The separation distance between the two plates is L 47

Figure 33. Two vertical plates submerged in water with similar wettability. (a) Interface profiles near two hydrophilic plates; and (b) two hydrophobic plates. (c) Horizontal component of the dimensionless force between the plates vs. separation ($\theta_1 = 45^\circ$ and $\theta_2 = 60^\circ$). In (a) and (b), the thick solid lines represent the plates; the black dashed line denotes the water level at infinity; and the thin solid lines denote the distorted air-water interface. 49

Figure 34. Two vertical plates with opposite surface wettability and $\theta_1 + \theta_2 \neq 180^\circ$. Interface profiles for (a) a moderate separation; and (b) a small separation between the plates. (c) Horizontal component of the dimensionless force between the plates vs. separation ($\theta_1 = 45^\circ$ and $\theta_2 = 120^\circ$). In (a) and (b), the thick solid lines represent the plates; the black dashed line indicates the liquid level at infinity; and the thin solid lines denote the distorted air-water interface. 50

Figure 35. Two vertical plates submerged in water with opposite surface wettability and $\theta_1 + \theta_2 = 180^\circ$. (a) Interface profile; (b) horizontal component of the dimensionless force vs. separation ($\theta_1 = 45^\circ$ and $\theta_2 = 135^\circ$). In (a), the thick solid lines represent the plates; the black dashed line indicates the liquid level at infinity; and the thin solid lines denote the distorted air-water interface. 51

Figure 36. (a) Configuration of two vertical cylinders partially submerged in liquid[97]; (b) Bipolar coordinates on plane xy [96]. 52

Figure 37. Contact line on the left cylinder when the separation between the two cylinders is small[97]. The second cylinder is located on the right (not shown). 55

Figure 38. Comparison of theoretical predictions with experimental data for the dimensionless horizontal force between two vertical cylinders. Both cylinders are lyophilic (a) Both

cylinders are partially submerged in water; (b) Both cylinders are partially submerged in an 8×10^{-2} M SDS solution. The dash-dot lines show the lower limit for possible separation between the cylinder centers. ($\theta_1 = \theta_2 = 0^\circ$, $r_1 = 370 \mu\text{m}$, $r_2 = 315 \mu\text{m}$, $\gamma_w = 72.4 \text{ mN/m}$, $\rho_w = 1.0 \text{ g/cm}^3$, $\gamma_{\text{SDS}} = 36.8 \text{ mN/m}$, and $\rho_{\text{SDS}} = 1.01 \text{ g/cm}^3$) 58

Figure 39. Comparison of theoretical predictions and experimental data for the horizontal force between two vertical cylinders partially submerged in water. The two cylinders have the opposite wettability. The dash-dot line shows the lower limit for possible separation between the cylinder centers. ($\theta_1 = 0^\circ$, $\theta_2 = 99^\circ$, $r_1 = 370 \mu\text{m}$, $r_2 = 315 \mu\text{m}$, $\gamma_w = 72.4 \text{ mN/m}$) 59

Figure 40. (a) Configuration of two small spherical particles floating at the air-liquid interfaces[97]; (b) The two fictitious cylinders generate the same interface profiles[97].60

Figure 41. Horizontal force vs. separation for three pairs of spherical particles with different densities. The particle sizes and contact angles are kept constant in calculation ($R_1 = R_2 = 100 \mu\text{m}$, $\theta_1 = \theta_2 = 60^\circ$). The dash-dot line shows the lower limit of possible separation between the centers of the particles. 63

Figure 42. Capillary image force between the floating particle and its image[102]. (a) Fixed contact angle at the wall ($\theta_w = 90^\circ$); (b) Fixed contact line at the wall ($\xi_0(0) = 0$). 64

Figure 43. Configuration of the spherical particle and vertical wall[102]. The particle can be modeled and analyzed using the fictitious cylinder. 66

Figure 44. Horizontal force vs. separation in the wall-sphere capillary interaction for different wall contact line elevations. (a) Buoyant sphere ($\rho_f = 0.58 \text{ g/cm}^3$, $R_f = 1 \text{ mm}$, $\theta_f = 45^\circ$); (b) Dense sphere ($\rho_f = 1.18 \text{ g/cm}^3$, $R_f = 1 \text{ mm}$, $\theta_f = 45^\circ$). The dash-dot lines show the smallest separation between the particle center and wall. 73

Figure 45. Horizontal force vs. separation in the wall-sphere capillary interaction for different wall contact angles. (a) Buoyant sphere ($\rho_f = 0.58 \text{ g/cm}^3$, $R_f = 1 \text{ mm}$, $\theta_f = 45^\circ$); (b) Dense sphere ($\rho_f = 1.18 \text{ g/cm}^3$, $R_f = 1 \text{ mm}$, $\theta_f = 45^\circ$). The dash-dot lines show the smallest separation between the particle center and wall. 74

Figure 46. Comparison of experimental data and theoretical prediction of the zero force point for fixed contact angle boundary condition. Separation s is equal to R_f . Contact angle and radius of sphere θ_f and r_f are 45° and 1 mm for both experiment and calculation..... 77

Figure 47. Sketch of EWOD-assisted Cheerios effect. (a) & (b) Floating sphere with a positive slope angle. (a) EWOD is OFF; (b) EWOD is ON. (c) & (d) Floating sphere with a negative slope angle. (c) EWOD is OFF. (d) EWOD is ON..... 78

Figure 48. Experimental results for EWOD-assisted Cheerios effect. (a) When EWOD is ON, buoyant sphere is attracted but dense sphere is repelled; (b) When EWOD is OFF, buoyant sphere is repelled but dense sphere is attracted. 79

Figure 49. Sketch of EWOD-assisted Cheerios effect with an EWOD electrode installed on the floating object. (a) & (b) Hydrophobic vertical wall. (a) EWOD is OFF; (b) EWOD is ON. (c) & (d) Hydrophilic vertical wall. (c) EWOD is OFF; (d) EWOD is ON. 80

Figure 50. Experimental setup of EWOD-assisted cheerios effect propulsion with an EWOD electrode installed on the boat. The red dashed line shows the vertical wall. An aluminum foil is attached at the bottom of the container as the ground electrode. The inset shows a floating boat used in the experiment. An EWOD electrode is attached at one sidewall of the boat. A thin copper wire (30 μm in diameter) is used as connection wire. 81

Figure 51. Experimental results for the EWOD-assisted cheerios effect propulsion with an EWOD electrode installed on the boat. (a) & (b) Hydrophobic vertical wall ($\theta_w > 90^\circ$). (a) EWOD is OFF; (b) EWOD is ON. (c) & (d) Hydrophilic vertical wall ($\theta_w < 90^\circ$). (c) EWOD is OFF; (d) EWOD is ON. Yellow dashed line represents initial position while red dashed line is ending position. Thick white arrow indicates floating object moving direction.... 82

Figure 52. Comparison of Cheerios effect propulsion methods. (a) Boat is attracted toward or repelled against the wall; (b) Boat propulsion in a small channel; (c) 3-D sketch of EWOD-assisted Cheerios effect continuous propulsion. In (b) and (c), the boats have positive slope angles. 83

Figure 53. Boat with positive slope angle propelling in a 15 mm wide channel. Pairs of electrodes were activated sequentially from right to left with duration of 1 s. Red bars indicate the activated EWOD electrodes. 84

Figure 54. Fabrication process flows for EWOD electrodes on (a) SiO₂ chip; (b) ITO glass chip. 85

Figure 55. Boat with positive slope angle propelling in two directions in a small channel with microchips. Duration of activation was 0.5 s for each pair of electrodes. 86

Figure 56. Rotation in a 24 mm radius circular container. Pairs of diagonal electrodes were activated clockwise with duration of 1.5 s. White bars indicate the activated EWOD electrodes. 87

Figure 57. Sketch of dielectrowetting setup. (a) Side view; (b) Top view. Dashed line represents droplet original shape; solid line denotes droplet shape after actuation. 88

Figure 58. (a) Fabrication process flow of dielectrowetting electrodes; (b) Side and top view images of droplet actuated by dielectrowetting ($V = 300 \text{ VRMS}$, $f = 10 \text{ kHz}$); (c) Contact line climbs vertically submerged dielectrowetting electrodes ($V = 300 \text{ VRMS}$, $f = 10 \text{ kHz}$). 89

Figure 59. Sketch of dielectrowetting-assisted Cheerios effect. (a) & (b) Floating object with a positive slope angle. (a) Signal is OFF; (b) Signal is ON. (c) & (d) Floating object with a negative slope angle. (c) Signal is OFF. (d) Signal is ON. 90

Figure 60. Experimental results for dielectrowetting-assisted Cheerios effect. Floating object with a positive slope angle is repelled when dielectrowetting signal is OFF ((a)) and is attracted when signal is ON ((b)); Floating object with a negative slope angle is attracted when signal is OFF ((c)) and is repelled when signal is ON ((d)). 91

Figure 61. Force/object mass vs. tilting angle β . (a) Theoretical prediction; (b) Experimental result. ($V = 300$ VRMS, $f = 10$ kHz) 92

Figure 62. Force/object mass vs. applied voltage. (a) Theoretical prediction; (b) Experimental result. ($f = 10$ kHz, $\beta = 30^\circ$)..... 92

Figure 63. (a) 3-D sketch of dielectrowetting-assisted Cheerios effect continuous propulsion; (b) Top view snapshots of continuous propulsion in a channel. Pairs of electrodes are activated sequentially from right to left with duration of 0.7 s. ($V = 300$ VRMS, $f = 10$ kHz, $\beta = 30^\circ$) 93

NOMENCLATURE

A	Wave amplitude
A_{boat}	Projected area of submerged boat part
b	Width of EWOD electrode
C_d	Specific capacitance of the dielectric layer
C_D	Drag coefficient
C_{re}	Capacitance of the external capacitor at receiver side
C_{tr}	Capacitance of the external capacitor at transmitter
d	Distance from the cylinder axis
D_i	Density correlation
f	Frequency
F	Force
F_{drag}	Drag force
F_g	Gravitational force
F_{prop}	Propulsion force
g	Gravitational acceleration
h	Water depth
h_i	Contact line elevation
H	Air-liquid interface level or contact line elevation
k	Wave number
L	Separation distance
L_0	Separation distance for zero force point
$L_c = q^{-1} = \sqrt{\gamma_{al}/\Delta\rho g}$	Capillary length
L_{re}	Inductance of the receiver coil
L_{tr}	Inductance of the transmitter coil
M	Mass
P	Pressure
P_c	Contact perimeter of the water-walker

Q	Capillary charge
r	Radius of contact line
R	Radius of sphere
s	Separation distance from vertical axis
s_0	Separation distance for zero force point
t_d	Thickness of dielectric layer
u_{boat}	Propulsion speed of the boat
u_{drift}	Drift velocity
V_l and V_u	Volume of the lower part and upper part of the sphere
V_d	Voltage across the dielectric layer
V_{total}	Total voltage applied to the EWOD system
z	Vertical position
ΔP	Pressure difference across the air-liquid interface
$\Delta\rho = \rho_l - \rho_a$	Density difference between air and liquid
ϵ_0	Vacuum permittivity (8.854×10^{-12} F/m)
ϵ_r	Relative permittivity of the dielectric layer
γ	Surface tension (default is air-water surface tension)
γ_{sl}^0	Initial solid-liquid surface tension with no voltage
θ_0	Initial contact angle with no voltage applied
θ	Contact angle
$\xi(x, y)$	Function describing the shape of the interface
ρ	Density
ω	Angular frequency
$\nabla_{II} \equiv \frac{\partial}{\partial x} \mathbf{e}_x + \frac{\partial}{\partial y} \mathbf{e}_y$	Two-dimensional gradient operator
Subscript a	Air
Subscript g	Gas
Subscript l	Liquid
Subscript s	Solid
Subscript w	Water

1.0 INTRODUCTION

Around 70 percent of the surface area of our planet is covered by water. People utilize creeks, rivers, lakes and oceans for a wide variety of living activities, such as transportation, fishing, and entertainment. However, human beings cannot survive in the water without tools. To be able to float on the water and move freely, people contrive and manufacture vessels in a wide size range, from tiny to huge, and equip them with propulsion devices, such as oar, sail, propeller, and air fan. Recently, interest has been increasing in using small floating robots for environment monitoring systems[1], surveillance security systems[2], educational robots, and toys.

In nature, there are a number of animals living or spending part of their lives at the surface of water, and many of these animals are able to walk on water. Recently, as the floating and propulsion mechanisms of these animals have been elucidated and the demand for small floating robots is increased, there has been an increasing interest in designing bio-inspired min/micro-robots to achieve certain goals, such as power efficiency, high speed, and silent movement[3].

1.1 PROPULSION OF NATURAL CREATURES

Depending on the ratio of the body weight Mg and the interfacial force γP_c , where M is the body mass of the water-walker, g the gravitational acceleration, γ the air-water surface tension, and P_c

the contact perimeter of the water-walker, walking and propelling of different animals on water can be divided into two categories[4]: water-walkers, characterized by $\frac{Mg}{\gamma P_c} > 1$, which are typically in decimeter or millimeter scale, such as sea birds and basilisk lizards, rely on the buoyancy force or the force generated by their feet repeatedly slapping and stroking downwards to support their body weight[5]; smaller creatures with $\frac{Mg}{\gamma P_c} < 1$, such as water striders, are supported by the surface tension[6] and use various propulsion methods.

1.1.1 $Mg/(\gamma P_c) > 1$

Creatures such as ducks and sea birds that live at the air-water interface and have a large ratio of body weight to interfacial force generally support their body weight by the buoyant force. These animals typically propel themselves by paddling. Some other animals, such as basilisk lizards, lift themselves by repeatedly striking the water surface with their feet. Figure 1 shows high-speed snapshots of water walking behavior of a basilisk lizard. Each stride of the lizard can be divided into four phases[7]: slap, stroke, recovery-up and recovery-down. An in-depth study[5] and time-averaged force measurements[8] showed that the majority of the weight support of basilisk lizards

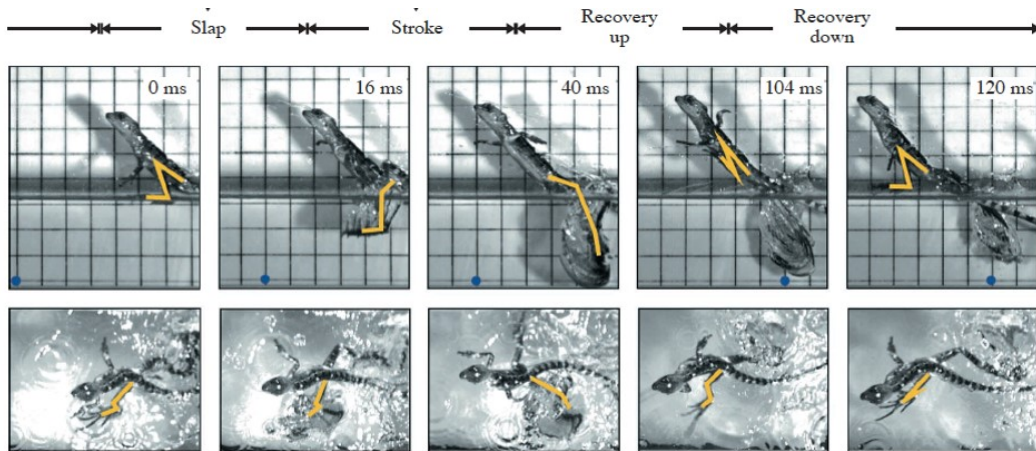


Figure 1. Side and top view images of a basilisk lizard running across free surface[7].

comes from stroking the foot vertically downwards into the water and expanding an underwater air cavity, rather than from slapping the water surface. Glasheen and McMahon[9] studied the relationship between the size of a basilisk lizard body and its water-walking ability. They found that large lizards can just barely support their body weight, but much smaller lizards can generate the upward force twice as much as their body weight.

1.1.2 $Mg/(\gamma Pc) < 1$

For water-walkers with small mass M , the body weight can be counterbalanced by surface tension[6]. As one of the most common examples, water striders can stand effortlessly due to water repellency and move quickly on water. Recent research showed that the water repellency is mainly created not by the wax that covers legs[10], but by the superhydrophobic effect caused by a large number of

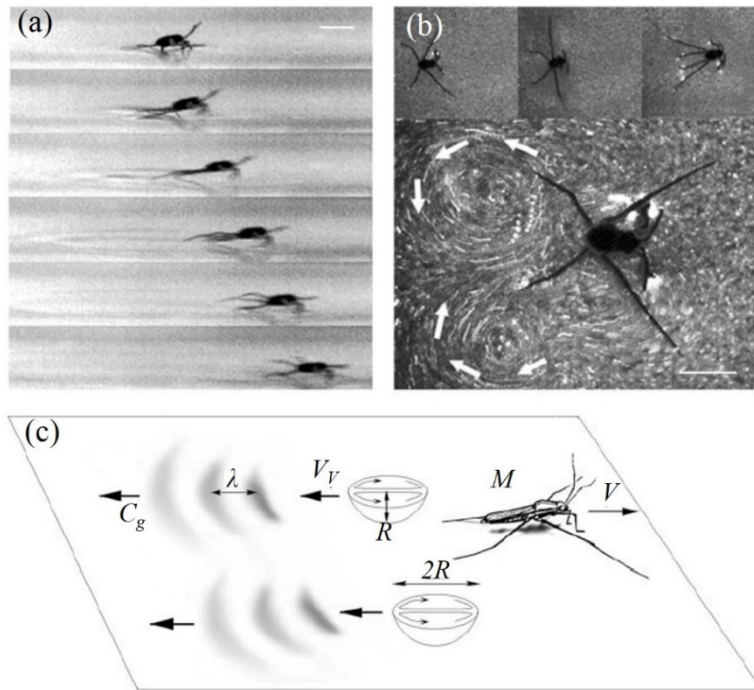


Figure 2. Flow generated by the stroke of a water strider[4]. (a) & (b) Side and top view images of a stroke; (c) Schematic illustration of the flow structures generated by the driving stroke.

oriented tiny hairs (micro-setae) with fine nano-structures[11-13]. Flexibility of the legs[14], adhesion energy[15], and hair density[15] were found to be important for the water repellency of the legs. Tilted, flexible hairs can facilitate locomotion by interacting with the water surface and generating directionally anisotropic adhesive forces[16].

Water striders perform two kinds of movements at the air-water interface: gliding and leaping[17]. By studying the flow generated by the driven stroke of the water strider, as shown in Fig. 2, Hu *et al.* [4] found that the strider transfers momentum to the underlying fluid not primarily through capillary waves, but rather through hemispherical vortices shed by its driving legs. Nevertheless, by simplifying the leg stroke into an impulsive point force, Bühler[18] found that both wave momentum and vortices momentum are significant, and share the horizontal momentum by 1/3 and 2/3, respectively. Gao and Feng[19] suggested that small water striders rely on vortices, whereas large ones may rely more on surface waves. Hu and Bush[20] proposed two principal modes of propulsion available to small water-walkers: (1) when driving leg speed is greater than the capillary wave speed, interfacial forces are generated by the deformed water surface for the surface locomotion; (2) for the slower leg speed, the propulsion force comes from the contact or viscous forces acting on the leg hairs when legs brush the water surface.

Fishing spiders propel themselves across the water surface using two gaits[21]: rowing with four legs at speed below 20 cm/s and galloping with six legs at speed above 30 cm/s. Suter and Wildman[21] concluded that hydrodynamic and anatomical constraints, including disintegration of the dimple, the weight of spider, and the substantial drag experienced by the spider during the glide interval between power strokes, confine rowing spiders to sustained velocities lower than 30 cm/s, and that galloping allows spiders to move considerably faster due to the freedom from these constraints.

Fishing spiders sometimes jump to avoid predators[22, 23]. Jumping height and duration were found to be similar for fishing spiders with different mass[22]. Fishing spiders also sometimes take advantage of air movement to ‘sail’ on the water surface[24, 25]. They extend their bodies and elevate themselves to appropriate height above the free surface depending on the air speed to utilize the aerodynamics forces for propulsion[25].

Terrestrial snails transmit waves of shear stress through a thin layer of mucus to walk on solid surface[26]. Since a free surface cannot support such shear stress, water snails use a different mechanism to crawl upside down on the surface. They deform the water surface with their foot to generate curvature pressures and lubrication flows inside the mucus layer at the free surface to crawl beneath it[27].

A lot of water-walking animals spend not entire but some of their lives in or on water. When they want to move from water to land, they need to pass the meniscus at the bank. However, millimeter-scale water-walkers are unable to climb menisci using their typical propulsion methods such as sliding their limbs[6]. Normally these small animals climb meniscus by capillary force, which is created by deformed water surface with their certain body postures, such as arching the back, as shown in Fig. 3, and thus do not need to move their appendages to achieve movement[28]. This phenomenon, which is also known as the Cheerios effect, will be discussed in detail in Chapter 3.

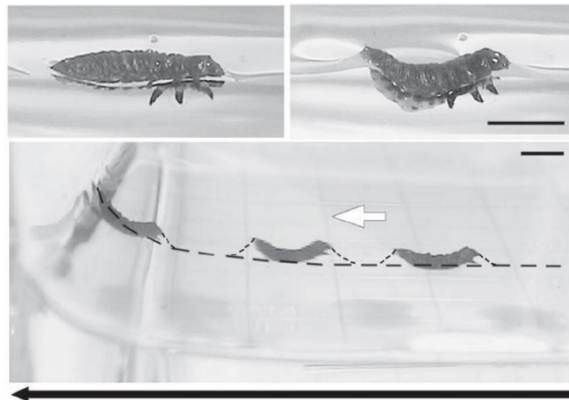


Figure 3. Meniscus climbing behavior of the water lily leaf beetle[28].

There are some insects, such as *Microvelia*[29], that can release some surfactant to create a surface tension gradient at the three-phase contact line and realize mass transfer, which is called the Marangoni effect. As a result, they can propel themselves at the free surface in emergency situations[29].

1.2 BIO-INSPIRED DEVICES

Since nature is the best teacher, the uncovered propulsion principles from the natural creatures may facilitate the development of the water-walking robots. Fast, durable, high load capacity, untethered and remote controllability, and high power efficiency are desirable properties for the future devices. To date, a large number of attempts have been made to mimic the propulsion methods of natural creatures mentioned in the previous section. Figure 4 shows some of the works on development of bio-inspired propelling devices in the domain of the Reynolds number (= propelling speed \times

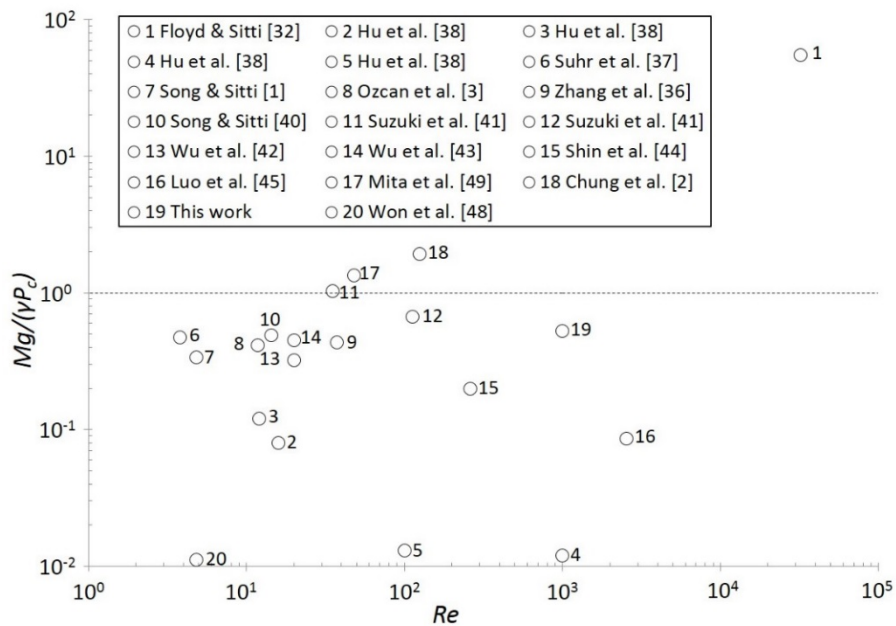


Figure 4. Artificial water-walkers. Re is the Reynolds number.

characteristic dimension / kinematic viscosity of water) and $\frac{Mg}{\gamma P_c}$. Roughly, the developed devices fall in the range of 1-1000 in Re and 0.01 – 10 in $\frac{Mg}{\gamma P_c}$. Interestingly, $\frac{Mg}{\gamma P_c}$ in the majority of the devices is smaller than 1. This may be because the case of $\frac{Mg}{\gamma P_c} > 1$ requires more precise dynamic and complex structures and sophisticated control algorithms to overcome the gravity and drowning.

One of the representative devices for $\frac{Mg}{\gamma P_c} > 1$ is to mimic the walking manner of basilisk lizards. Floyd *et al.* [30] introduced a robot prototype that can run on the water surface by two or four feet slapping and stroking into the water. They later optimized the foot design[31] and suggested the use of a four-legged robot instead of two-legged one for better stability and higher lift-to-power ratio[32]. Park *et al.* [33, 34] built a dynamic model for the previous robot and analyzed the effects of running frequency and tail types for stability. Park *et al.* [35] later improved the robot with a circular tail, which is shown in Fig. 5(a), and achieved stable running on water.

It is easy to find numerous water walking devices for $\frac{Mg}{\gamma P_c} < 1$. Takonobu *et al.* [39] studied the muscle arrangement of water striders and designed a walking robot based on the water strider's internal structure. It had similar leg motions to those of the real insect. However, due to the complexity of the structure, the robot was not small or light enough. As a result, it was supported not by surface tension but by buoyance force. Compared with partially submerged floating objects, robots supported

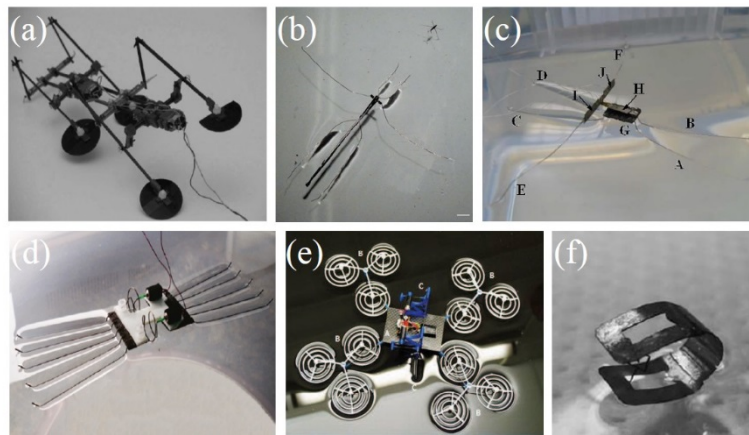


Figure 5. Bio-inspired water walkers. (a), [35]; (b), [4]; (c), [36]; (d), [3]; (e), [37]; (f), [38].

by surface tension experience much smaller drag resistance and thus can achieve higher power efficiency. As shown in Fig. 5(b), Hu *et al.* [4, 38] designed a water-walking device that is sufficiently light to be supported by surface tension. The robot had two rowing legs and was powered by an elastic thread. However, it could travel only for a short time. Figure 5(e) shows a 6-legged elliptical leg rotation robot actuated by three piezoelectric unimorph actuators to mimic the walking behavior of water striders, which was proposed and fabricated by Suhr *et al.* [37]. By setting the vibrational motion of the legs in phase or out of phase, the robot could go forward or backward and steer. Song and Sitti[1] continued Suhr *et al.*'s work[37] and fabricated a similar piezoelectric unimorph actuated robot. The maximum forward speed of the robot was measured to be 3 cm/s, and the rotational speed was 0.5 rad/s. Figure 5(d) shows a DC motor actuated device designed by Ozcan *et al.* [3]. The driving leg motion was also elliptical. The maximum forward and turning speeds of the robot were measured to be 7.15 cm/s and 0.21 rad/s, respectively. As shown in Fig. 5(c), Zhang *et al.* [36] fabricated a water strider robot that was driven by two DC (direct current) motors and had 10 supporting legs and two activating legs. Its maximum speed was 15 cm/s.

Song *et al.* [40] first introduced an untethered water strider robot with 12 supporting legs. One Li-Polymer battery was mounted on the robot to supply power. It could achieve a linear speed of 8.7 cm/s and a rotational motion of 0.8 rad/s. Suzuki *et al.* [41] also fabricated an untethered, single motor driving walking robot. They used the different resonant frequencies of the legs, which were adjusted by slightly changing the length of legs, to control movements in the forward, left, or right direction. Hu *et al.* [38] introduced another untethered device that had a thermal actuator. However, the linear speed was only 2 mm/s, which was one or two orders of magnitude lower than other devices. Wu *et al.* [42, 43] focused on the control of the floating water strider robot. They successfully used infrared signals to remotely control the robot's direction and to change the propulsion speed.

Hu *et al.* [38] introduced a leaping device inspired by *Podura aquatica*, which could catapult itself by striking the free surface with its tail. As shown in Fig. 5(f), the device consisted of a curved leaf spring latched by hand. As soon as the latch was released by heating with a soldering iron, the leaf struck the water surface and catapulted the device upward. The jump height was about 10 cm. Shin *et al.* [44] designed a 6-legged water jumping robot using a shape memory alloy. The robot was capable of jumping to a maximum height of 2.6 cm.

Inspired by the meniscus climbing insects, Hu *et al.* [38] reported a meniscus climbing device that consisted of a rectangular plastic sheet with a thermally actuated Nitinol muscle wire stretching along its midline and attaching to both ends. Ohmic dissipation resulted from passing current causing the wire to contract and the sheet to bend, which created a lateral force for propulsion.

Inspired by surfactant releasing insects, Luo *et al.* [45] utilized the Marangoni effect by applying fluid with low surface tension to the stern to propel the floating boat. Japanese scholars [46] proposed a self-propelling system powered by a redox reaction. The benzoquinone disk could spontaneously move in different modes: continuous, intermittent (repetition between rest and rapid motion), and velocity-decay motions. Since the movements highly depend on the species and concentration of the reductant, the application is limited only to specific conditions. Moreover, this method may bring contamination to the surrounding fluid. The temperature gradient can also generate the Marangoni effect, which is more specifically known as thermocapillarity. Hendaro and Gianchandani [47] generated a Marangoni flow by suspending a heat source above the fluid surface to rotate a micro-motor immersed in silicone oil.

There are also some other propulsion methods that may not be directly adopted from the propulsion mechanisms of natural creatures. Won *et al.* [48] utilized microstreaming flows created by acoustic energized bubbles to propel a water floating mini-boat. Mita *et al.* [49] designed a floating

object propulsion system that utilized bubble movements on the system. The bubble was moved by electrowetting-on-dielectric (EWOD) actuation that was wirelessly powered by the radio frequency power transfer. The immersed air bubble was attached to the dielectric-covered EWOD electrodes that were placed on the exterior surface of the object's bottom. When the voltage was applied to the EWOD electrode, the bubble moved one step. The bubble movement generated the displacement of the surrounding liquid and thus the floating object moved in the opposite direction to the bubble movement based on the action and reaction principle. In order to generate continuous movement, once the bubble moves from one end to the other, a new bubble should be provided at the initial position. However, this system did not have a bubble generation mechanism, so no continuous movements could be achieved.

Chung *et al.* [2] used EWOD to propel a floating object but in a different way. AC (alternating current) signal was applied to the EWOD electrode. The structure was extremely simple and included no moving mechanical parts. However, the propulsion mechanism was not revealed at that time. A following research uncovering the detailed mechanism and studying parameter effects will be illustrated in Chapter 2.

2.0 AC EWOD PROPULSION

2.1 ELECTROWETTING ON DIELECTRIC (EWOD)

2.1.1 EWOD principle

In 1875, Lippmann first recognized that capillary force can be modified by adding electrostatic charge[50]. It didn't draw extensive attention before it was introduced into the MEMS community in the early 1990s. However, from theory to practice, it was necessary to avoid electrolysis of the solution at high voltage. This principle was later proved to be validated in the configuration where the electrode is covered with a thin layer of dielectric layer[51, 52], which can overcome the electrolysis to a great extent. This phenomenon, which is named electrowetting on dielectric (EWOD), has outstanding MEMS devices' favorable features, such as excellent reversibility and low power consumption.

Figure 6 shows a typical configuration of EWOD. An aqueous sessile droplet sits on an EWOD substrate that consists of a dielectric layer and a conductive electrode. In case the dielectric layer is not hydrophobic, another thin layer of hydrophobic material, such as Teflon, is deposited onto the dielectric layer. When a DC potential V_d is applied at the dielectric layer, the electric charge changes the surface energy of the dielectric layer, inducing a change in surface wettability and the contact angle θ . Typically, the contact angle θ decreases with increase of voltage V_d . As a

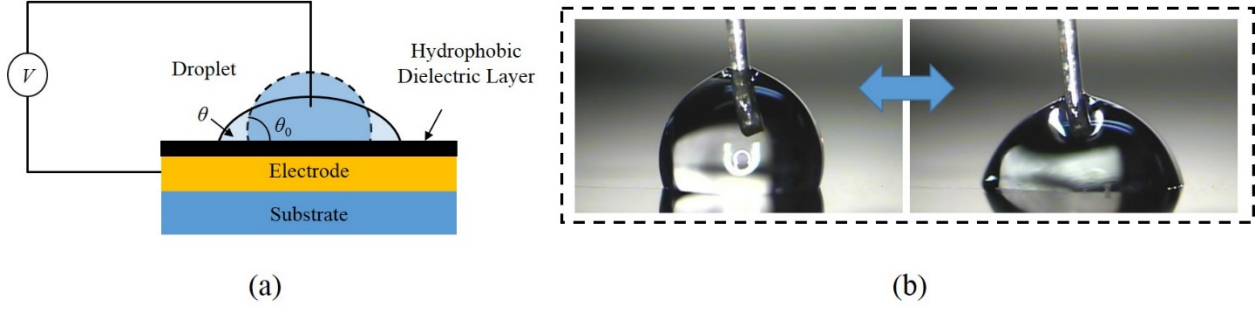


Figure 6. Principle of electrowetting on dielectric. (a) Schematic configuration. The dashed line represents the droplet original shape; the solid line denotes the droplet shape after actuation. (b) Snapshots of basic electrowetting demonstration on a sessile drop.

result, the droplet spontaneously spreads out on the dielectric surface. When the external signal is cut off, the contact angle returns to its initial state θ_0 , which brings the droplet to its original shape.

Equation (2-1), which is known as Lippmann's equation, describes the relation between solid-liquid interfacial tension γ_{sl} and applied electric potential V_d :

$$\gamma_{sl} = \gamma_{sl}^0 - \frac{C_d}{2} V_d^2 \quad (2-1)$$

where C_d (F/m²) is the specific capacitance of the dielectric layer, and γ_{sl}^0 the solid-liquid interfacial tension at no external voltage. The relation between contact angle θ and interfacial tensions at the three-phase contact line is given by Young's equation:

$$\cos\theta = \frac{\gamma_{sg} - \gamma_{sl}}{\gamma_{gl}} \quad (2-2)$$

where γ_{sg} is the solid-gas interfacial tension, and γ_{gl} the gas-liquid interfacial tension.

By substituting Eqn. (2-2) into Eqn. (2-1), one can derive the relation between the contact angle θ and the externally applied voltage across the dielectric layer V_d , which is known as the Lippmann-Young equation:

$$\cos\theta = \cos\theta_0 + \frac{\epsilon_r \epsilon_0 V_d^2}{2\gamma_{gl} t_d} \quad (2-3)$$

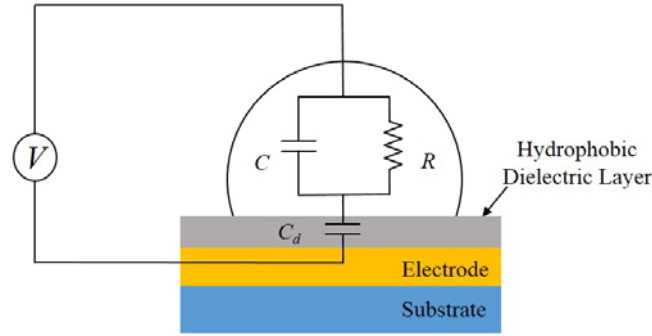


Figure 7. Equivalent circuit diagram for sessile droplet EWOD setup.

where θ_0 is initial contact angle with no external voltage, ϵ_r the relative permittivity of the dielectric layer, ϵ_0 vacuum permittivity (8.854×10^{-12} F/m), and t_d the thickness of the dielectric layer. This equation shows that cosine value of contact angle θ changes parabolically with applied voltage. Because the voltage term V_d in Eqn. (2-3) is squared, the sign or direction of electrical signal does not affect the contact angle value. As a result, the larger absolute value of V_d results in larger $\cos\theta$ and smaller contact angle θ . It is worth mentioning that voltage V_d in Eqn. (2-3) does not necessarily equal total voltage applied to the system V_{total} . A commonly used equivalent circuit diagram for sessile droplet EWOD is shown in Fig. 7[54, 55]. Since the electric current at

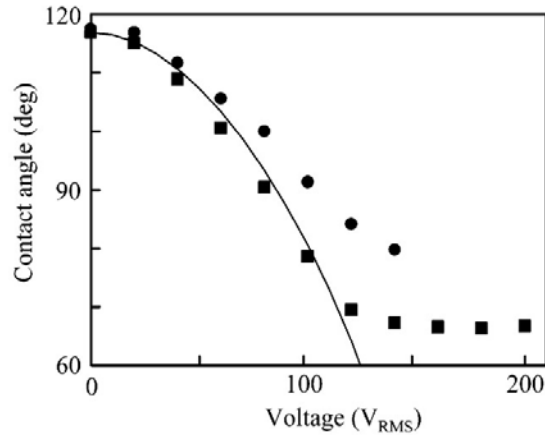


Figure 8. Contact angle of a sessile droplet under DC or AC electrowetting[53]. The rectangular and circular symbols correspond to the cases of DC and AC ($f = 10$ kHz), respectively. The solid line represents the Lippmann-Young equation (Eqn. (2-3)).

steady state is negligible due to the existence of capacitance of dielectric layer C_d , one can assume that voltage across the dielectric layer V_d equals total applied source potential V_{total} for the DC case.

Contact angle can only be manipulated in a certain range. When V_{total} exceeds critical value, the contact angle no longer follows the voltage change and becomes saturated, which is known as contact angle saturation phenomenon[56, 57]. It's clearly shown in Fig. 8 that for DC case (rectangular symbols), at low voltage, the contact angle is coincident with the Lippmann-Young equation, but in high voltage range, the contact angle deviates from the theoretical curve at some point and remains constant for even higher voltage V_{total} .

2.1.2 AC EWOD

According to Eqn. (2-3), when an AC electric field is applied, the contact angle should vary with alternating voltage, which will induce an oscillation of three-phase contact line and, as a result, oscillation of the droplet. But the droplet can only vibrate at a finite range of frequency[58]. At high frequency range (typically higher than several kHz), the amplitude of contact line oscillation becomes very small due to two possible reasons. (1) The voltage V_d decreases as frequency increases if the total voltage applied to the system V_{total} remains the same. This is because, in the AC case, the current is no longer zero, which means there's a voltage drop across the droplet. So the total voltage is divided and only part of it is applied across the dielectric layer. As a result, V_d is less than V_{total} and decreases as frequency increases. (2) The contact line cannot follow the microscopic contact angle change mechanically. As a result, the overall shape of the droplet doesn't oscillate and appears to be deformed at a certain macroscopic contact angle at high frequency.

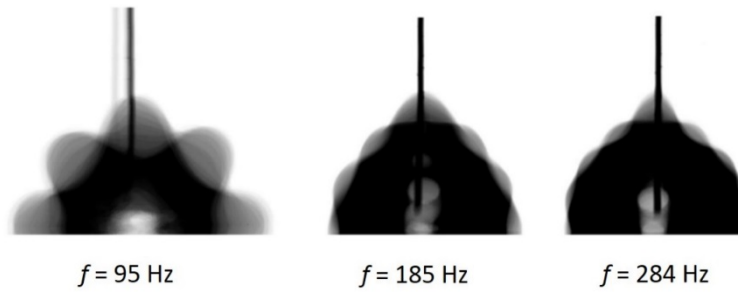


Figure 9. Patterns of droplet oscillation that are obtained by overlapping more than 50 images at 100 V for resonance frequencies[59].

The circular symbols in Fig. 8 show macroscopic contact angle change at high frequency (10 kHz) versus total applied AC voltage V_{total} . The contact angle deviates from the Lippmann-Young equation at much lower voltage compared to the DC case, which is caused by the voltage drop across the droplet.

AC EWOD is commonly used to overcome or reduce the resistance in droplet transportation and to enhance fluid mixing. Oh *et al.* [59] studied frequency dependent oscillation resonance of droplet under AC potential, as shown in Fig. 9. Li and Mugele[60] found that contact angle hysteresis almost disappears with increasing AC voltage, whereas for direct voltage it remains constant. Based on this finding, Mannerje *et al.* [61] proposed and demonstrated a prototype of wiper-free windscreen.

Miraghaie *et al.* [62] reported that the mixing rate of a sessile droplet was significantly enhanced by AC EWOD at a frequency range of 30 to 300 Hz. Mugele *et al.* [63] triggered self-excited oscillations of a millimeter-sized droplet by low frequency AC signal (10-125 Hz) and found that the mixing rate was accelerated by approximately two orders of magnitude comparing with that of pure diffusion. Malk *et al.* [64] observed two pairs of vortex flows inside an oscillating droplet and found that the vortex location could be controlled by adjusting signal frequency. Ko *et*

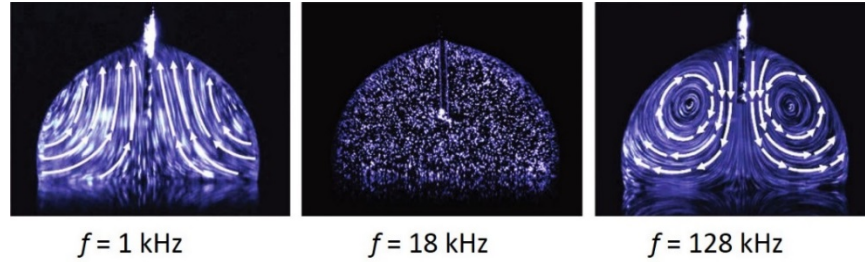


Figure 10. Frequency dependence of flow pattern under AC electrowetting[53].

al. [53] characterized this kind of flow into two types by frequency (Fig. 10). A quite fast flow was observed in a low frequency range of 10 Hz to 15 kHz. In a higher frequency range about 35 to 256 kHz, the flow changes direction. They found that in the low frequency range, flow is insensitive to conductivity of the solution. However, the flow at high frequency is very sensitive to the conductivity of the solution and electrode position. It was suggested that the shape oscillation of a droplet is responsible for the low-frequency flow[53, 59]. Mugele *et al.* [65] explained the strength and frequency dependence for the low-frequency flow by Stokes drift driven by capillary waves that emanate from the oscillating contact line. The high-frequency flow was found to be caused by electrothermal effect[66, 67].

There have also been some other interesting AC EWOD experiments reported. Chung *et al.* [68] developed micro-bubble tweezers that used bubbles actuated by AC EWOD to carry micro-particles. Ko *et al.* [69] found that the oscillation of a sessile bubble in aqueous solution could produce a steady streaming jet within the solution. Jet velocity is proportional to oscillation amplitude and is greatest at natural oscillation frequencies. Chung *et al.* [2] utilized AC EWOD to propel floating objects. The structure was extremely simple and included no moving mechanical parts. A following research uncovering the detail propulsion mechanism and studying parameter effects will be illustrated in the next sections.

2.2 EXPERIMENTAL SETUP

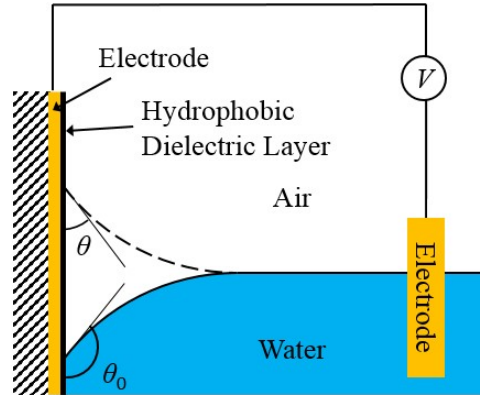


Figure 11. EWOD electrode at vertical wall. θ_0 is the initial contact angle at the wall; θ denotes the contact angle after DC signal applied. Another electrode without dielectric layer covered is inserted into water to form a closed electric circuit.

In traditional droplet or bubble microfluidics (for example, Fig. 6), the EWOD electrode is always arranged horizontally, which results in lateral movements of contact line. If the EWOD electrode is vertically inserted into water and penetrates the interface as shown in Fig. 11, a three-phase contact line is formed. Since water is electrically conductive, the EWOD circuit is closed through water. When there is no electrical potential applied, the contact angle is θ_0 ($> 90^\circ$ due to hydrophobic surface), which makes the meniscus below the infinite free level. When DC voltage V_{total} is applied to the system, the contact angle reduces to θ (assume V_{total} is high enough and $\theta < 90^\circ$), which brings the meniscus above the infinite free surface level. When an AC electric signal (frequency is not very high) is applied, the contact angle will oscillate following the signal, which results in the oscillation of the contact line.

This AC EWOD setup can be implemented in a floating object on a free surface, as shown in Fig. 12. An electrode covered with a dielectric layer is attached to the side surface of the floating

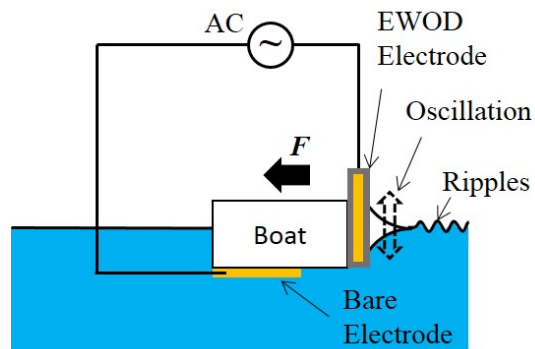


Figure 12. Illustration of AC EWOD propulsion. The EWOD and bare ground electrodes are installed at the stern and bottom of the boat, separately.

object and an additional bare electrode is submerged in water (a possible position of the latter electrode would be the exterior surface of the object's bottom as shown in Fig. 12). In case multiple EWOD electrodes are needed for rotational and steering motions, they can be attached to the other side surfaces normal to the propulsion direction. When an AC voltage is applied to the electrodes, the contact angle oscillates and the free surface in contact with the EWOD electrode(s) also oscillates. These oscillations eventually generate ripples (waves) and propel the floating object.

Figure 13(a) shows how the EWOD electrodes are made. A thin, flexible sheet with a Cu layer of 18 μm in thickness (Dupont Pyralux[®] flexible Cu product) is coated with a 2.5 μm thick parylene layer as a dielectric layer. To make the final surface hydrophobic, a thin layer ($\sim 2000\text{\AA}$ thick) of Teflon AF[®] is dip-coated. Figure 13(b) is the photo of a fabricated device showing how the EWOD and ground (bare aluminum foil) electrodes are installed separately at the stern and bottom of the centimeter-sized test foam boat. The test boat is made out of foam board. The total weight of the test boat with electrodes is 0.27 grams. The dimensions of the boat are 35 (L) \times 25 (W) \times 8 (H) mm^3 . The boat is tested in a pool filled with deionized (DI) water (conductivity of 2 $\mu\text{S/cm}$). In order to minimize mechanical disturbance and resistance to the boat, very thin Cu wires (30 μm in diameter) are used to transmit the AC signal to the electrodes.

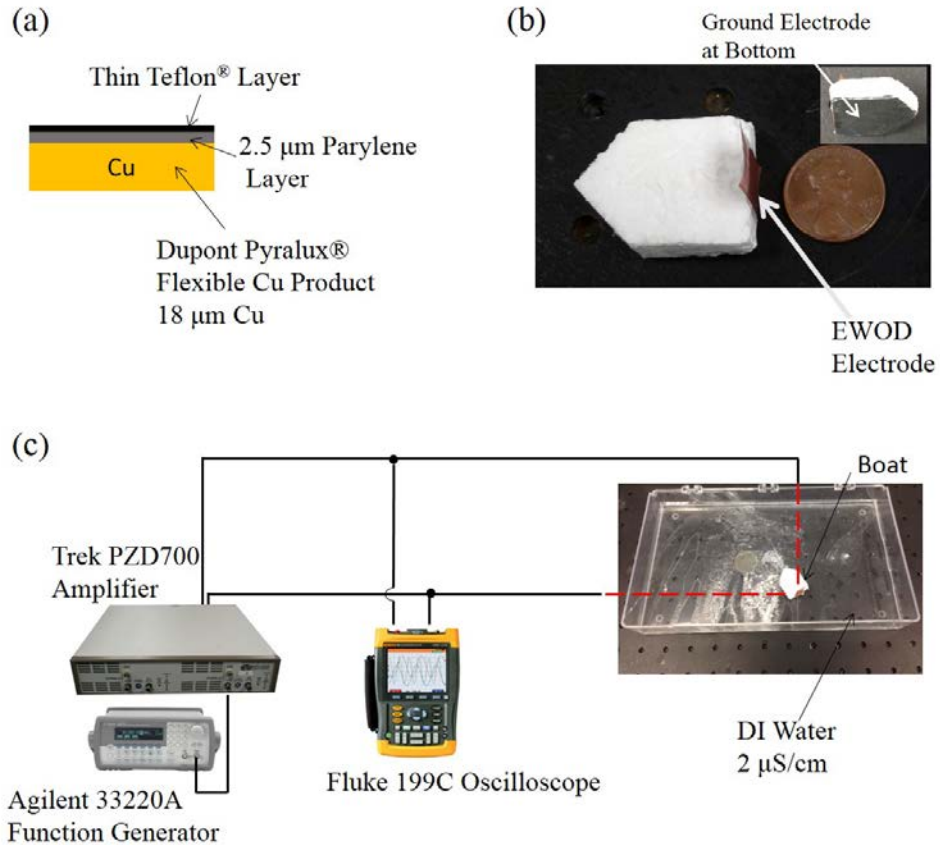


Figure 13. (a) EWOD electrode configuration; (b) Fabricated boat with EWOD and ground electrodes installed. The inset shows the side and bottom of the boat. (c) Experimental setup of AC EWOD propulsion.

2.3 PROPULSION AND MECHANISM

2.3.1 Propulsion test

A variety of boat propelling motions is shown in Fig. 14. The sinusoidal AC input signal is fixed at 100 Hz in frequency and 100 V_{RMS} in amplitude. The water depth h is 10 mm. The EWOD electrode is 10 mm wide. Figure 14(a) shows a linear boat motion when the EWOD electrode is

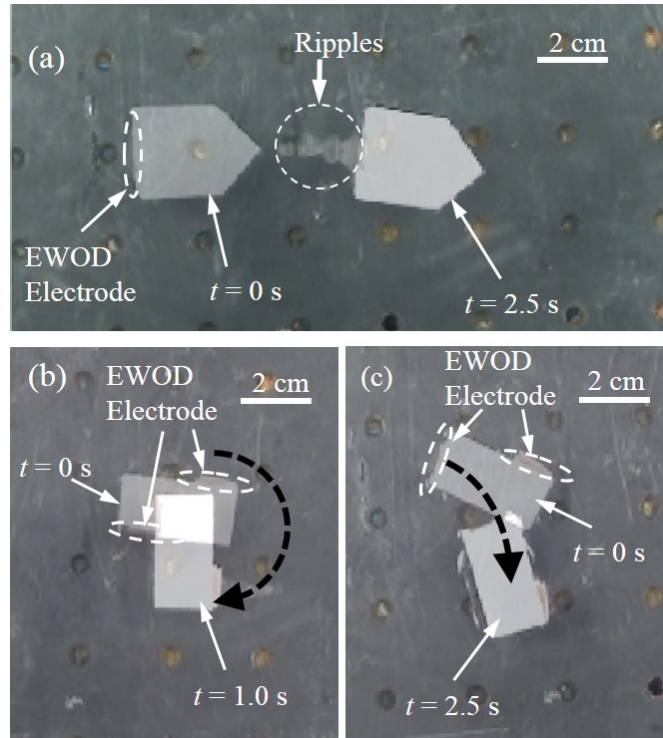
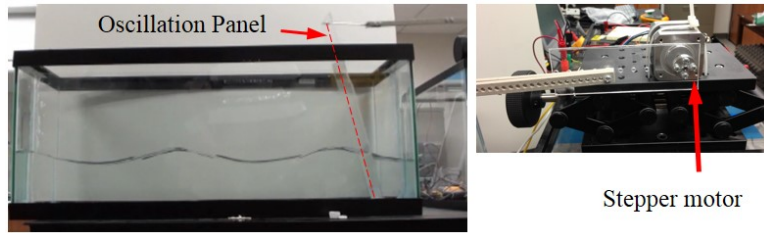
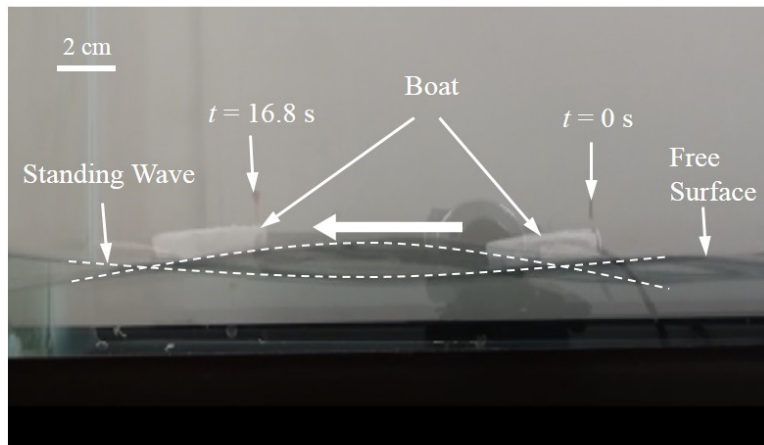


Figure 14. AC EWOD propulsion in stationary water. Two snapshots before and after actuation are overlapped to compare the positions. (a) Linear motion; (b) Rotation; (c) Steering. A boat with a rectangular shape ($30 \text{ (L)} \times 10 \text{ (W)} \times 10 \text{ (H)} \text{ mm}^3$) is used for (b)&(c).

installed at the stern and the ground electrode is mounted on the exterior part of the bottom. The measured maximum linear speed is around 40 mm/s. When multiple EWOD electrodes are installed at different locations on the boat side surface and activated in a combined fashion, propulsion direction can be controlled. The two simplest cases are shown in Figs. 14(b) and 14(c). When two EWOD electrodes are installed diagonally, the boat generates a rotational motion, as shown in Fig. 14(b). The boat can also be steered along a curvilinear path, shown in Fig. 14(c), when one EWOD electrode is placed at the stern and another is at the sidewall. When two or more EWOD electrodes are installed, no ground electrode is needed because the electric circuit can be closed via EWOD electrodes.



(a)



(b)

Figure 15. AC EWOD propulsion in a wave tank. (a) Wave tank and stepper motor; (b) Snapshot superposition of boat propulsion on wave surface. A standing wave is generated in the water tank. Dashed lines show overlapped profiles of the standing wave.

The above experiments were performed on quiescent water. In addition, the boat can be propelled on wavy water, as shown in Fig. 15. A standing wave is generated by a flap type wave maker in a tank of dimensions $768 \text{ (L)} \times 318 \text{ (W)} \times 330 \text{ (H)} \text{ mm}^3$ (Fig. 15(a)). The water depth is 35 mm. The wave amplitude in the tank is around 5 mm. The wave oscillation frequency of 2.75 Hz is carefully chosen based on the dimension of the wave tank and wave amplitude. Figure 15(b) is overlapped images showing the boat moving from a wave node, passing the anti-node, and finally arriving at another node. Dashed lines in Fig. 15(c) show overlapped profiles of the standing wave.

2.3.2 Flow visualizations and propulsion mechanism

In order to understand how the propelling force is generated, the surface waves generated by vertical oscillation of the three-phase contact line are first visualized with the Free-Surface Synthetic Schlieren (FS-SS) method[70]. A random dot pattern is prepared and attached to the bottom of the water tank. A digital camera (Canon XTi) takes top views of the dot pattern through the water before and after the AC EWOD is on. When an electrical signal is applied to the EWOD electrode, generated waves distort the free surface and the pattern image. The camera exposure time is 1/1600 s. The 2-D displacements of individual dots due to refraction of light are computed by the digital image correlation algorithm (freeware Ncorr). Then Surfaceheight Script (PIVMat toolbox for Matlab) is used to reconstruct the surface height based on the displacement field. The error of obtained surface height is less than 10%. Figure 16 shows surface waves near the activated EWOD electrode when an electrical signal of 100 V_{RMS} and 10 Hz is applied to the EWOD system. The water depth is maintained at 10 mm. A periodic pattern of the wave can be observed.

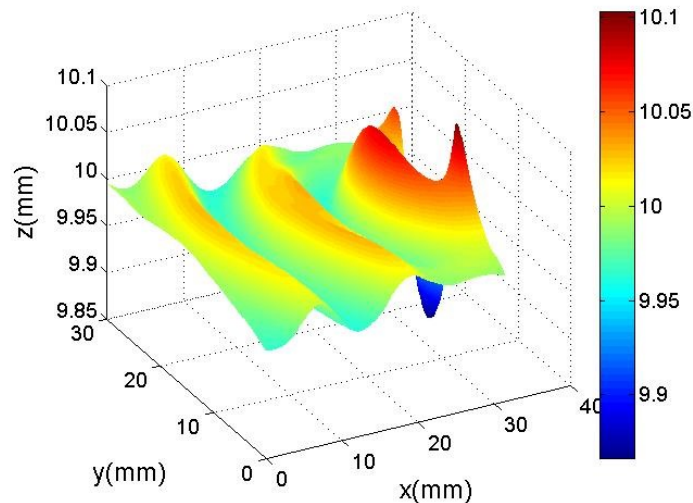


Figure 16. Visualization of surface waves close to the EWOD electrode by FS-SS method ($f = 10$ Hz, $V = 100$ V_{RMS}).

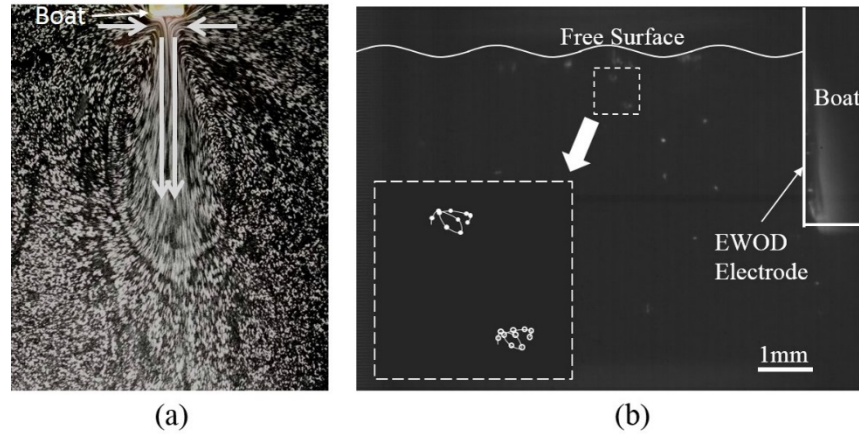


Figure 17. (a) Surface flow visualization (top view, exposure time = 0.6 s); (b) Trajectories of two particle tracers in the center plane behind the boat recorded by a high-speed camera. The amplitude of the wave is not scaled. The inset shows magnified and digitized traces.

Additionally, the overall flow pattern on the free surface is visualized, as shown in Fig. 17(a). Polyethylene microspheres ($50\ \mu\text{m}$ in diameter, $\rho = 1.0\ \text{g/cm}^3$) are seeded on the free surface. The camera exposure time is 0.6 s long. Note that the visualization shows the streaks of the particles during this exposure time, which represent the time-averaged flow field. The flow comes from either side of the electrode and is ejected out normally to the electrode. This ejected flow generates a pushing force that propels the boat in the opposite direction to that of the ejected flow. Figure 17(b) shows trajectories of particle tracers in the centerline in the wake of the boat that are recorded by a high-speed camera (Vision Research Phantom V7.3). Four sequential images are overlapped. These trajectories show the instantaneous velocity of tracers under the oscillating free surface. The AC EWOD signal applied is sinusoidal at 10 Hz in frequency and $100\ \text{V}_{\text{RMS}}$ in amplitude. The inset shows magnified and digitized trajectories of two tracers. When the free surface is oscillated by EWOD, the tracers follow elliptical orbits. Interestingly and importantly, however, the tracers have net displacements (drift) moving away from the EWOD electrode after finishing one period of oscillation. The ejecting flow in the flow visualization on the free surface

results from these net displacements. The tracers near the free surface have a larger orbit and displacement than the tracers farther from the free surface do.

Figures 18(a) and 18(b) show time-averaged velocity fields in the center and cross-sectional planes of the wake region that are measured by PIV (particle image velocimetry). 532 nm YAG laser (New Wave SoloIII-15) is diverged into a laser sheet. A camera (Powerview Plus 4MP) is located perpendicularly to the laser sheet. The synchronizer (TSI 610034) coordinates the timing between the laser and the camera. The image acquisition is accomplished by Insight 3G™ software platform (TSI Inc.) that deals with all timing coordination and phase triggering settings and generates velocity vectors over the entire field of view. One can clearly see an outgoing flow ejected normally to the electrode near the free surface in the center plane (Fig. 18(a)), which is consistent with the flow visualization in Fig. 17(a). This outgoing flow, in turn, exerts a momentum to the boat, which is responsible for propulsion of the boat. The flow is fastest on the free surface and decays very quickly as the depth increases. Near the electrode, the flow has a horizontal

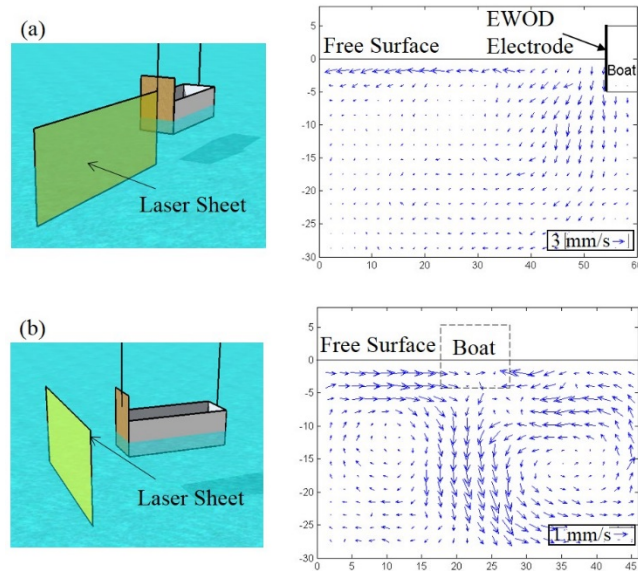


Figure 18. Velocity field measurement: (a) PIV measurement in the centerline of the wake; (b) PIV measurement 10 mm downstream from the EWOD electrode (boat stern).

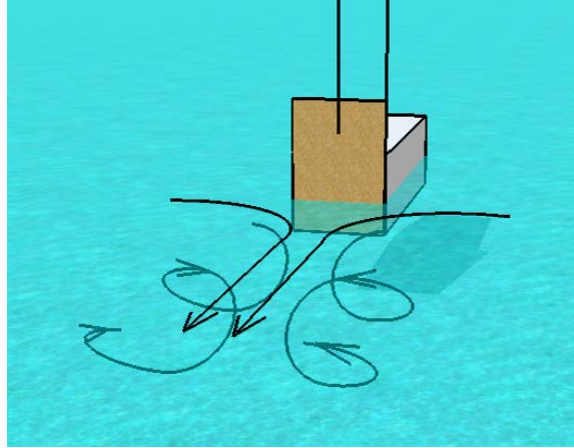


Figure 19. 3-D flow field sketch based on the measurements.

component (outgoing from the electrode) as well as a vertical (downward) component. The cross-sectional velocity measurement is made 10 mm downstream from the boat stern (Fig. 18(b)). At this point, there exist two counter-rotating vortices. Based on all these results, an overall 3-D flow pattern is sketched, as shown in Fig. 19. A flow (non-zero time-averaged flow) with two counter-rotating spiral vortices is generated by a free surface oscillation near the electrode.

Previously, Hocking reported a similar wave that was produced by a vertically oscillating plate partially immersed in water [71], even though the associated drift flow was not investigated. The above trajectories in Fig. 17(b) resemble the Stokes drift in capillary waves [72, 73], which describes the phenomenon that fluid particles just below the free surface experience a net displacement along the wave propagation direction after a period of time when surface waves travel by. The Stokes drift (net displacement) is mathematically interpreted as the difference between the second order terms in the Eulerian and Lagrangian mean velocities [74, 75]. Note that the first order terms in the Eulerian and Lagrangian mean velocities are identical. In addition, the counter-rotating vortices in Fig. 18(b) are similar to the Langmuir circulation [76] that is the result of interactions between the Stokes drift current induced by surface waves and the mean current

[77]. All these flow visualization results are consistent with the flow behaviors associated with the Stokes drift, which is the responsible mechanism for the present AC EWOD propulsion.

The drift velocity u_{drift} (= net displacement/time) in the Stokes drift can be represented by the wave theory [73, 78]:

$$u_{drift}(z) = k\omega A^2 e^{2kz}, \quad (2-4)$$

where k is the wavenumber of oscillation, ω the angular frequency, A the wave amplitude, and z the vertical distance from the free surface. The drift velocity depends on the properties of the surface wave (k , A and ω). In addition, the velocity decays as z increases, which is in qualitative agreement with the above tracer trajectories. Mugele *et al.* [65] observed a similar Stokes drift in the capillary wave when a sessile droplet was oscillated by AC EWOD at a low frequency. This work showed that the Stokes drift was responsible for the enhancement of fluid mixing within the droplet. In the capillary wave, the wave frequency ω can be related with the wavenumber k by the gravity-capillary wave dispersion relation [79]:

$$\omega^2 = \left(g + \frac{\gamma}{\rho_w} k^2\right) k \tanh(kh), \quad (2-5)$$

where ρ_w is density of water. The drift velocity at the free surface ($z = 0$) is

$$u_{drift}(0) = k\omega A^2. \quad (2-6)$$

Note that the frequency of the EWOD input signal is not necessarily equal to the wave frequency. If one assumes that Eqn. (2-3) is still valid for EWOD motions oscillating at the fairly low frequency, the major frequency of the contact angle (or contact line) oscillation would be double that of the EWOD signal frequency as the cosine of the contact angle is related to the square of the EWOD signal. That is, for the sinusoidal AC signal with frequency f , the contact line oscillates at frequency $2f$ with two peaks in oscillation amplitude during one signal period. In addition to the frequency doubling, the dynamic response of the contact line movement comes into

play. Some previous studies [65, 80] on the droplet configuration reported that the time-varying contact angle does not necessarily have two identical peaks in one signal period. This means that the contact angle and possibly the wave generated in the free surface may have fundamental, subharmonic and harmonic frequencies. When the EWOD frequency was set at f in the present experiment, it was observed by high-speed images that the major frequency component in the contact line oscillation was the second harmonic (i.e. $2f$). The visualization of free surface by the FS-SS method also confirms that the major frequency of the surface wave is $2f$ and not the signal frequency f . Based on this, it is inferred that the major component of ω in Eqn. (2-6) is $4\pi f$.

2.3.3 Stokes drift and parameter effects

There are many parameters that influence the EWOD boat propulsion. According to Eqns. (2-5) and (2-6), the drift velocity, which is critical to the EWOD boat propulsion, depends on the frequency and the amplitude of the generated wave, which are determined by the change in the AC EWOD contact angle. According to Eqn. (2-3), the change in the contact angle is a function of the dielectric constant and thickness of the dielectric layer, the initial contact angle, the surface tension, and the voltage applied to the dielectric layer. Throughout the experiments for the parameter effects study, the thickness of the dielectric layer is fixed at 2 μm . In addition, DI water (conductivity of 2 $\mu\text{S/cm}$) at room temperature is used for the working fluid, and the water depth is fixed at 10 mm. As a consequence, the remaining parameters affecting propulsion are the amplitude and the frequency of the applied EWOD signal. In addition, it turns out that the EWOD electrode width b and the shape (sinusoidal, triangular, square waves) of the EWOD signal also affect the propulsion. In the following subsections, the effects of these parameters on the Stokes drift and propulsion speed will be presented and discussed.

2.3.3.1 Effect of signal frequency

Figure 20(a) shows experimental results of contact line oscillation amplitude vs. EWOD signal frequency when the amplitude of the EWOD signal is fixed at $V_{total} = 100 \text{ V}_{RMS}$. High-speed images are used for measurement of contact line oscillation amplitude. The oscillation amplitude quickly decreases as the frequency increases and is undetectable when the frequency reaches 1

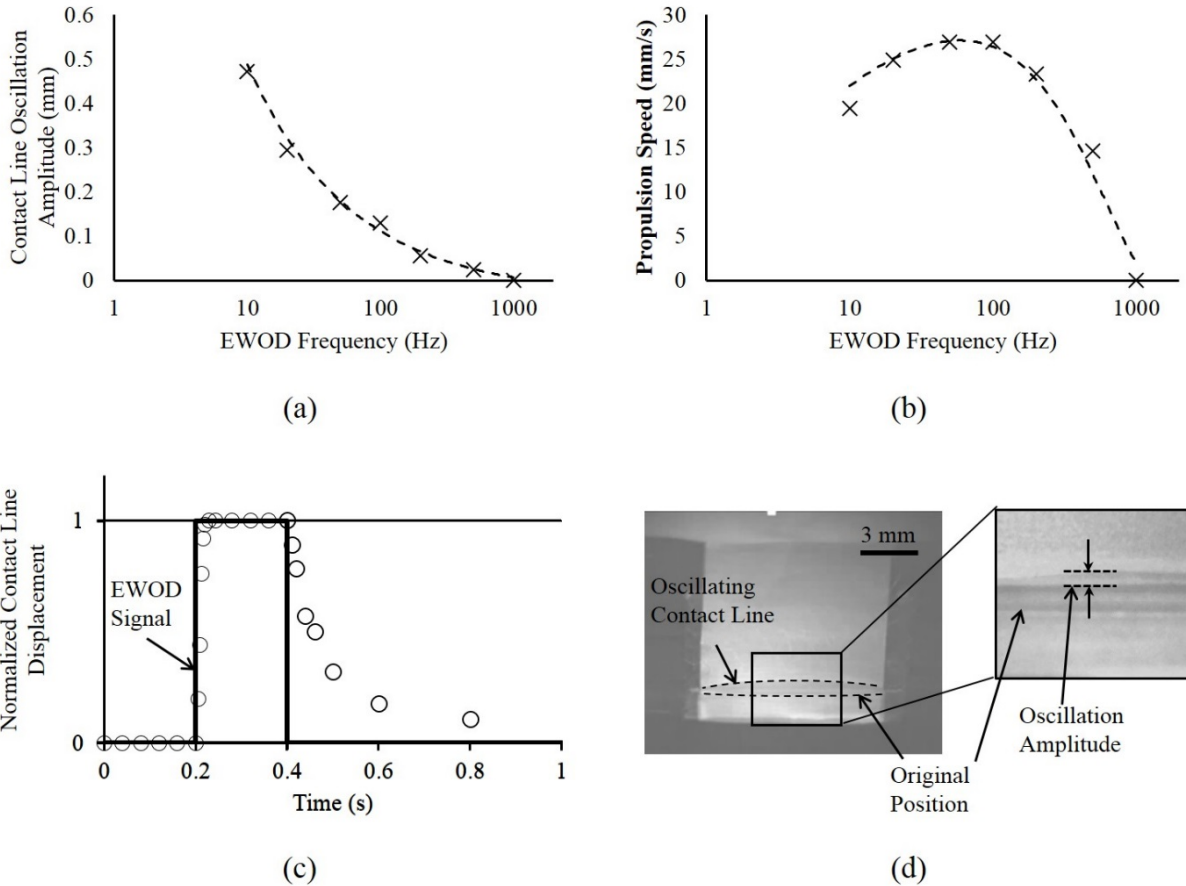


Figure 20. (a) Oscillation amplitude of the contact line vs. EWOD frequency (the broken line is a power series fit, $V_{total} = 100 \text{ V}_{RMS}$, $h = 10 \text{ mm}$, $b = 10 \text{ mm}$ with sinusoidal EWOD signal); (b) Boat speed vs. frequency (the broken line is a curve fit by Eqn. (2-10), $V_{total} = 100 \text{ V}_{RMS}$, $h = 10 \text{ mm}$, $b = 10 \text{ mm}$ with sinusoidal EWOD signal); (c) Response of the contact line to an EWOD step voltage; and (d) Positions of the contact line when an AC EWOD is applied. The right figure is the magnified image to show the position and movement of the contact lines.

kHz. A curve fit with power series is shown as a broken line in Fig. 20(a). Experimental measurements of boat propulsion speed at different frequencies are shown in Fig. 20(b). The boat speed increases until the frequency increases up to $f = 100$ Hz. However, the speed decreases when $f > 100$ Hz and reaches almost zero at 1 kHz. This overall trend can be explained by the Stokes drift. In the constant-speed boat propelling, the propulsion force is balanced by the drag force on the boat:

$$F_{prop} = F_{drag}. \quad (2-7)$$

If the Stokes drift generates the majority of momentum exchange with the boat, the propulsion force can be roughly estimated by integrating the momentum induced by the Stokes drift velocity near the wake region:

$$F_{prop} \approx \int_{-h}^0 \rho_w u_{drift}(z)^2 b dz = \frac{\rho_w k \omega^2 A^4 b}{4}. \quad (2-8)$$

Note that resistance by the tethered powering wires (30 μm in diameter Cu wires) is neglected and the pressure is assumed to be uniform). In the meantime, the drag force may be expressed as:

$$F_{drag} \approx \frac{1}{2} C_D \rho_w u_{boat}^2 A_{boat}, \quad (2-9)$$

where C_D is drag coefficient, u_{boat} propulsion speed of the boat, and A_{boat} the projected area of submerged boat part. Substitution of Eqns. (2-8) and (2-9) into Eqn. (2-7) yields a relation of the boat speed:

$$u_{boat} \approx \sqrt{\frac{b}{2C_D A_{boat}}} \sqrt{k} \omega A^2. \quad (2-10)$$

Using Eqn. (2-10), the propulsion speed is curve-fitted (broken line in Fig. 20(b)). In this fitting, $4\pi f$ is used for ω , k is obtained from Eqn. (2-5), and $C_D = 0.0065$ is determined by the curve fitting. In addition, it is assumed that the wave amplitude is equal to the oscillation amplitude of the contact line. That is, the curve fit result in Fig. 20(a) is used for A . The curve fit of propulsion

speed in Fig. 20(b) matches the experimental result very well. The increasing trend for $f < 100$ Hz is mainly attributed to the product term $\sqrt{k}\omega$ in Eqn. (2-10). The decreasing trend for $f > 100$ Hz is due mainly to the fast decrease in oscillation amplitude A at high frequency. A similar decrease in oscillation amplitude at high frequency was observed in a sessile droplet configuration [80]. During the experiments, it was observed that the contact line on the EWOD electrode advanced (moved up) quickly but receded (moved down) slowly, as Fig. 20(c) shows the response of the contact line to a step signal of EWOD. This is a main reason for the decrease in the amplitude of contact line oscillation as the frequency increases. The high frequency EWOD signal does not allow sufficient time for the contact line to completely return to the initial position, thus, the averaged position of the contact line during oscillation stays higher than the original position without a full swing between the initial and highest positions of the contact line, as shown in Fig. 20(d). This behavior becomes more prominent as the frequency increases, as reflected in the decreasing oscillation amplitude shown in Fig. 20(a). Another possible reason for the decrease in oscillation amplitude is that the voltage across the dielectric layer decreases as the frequency increases, even though the total voltage applied to the EWOD system V_{total} maintains the same. This is due to the increase in the electrical impedance of the water as the frequency increases. That is, the water acts as a voltage divider and the voltage drop across the water becomes larger as frequency increases.

2.3.3.2 Effect of signal amplitude

The effect of the amplitude of the EWOD signal to the contact line oscillation amplitude is shown in Fig. 21(a). The signal frequency is fixed at $f = 100$ Hz. The oscillation amplitude increases until the voltage amplitude increases (Fig. 21(a)) up to 140 V_{RMS}. Note that there is a threshold voltage

(~50V) to initiate the movement of the contact line. The threshold voltage is related to contact angle hysteresis[81, 82], which is common in contact line movements. To initiate advancing of the contact line, an excessive change in the contact angle is required to overcome resistance forces. After the peak, the oscillation amplitude decreases as the voltage further increases. The broken line in Fig. 21(a) is a Fourier series fit. The experimental measurements of propulsion speed at different applied voltages are shown in Fig. 21(b). The overall trend is similar to that of the contact

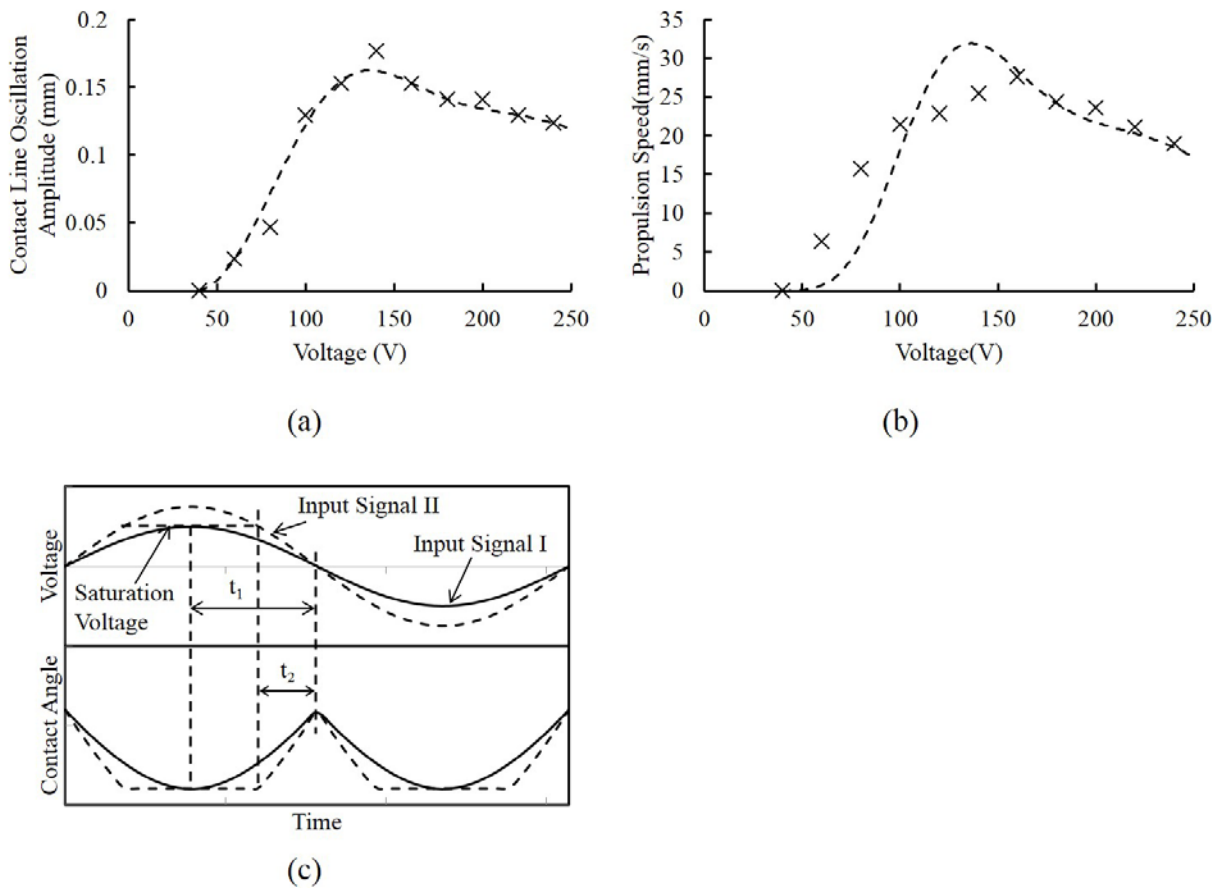


Figure 21. (a) Oscillation amplitude of the contact line vs. EWOD voltage V_{total} (the broken line is a Fourier series fit, $f = 100$ Hz, $h = 10$ mm, $b = 10$ mm with sinusoidal EWOD signal); (b) Boat speed vs. signal voltage (the broken line is a curve fit by Eqn. (2-10), $f = 100$ Hz, $h = 10$ mm, $b = 10$ mm with sinusoidal EWOD signal); and (c) Contact angle saturations for two sinusoidal signals with different amplitude.

line oscillation amplitude. Again, using Eqn. (2-10) the propulsion speed is curve-fitted ($C_D = 0.02$), as shown by the broken line in Fig. 21(b).

These overall trends of the contact line oscillation amplitude may be qualitatively explained as follows. According to Eqn. (2-3), the cosine of the contact angle is proportional to the squared voltage. As the voltage increases, the oscillation amplitude of the contact angle and contact line also increase. As a result, the drift speed and the propulsion speed increase. The decreasing trend in propulsion speed after the peak voltage results from the well-known phenomenon in EWOD, called contact angle saturation, where there is no further decrease in the contact angle above a certain voltage[56, 57]. This explanation can be further detailed as follows. For example, consider two sinusoidal EWOD signals (Input signals I and II) in Fig. 21(c). Let the amplitude of Input signal II be higher than that of Input signal I and let the voltage of contact angle saturation equal to the peak of Input signal I. The contact angle saturation for Input signal II would start earlier and stay longer within each oscillation period than that of Input signal I would. The longer saturation time results in a shorter time for the contact line to recede (in Fig. 21(c), t_1 is longer than t_2). That is, the contact line would not move down much. This eventually leads to smaller oscillation amplitudes of the contact line. This is the reason why the contact line oscillation amplitude and the boat speed both decrease when the applied voltage increases over a certain voltage.

2.3.3.3 Effect of EWOD signal shape

The EWOD signal shape significantly affects the propulsion speed. Figure 22(a) shows the effect of the EWOD signal shape on the oscillation amplitude of the contact line. Three different signals at the fixed EWOD voltage amplitude ($V_{total} = 100 \text{ V}_{\text{RMS}}$) were examined: sinusoidal, triangular, and modified square signals. The reason the modified square signal (3rd signal in Figure 22(a)),

not regular square signal, is examined is as follows. According to Eqn. (2-3), EWOD does not respond to the polarity of the applied signal. That is, the regular square signal would be rectified to a DC signal by EWOD and would not oscillate the contact line. The modified square signal, which has two peaks (positive and negative) within the signal period and stays a zero level between the peaks, will generate oscillations in the contact line. All three signals have two peaks (positive and negative) within the period, so the wave oscillation frequencies for three signals are the same. One can see in Figure 22(a) that the oscillation amplitude for all three signals monotonically decreases as the frequency increases. The sinusoidal and triangular signals have similar oscillation amplitudes in the entire range while the modified square signal generates much larger amplitude, especially in the low frequency range. The measured propulsion speeds for three signal shapes are shown in Figure 22(b). The overall trends for these three signals are similar: they all initially increase as the frequency increases, and decrease after the peaks. These trends are also well curve-fitted by Eqn. (2-10) ($C_D = 0.0065$). The sinusoidal and triangular signals generate the similar propulsion speed, while the modified square signal generates much faster propulsion than the sinusoidal and triangular signals throughout the entire frequency range.

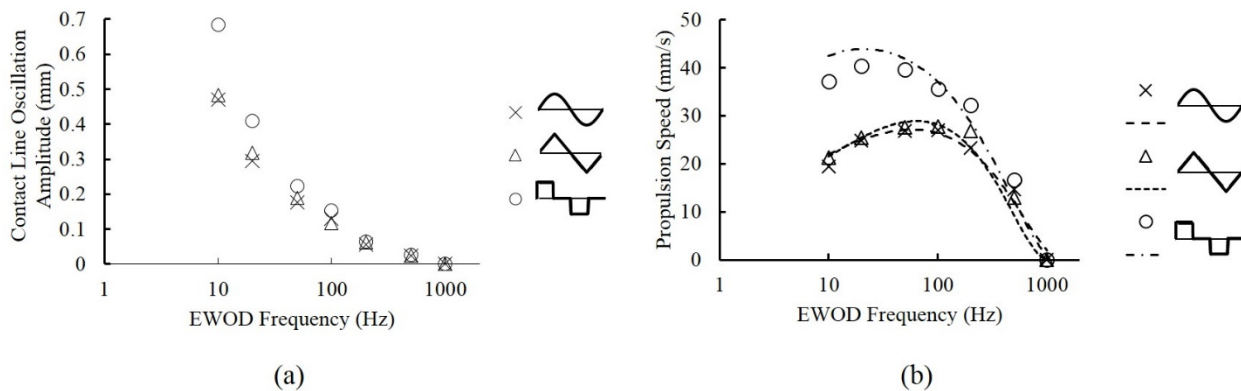


Figure 22. (a) Oscillation amplitude of the contact line for three signal shapes vs. frequency. ($V_{total} = 100 V_{RMS}$, $h = 10$ mm, $b = 10$ mm); and (b) Boat speed for three signal shapes vs. frequency. The lines are curve fits by Eqn. (2-10).

The effects of these three signal shapes can be understood as follows. The sinusoidal and triangular signal profiles in time domain are not very different when they have the same RMS value. Thus the oscillation amplitudes and propulsion speeds for these two signals are very similar. In addition, the sinusoidal and triangle signals do not decrease quickly after they reach their peaks, compared to the modified square signal. This may retard recession of the contact line at a similar rate and result in smaller amplitudes in the contact line oscillation. However, the modified square signal sharply drops to zero after peaks, which means retracting of the contact line is not hampered by the electrowetting force but is immediately drawn by other forces (e.g., gravity). The contact line moves further down and the oscillation amplitude of the contact line is larger. As a result, the propulsion speed becomes larger, even though the modified square signal does not have a higher peak ($141 V_{\text{Peak}}$) than the sinusoidal ($141 V_{\text{Peak}}$) and triangular ($173 V_{\text{Peak}}$) signals for the same RMS value.

2.3.3.4 Effect of electrode width

When the EWOD electrode becomes wider, the propulsion speed becomes faster, as shown in Fig. 23. During the experiment, the same boat was used with the exception of the width of the EWOD electrodes. As seen in Fig. 23, the boat speed with the 20 mm wide electrode is approximately

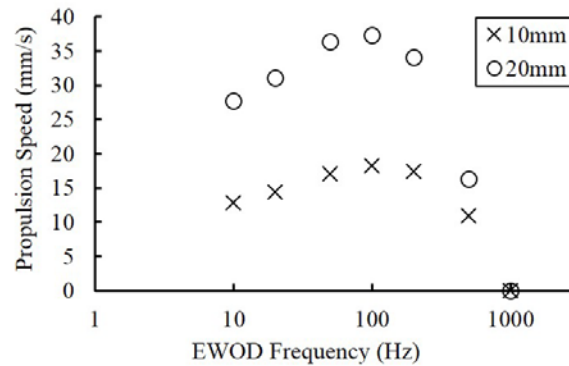


Figure 23. Effect of electrode width. (Sinusoidal signal, $V_{\text{total}} = 100 V_{\text{RMS}}$, $h = 10 \text{ mm}$)

twice as fast as that with the 10 mm wide electrode. In addition, it was observed in the surface flow visualization that the width of the Stokes drift flow is approximately doubled when the electrode width changes from 10 mm to 20 mm (not shown). According to the wave theory, the energy carried by waves is linearly proportional to the length of the wave crest[78]. A wider oscillating contact line generates higher wave energy and, accordingly, more momentum in the Stokes drift.

2.4 WIRELESS PROPULSION

Except for the controllable parameters introduced in the previous section, such as AC frequency, voltage amplitude, dielectric layer thickness, and water conductivity, that may affect the propulsion speed, some other factors, such as environment air flow and force from bended connection thin wires, can also strongly influence the propulsion because the propulsion force is very small. In the conventional boat propulsion system (Fig. 13(c)), 30 μm in diameter copper wires have been used to minimize the effect of wire bending to the boat motion. However, the wires not only generate large force comparing with the propulsion force, but also limit the extent

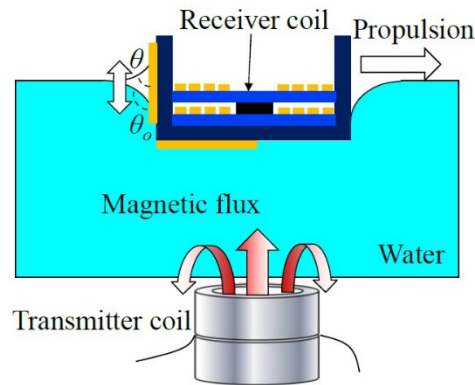


Figure 24. Sketch of wireless AC EWOD propulsion system.

of the propulsion area that the boat can reach. Instead of employing thinner wire in the mini-boat propulsion system, a wirelessly operated system (Fig. 24) is introduced to avoid adverse effects that are brought by connection wires.

In this configuration, a wireless power transmitting system is employed. A planar receiver coil is integrated with an EWOD electrode and installed on the boat. A spool type inductor coil acting as a transmitter is put under the water container and can be moved to align with the receiver coil to transmit an AC electrical signal.

2.4.1 Wireless EWOD

Mita *et al.* [49] first presented a wireless EWOD operation using a commercial inductive coupling chip. They used a very thin dielectric layer to achieve low voltage EWOD operation. Driving voltage at the receiver side was around 15 V.

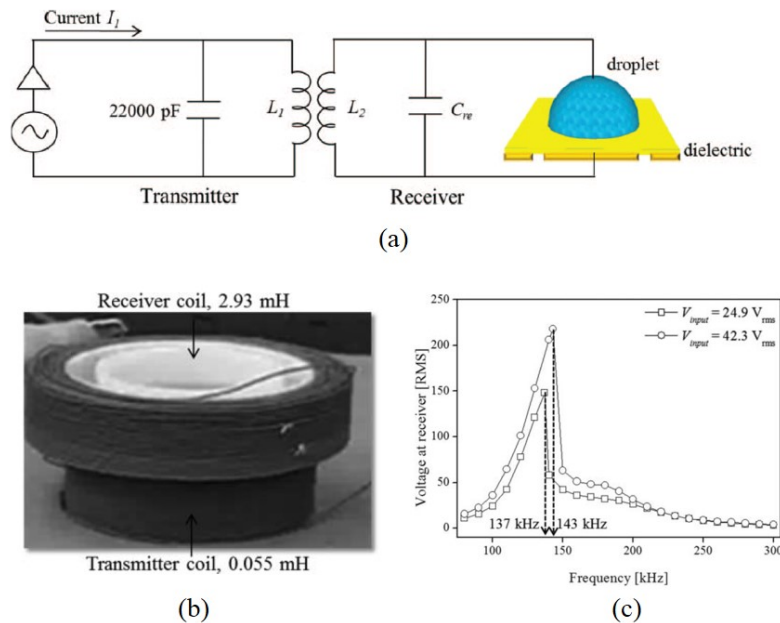


Figure 25. Wireless EWOD principle[83]. (a) Schematic of EWOD wireless powering using inductive coupling; (b) The receiver coil and the transmitter coil; (c) Voltage at the receiver.

However, voltage for a typical EWOD application needs to be higher than 50 V. As shown in Fig. 25, Byun and Cho[84] reported a wireless EWOD droplet setup using a homemade spool type inductor coil. According to theory, a high transmission frequency (> 100 kHz) is desirable in order to achieve higher transmission efficiency, in other words, higher voltage. But, as already discussed in subsection 2.1.2, a three-phase contact line cannot follow high frequency (> 1 kHz), which implies that it is very difficult for a contact line to directly oscillate in harmony with the transmitted frequency. They thus introduced an amplitude modulated signal at the transmitter side. A low frequency envelop signal that is favorable for the EWOD system was carried by a high frequency carrier frequency, which can be adjusted according to the transmission efficiency. A demodulator at the receiver side, or self-demodulated droplet[85], was used to separate the envelop signal from the carrier signal. Thus, high transmission efficiency and low EWOD signal frequency can be achieved simultaneously. Voltage at the receiver side could easily climb up to several

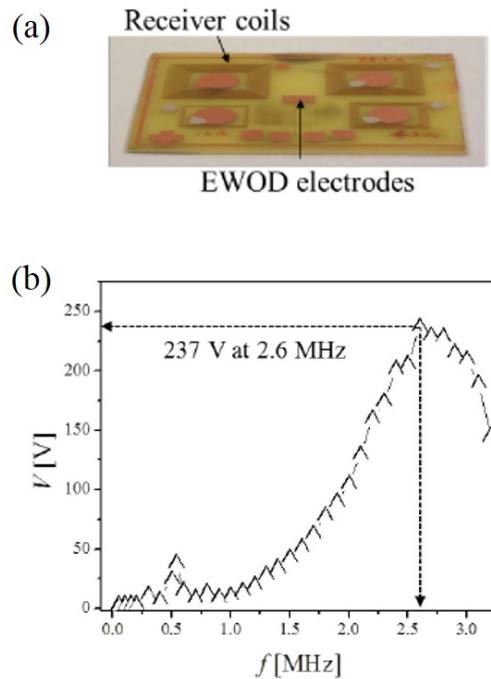


Figure 26. Planar type wireless EWOD[84]. (a) Planar type receiver together with EWOD electrodes; (b) Voltage at the receiver side without droplet.

hundred volts. Although there was a lot of energy consumption by additional electric components, due to the high transmission frequency, voltage directly applied across the dielectric layer was still much greater than the required EWOD operation voltage.

In order to easily integrate with traditional planar type EWOD devices, Byun *et al.* [84] fabricated receiver coils on a planar PCB board but kept the spool type transmitter. The performance of the planar receiver coil is similar to that of a spool type coil except that the frequency shifts to a higher frequency range. Figure 26 shows the photo of the planar coil and voltage output at the receiver side.

2.4.2 Experiment

The microfabrication process flow of the planar receiver coils is shown in Fig. 27(a). Figure 27(b) shows a single receiver coil on a PCB board. In this experiment, two planar receiver coils, having

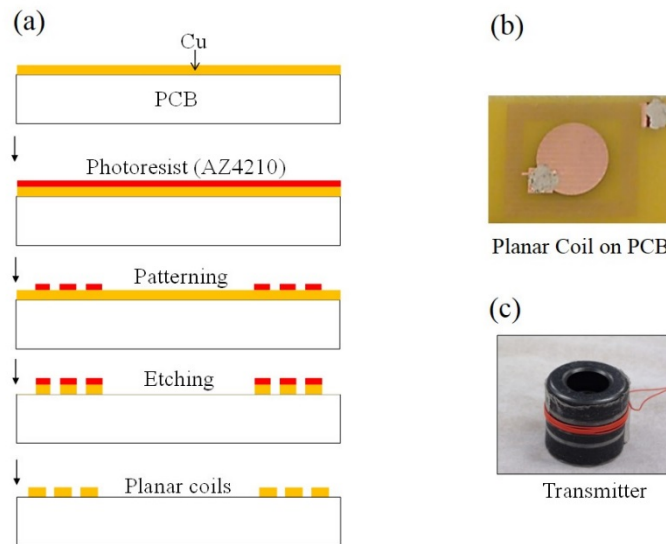


Figure 27. (a) Microfabrication process flow of planar coils on PCB. Cu layer (15 μm) on top of 1.5 mm of board thickness is patterned by photolithography process and wet-etched. (b) A photo of fabricated planar coils. (c) A photo of transmitter coil. The wire (diameter $\sim 250 \mu\text{m}$) is wound around air-cored ferrite rings.

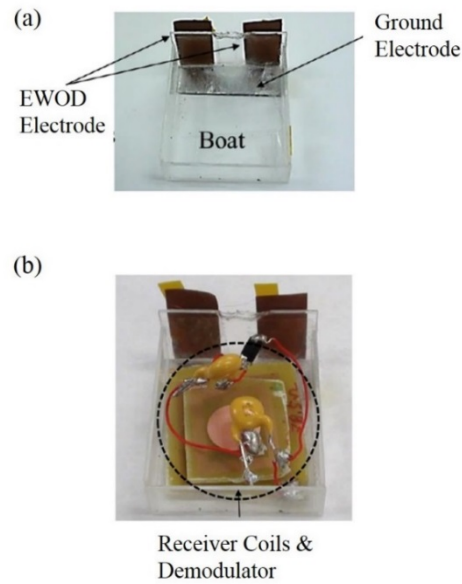


Figure 28. Boat for wireless EWOD propulsion. (a) EWOD electrodes and ground electrode installed on boat; (b) Photo of wireless EWOD boat with receiver circuit installed.

20 and 42 winding-turns, are connected and stacked in series. A single wire (diameter $\sim 250 \mu\text{m}$) winding around air-cored ferrite rings acts as a transmitter (Fig. 27(c)). As shown in Fig. 28, a transparent box-type mini boat with an open top ($38 \text{ (L)} \times 32 \text{ (W)} \times 10 \text{ (H)} \text{ mm}^3$) is prepared, and two flexible Cu EWOD electrodes that are same as those introduced in Fig. 13 are prepared and glued at the stern of the boat. The ground electrode is also installed on the external bottom side of the boat. The total weight of the wireless boat is approximately 7.1 grams after all the devices and electrodes are installed.

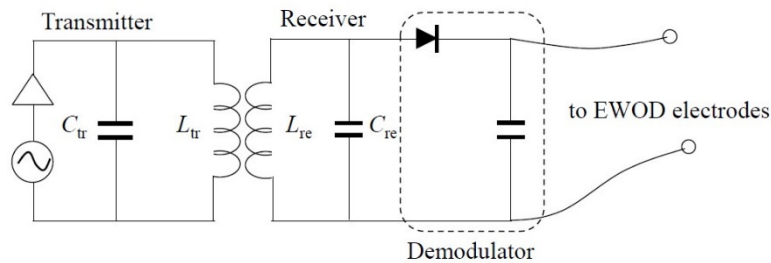


Figure 29. An equivalent electric circuit using magnetic induction. L_{tr} and C_{tr} is the inductance and capacitance of the transmitter. L_{re} and C_{re} is the inductance and capacitance of the receiver.

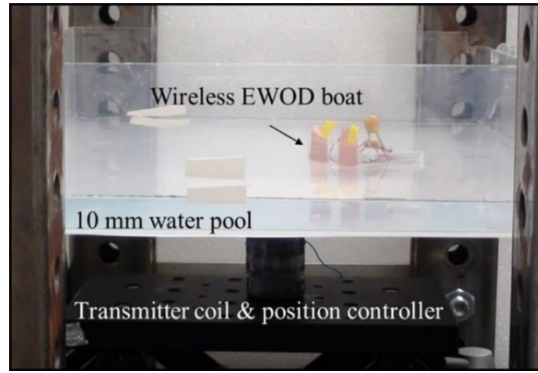


Figure 30. Photo of wireless boat propulsion setup.

An equivalent electric circuit is illustrated in Fig. 29. The inductance of the transmitter coil L_{tr} is about $0.5 \mu\text{H}$. The transmitter is connected to a capacitor ($C_{tr} = 4700 \text{ pF}$) in parallel. The receiver circuit is also composed of two stacked planar coils in series with the capacitor ($C_{re} = 22 \text{ pF}$) in parallel, and a demodulation circuit is also installed in front of the EWOD and ground electrodes. The demodulation circuit is composed of single diode (IN5399-E3/54, Vishay General Semiconductor) and ceramic capacitor (1500 pF). Overall experimental setup for the wireless EWOD boat propulsion is pictured in Fig. 30. The wireless boat is tested in a pool filled with 10 mm depth of DI water ($2 \mu\text{S/cm}$). The transmitter coil sitting on the position controller is placed under the water pool in which a center to center alignment is manually achieved between the transmitter coil and receiver coils.

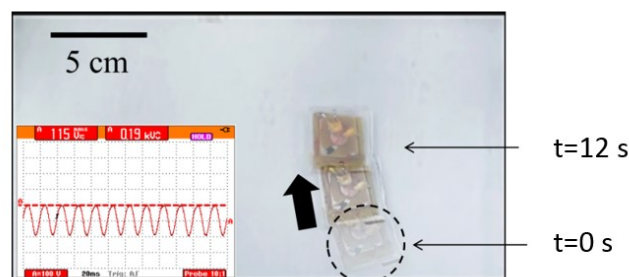


Figure 31. Snapshot superposition of wireless EWOD propulsion. The inset represents the signal applied to wireless boat.

The demonstration of wireless EWOD boat propulsion is shown in Fig. 31. When the wireless transmitted voltage shown in the inset in Fig. 31 is applied at the EWOD electrodes, the boat is propelled and moves forward. The transmission carrier frequency is 3.5 MHz with 50 Hz of low frequency envelope. The overlaid images clearly demonstrate the propulsion. The maximum propulsion speed is approximately 5 mm/s. This speed is much lower than that introduced in section 2.3 (about 40 mm/s) because the boat with a wireless powering circuit is much heavier than that in the previous case.

2.5 SUMMARY

This chapter describes a propulsion mechanism of the centimeter sized floating object utilizing AC EWOD and investigates the effects of many parameters including the frequency, amplitude and shape of the applied EWOD signal and the width of the EWOD electrode on propulsion. The floating object is propelled by vertically oscillating the free surface using AC EWOD. The oscillating free surface generates a Stokes drift that is responsible for propulsion. The wave patterns are visualized using the Free-Surface Synthetic Schlieren (FS-SS) method, and the overall velocity field in the wake region of the floating object is visualized and measured by a PIV system. A 3-D flow field sketch is constructed based on the flow visualizations and PIV measurements, which show that near a free surface a streaming flow outgoing from the electrode is generated and below the free surface two counter-rotating spiral vortices are generated. These flows induce a momentum exchange with the floating object and generate a propulsion force. The propulsion speed of the floating object highly depends on the amplitude, frequency, and shape of the EWOD signal. There exists an optimal frequency and amplitude that maximizes the propulsion speed.

These behaviors can be qualitatively explained using a scaling analysis between the propulsion speed and Stokes drift, although the complete mathematical model is still open. Among the three signal shapes (sinusoidal, triangular, and modified square signals) of the same RMS value, the modified square signal shows the fastest propulsion speed throughout the tested frequency range (10 Hz ~ 1 kHz). These phenomena are also explained by the measured oscillation amplitudes and Stokes drift relations. Additionally, it is shown that a wider EWOD electrode generates a faster propelling speed. Finally, a wireless powering method for EWOD is introduced. With stacked planar receiver coils and an amplitude modulated signal, a wirelessly powered EWOD propulsion is realized.

3.0 PROPULSION BY CHEERIOS EFFECT

The Cheerios effect is an everyday phenomenon named after observations of cereal flakes floating in milk tending to aggregate and stick to the sidewall of the bowl[86, 87]. This phenomenon is not restricted to cereal flakes only. In fact, most small floating objects have a tendency to move away from or toward the sidewall depending on the surface wettability and other properties. The Cheerios effect is also generally known as lateral capillary force. In the presence of the floating objects, the air-liquid interface is distorted from its original shape, which generates a lateral force enabling the floating objects to move. As mentioned in subsection 1.1.2, some water-dwelling creatures harness this phenomenon to climb up the inclined meniscus forming at the water bank[28, 88]. By using only typical propulsion methods, such as sliding their limbs, these creatures are unable to climb the slippery meniscus[6]. Instead, these small animals have developed special tricks whereby they change their posture and distort the adjacent interfaces to generate a lateral force. In Fig. 3, for example, the waterlily leaf beetle simply bends its back and distorts the adjacent interfaces to climb the slippery meniscus[28]. In addition, the Cheerios effect governs a variety of interaction behaviors between floating objects in the processes of 2-dimensional array or monolayer self-assembly on the fluid-fluid interface[89-91].

In this chapter, theoretical models for the capillary interactions (Cheerios effect) in four configurations are reviewed. Numerical calculations for the case of two cylinders at small separation are compared with an asymptotic solution and experimental data. The effects of wettability and density are discussed. In addition, on-demand controlling methods (electrowetting

and dielectrowetting principles) are used to alter wettability in order to achieve active control of the Cheerios effect.

3.1 THEORETICAL MODELS

Current studies have been performed to understand the Cheerios effect phenomenon in different configurations. Four common physical configurations are interactions between (1) two infinite vertical walls, (2) two vertical circular cylinders, (3) two spheres, and (4) a sphere and a vertical wall. A simple and common understanding in these configurations is that attraction or repulsion solely depends on the surface wetting property[91-94]. For example, objects with similar wettability (i.e., both interacting objects are lyophobic or lyophilic) attract each other; otherwise, they repel away. However, this understanding is true for the case where two infinite vertical walls or vertical cylinders are not very close to each other. It may not be true for other configurations, such as interaction between a floating object and a vertical wall or between two floating objects. Vella and Mahadevan[86] challenged the theory with a simple experiment. By maintaining a similar surface wettability of two floating objects but changing the weight of one object, it was shown that the force between the objects could be reversed.

To better understand the Cheerios effect in these configurations, many theoretical models have been reported. One of the simplest models may be for the configuration between two infinite vertical walls[86, 95]. Since the walls are infinitely wide and high, the calculation is relatively simple with no vertical forces considered. When two vertical cylinders are submerged into a liquid, a 3-dimensional model is needed to describe the contact line on the cylinders. Using the Young-Laplace equation and the matched asymptotic expansions[96], Kralchevsky *et al.*[97] obtained an

asymptotic solution for the capillary force. The solution reduces to a simple expression when the separation distance is large. In this model, the vertical force balance is not required either. When two spherical objects are floating at the interface, the vertical force balance becomes important. Although the contact angle is fixed, the slope angle (the angle between the interface near the spheres and horizontal plane, which is critical to calculating the lateral force) can be different depending on the contact line position. Once the contact line position is determined from the vertical force balance, the calculation of the capillary force using the Nicolson superposition approximation is quite similar to that in the case of the two vertical cylinders[97-99]. Direct measurements of the lateral capillary force between vertical cylinders and between spheres agree well with theory[100, 101]. A theoretical model for the capillary interaction between a single spherical particle floating in the vicinity of an infinite vertical wall (which is the closest model to many Cheerios effect observations) was also developed[102]. This theory was partially verified by measuring the equilibrium position of the floating particle[103]. Moreover, Mansfield *et al.*[104] studied mutual attraction or repulsion of 2-dimensional strips. Some researchers[99, 105, 106] studied the configuration of horizontally floating two infinite cylinders where the vertical force balance becomes important to determine the contact line around the cylinder surfaces, although the capillary interaction can be described by a 2-dimensional model. The interaction between small, floating, horizontal cylinders with a finite length was also investigated[107].

The Cheerios effect occurs due to the horizontal component of the capillary force generated by the interface distortion. In order to find the horizontal component, the shape of the air-liquid interface deformed by objects or walls needs to be first determined. Let ξ be a function describing the shape (vertical position) of the interface:

$$z = \xi(x, y). \quad (3-1)$$

The interface shape obeys the Young-Laplace equation:

$$\nabla_{II} \left(\frac{\nabla_{II} \xi}{\sqrt{1 + |\nabla_{II} \xi|^2}} \right) = \frac{\Delta P}{\gamma_{al}} \quad (3-2)$$

where $\nabla_{II} \equiv \frac{\partial}{\partial x} \mathbf{e}_x + \frac{\partial}{\partial y} \mathbf{e}_y$ is the two-dimensional gradient operator, ΔP is the pressure difference across the air-liquid interface, and γ_{al} the air-liquid interfacial tension. For a small interfacial slope

$$|\nabla_{II} \xi|^2 \ll 1, \quad (3-3)$$

Eqn. (3-2) can be linearized to yield[108]

$$\nabla_{II}^2 \xi = \frac{\Delta \rho g}{\gamma_{al}} \xi = q^2 \xi, \quad (3-4)$$

where the density difference is $\Delta \rho = \rho_l - \rho_a \approx \rho_l$ and $q^{-1} = L_c \approx \sqrt{\gamma_{al}/\rho_l g}$ is the characteristic capillary length. For the air-water interface at room temperature, L_c is about 2.7 mm.

Once the interface shape is determined from Eqn. (3-4) along with the boundary conditions, the capillary force can be calculated by integrating the interfacial tension along the contact line and the hydrostatic pressure on the object:

$$\mathbf{F} = \mathbf{F}^{(\gamma)} + \mathbf{F}^{(P)}, \quad (3-5)$$

where

$$\mathbf{F}^{(\gamma)} = \oint_L \gamma_{al} d\mathbf{l}, \quad \mathbf{F}^{(P)} = \oint_S P d\mathbf{s}. \quad (3-6)$$

3.1.1 Model of two infinite vertical plates

Figure 32 illustrates the configuration of two infinite vertical plates at the air-liquid interface[86, 95]. The plate thickness is neglected for simplicity. The presence of the plates distorts the air-liquid interface. The plates have contact angles θ_1 and θ_2 and are apart in a horizontal distance L . The three regions divided by the two plates are labeled as $i = 1, 2$, and 3 . Note that the liquid in

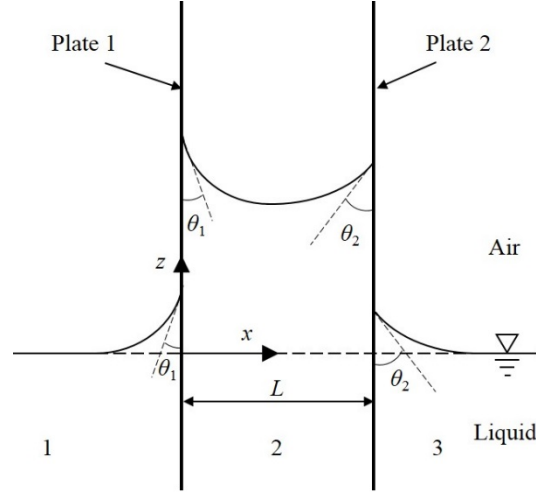


Figure 32. Configuration of two infinite vertical plates partially submerged in liquid[86]. The contact angles on the two plates are θ_1 and θ_2 . The separation distance between the two plates is L .

the three regions is connected. Equation (3-4) can be simplified to a 2-dimensional equation[86]

$$\frac{d^2\xi}{dx^2} = q^2\xi. \quad (3-7)$$

A general solution of Eqn. (3-7) is:

$$\xi_i(x) = A_i e^{x/L_c} + B_i e^{-x/L_c}. \quad (3-8)$$

In regions 1 and 3, the interface level as $x \rightarrow \pm\infty$ is 0, i.e.,

$$\xi_1(-\infty) = \xi_3(\infty) = 0. \quad (3-9)$$

The boundary conditions at the plate walls are given by the contact angles as

$$\xi'_1(0) = \cot \theta_1, \quad \xi'_3(L) = -\cot \theta_2. \quad (3-10)$$

Combining Eqns. (3-8), (3-9) and (3-10), one can obtain the interface profiles in regions 1 and 3 as

$$\xi_1(x) = L_c \cot \theta_1 e^{x/L_c}, \quad (3-11)$$

$$\xi_3(x) = L_c \cot \theta_2 e^{(L-x)/L_c}. \quad (3-12)$$

In region 2, the boundary conditions at the walls are

$$\xi_2'(0) = -\cot \theta_1, \quad \xi_2'(L) = \cot \theta_2, \quad (3-13)$$

which give an interface profile between the two plates as:

$$\xi_2(x) = L_c \frac{\cot \theta_1 \cosh \frac{L-x}{L_c} + \cot \theta_2 \cosh \frac{x}{L_c}}{\sinh \frac{L}{L_c}}. \quad (3-14)$$

Due to the same contact angles on both sides of each plate, the horizontal components of the surface tension force on both sides of the plate cancel out ($F^{(\nu)} = 0$). So the horizontal force is caused only by the hydrostatic pressure difference across the plate. The horizontal force acting on each plate can be calculated according to Eqn. (3-6) by integrating the hydrostatic pressure on the plate[86, 94]. For example, the force on the left plate in Fig. 32 is given as:

$$\begin{aligned} F_x &= \int_{-\infty}^{\xi_1(0)} \rho_l g y dy - \int_{-\infty}^{\xi_2(0)} \rho_l g y dy = \int_{\xi_2(0)}^{\xi_1(0)} \rho_l g y dy \\ &= \frac{1}{2} \rho_l g [\xi_1(0)^2 - \xi_2(0)^2]. \end{aligned} \quad (3-15)$$

By substituting Eqns. (3-11) and (3-14) into Eqn. (3-15), one has the horizontal force as:

$$F_x = -\frac{\gamma_{al}}{2} \left[\frac{(\cot \theta_1 \cosh \frac{L}{L_c} + \cot \theta_2)^2}{\sinh^2(\frac{L}{L_c})} - \cot^2 \theta_1 \right]. \quad (3-16)$$

Figure 33 shows the calculated interface profiles and horizontal force for two plates submerged in water. Both plates are hydrophilic or hydrophobic. In Fig. 33(a), both plates are hydrophilic with contact angles θ_1 and θ_2 ($\theta_1 < 90^\circ$ and $\theta_2 < 90^\circ$). The air-water interface (water level) in region 2 is higher than that at infinity ($x \rightarrow \pm\infty$), i.e., $H_2 > 0$. The water weight in region 2 is balanced by the upward vertical component of the capillary force at the contact line. This phenomenon is commonly known as capillary action or capillarity. Using the Young-Laplace equation, one can easily find that the water pressure P between the plates is smaller than the atmospheric pressure P_a . In region 2, the water surface is higher ($H_2(0) > H_1(0)$ and $H_2(L) > H_3(L)$) and the pressure is smaller ($P < P_a$), so the plates are pushed toward each other (attracting

each other). In Fig. 33(b), on the contrary, the interface in region 2 is lower than the zero level ($H_2 < 0$) when both plates are hydrophobic ($\theta_1 > 90^\circ$ and $\theta_2 > 90^\circ$). The cavity between the plates creates an upward, buoyancy-like force that is balanced by the downward vertical component of the capillary force at the contact line. Similarly to the hydrophilic case in region 2, $P_a < P$ can be obtained from the Young-Laplace equation. Since the water level in region 2 is lower ($H_2(0) < H_1(0)$ and $H_2(L) < H_3(L)$) and the pressure in regions 1 and 3 is greater than P_a ($P > P_a$), the two plates also attract each other. Figure 33(c) shows the horizontal force vs. the separation for the plates with similar wettability, which is calculated from Eqn. (3-16). Positive

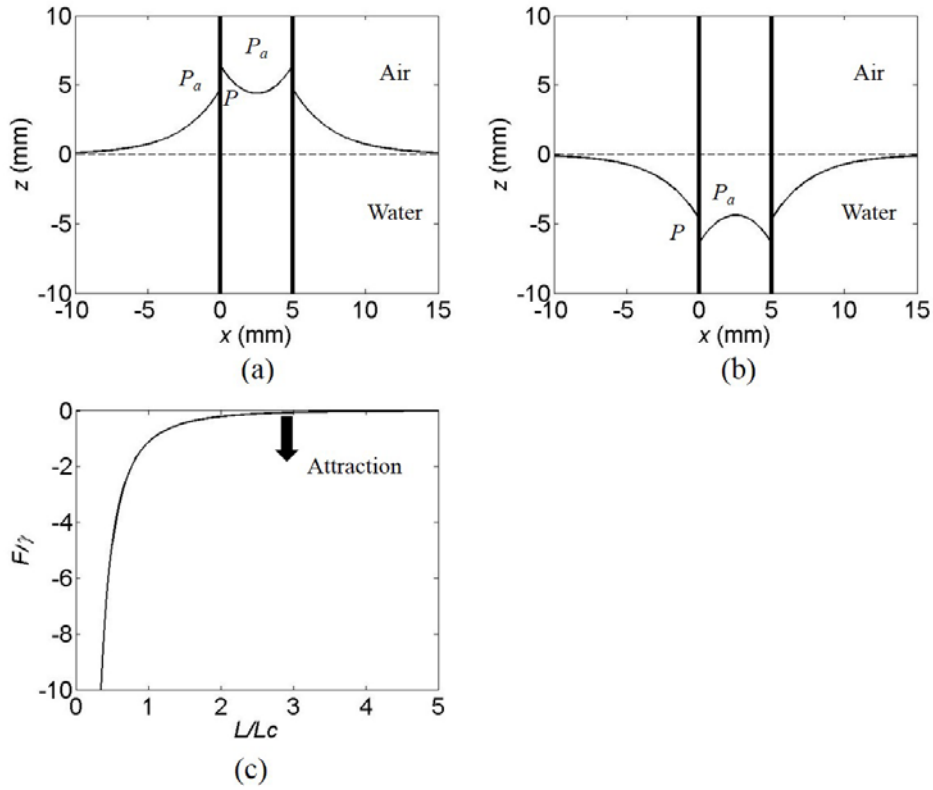


Figure 33. Two vertical plates submerged in water with similar wettability. (a) Interface profiles near two hydrophilic plates; and (b) two hydrophobic plates. (c) Horizontal component of the dimensionless force between the plates vs. separation ($\theta_1 = 45^\circ$ and $\theta_2 = 60^\circ$). In (a) and (b), the thick solid lines represent the plates; the black dashed line denotes the water level at infinity; and the thin solid lines denote the distorted air-water interface.

means repulsive while negative means attractive. No matter what the separation distance is, the force is always attractive. In particular, it increases quickly as the two plates come closer.

For the plates with opposite wettability (i.e., one plate is lyophilic and the other is lyophobic), the force behavior is much more complicated. Figure 34(a) shows the interface profiles for $\theta_1 < 90^\circ$, $\theta_2 > 90^\circ$ and $\theta_1 + \theta_2 < 180^\circ$ when the two plates submerged in water are a moderate distance apart. The left contact line in region 2 is a little lower than the contact line in region 1 ($H_2(0) < H_1(0)$) but the right contact line is higher than the contact line in region 3

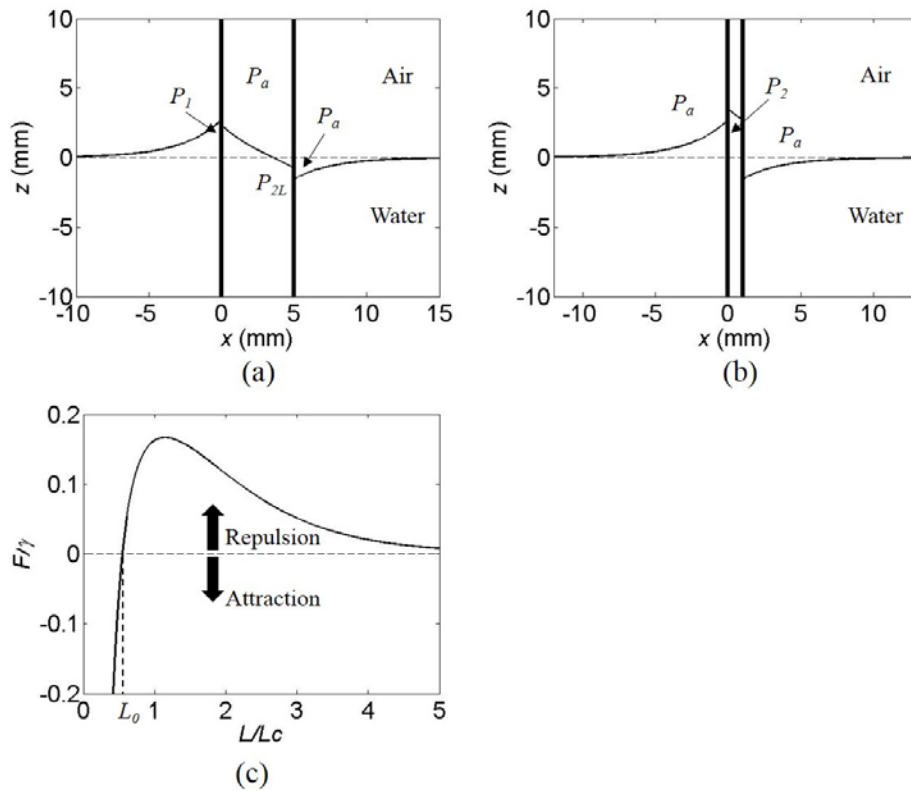


Figure 34. Two vertical plates with opposite surface wettability and $\theta_1 + \theta_2 \neq 180^\circ$. Interface profiles for (a) a moderate separation; and (b) a small separation between the plates. (c) Horizontal component of the dimensionless force between the plates vs. separation ($\theta_1 = 45^\circ$ and $\theta_2 = 120^\circ$). In (a) and (b), the thick solid lines represent the plates; the black dashed line indicates the liquid level at infinity; and the thin solid lines denote the distorted air-water interface.

($H_2(L) > H_3(L)$). One can easily find that $P_a > P_1$ and $P_{2L} > P_a$. On the left plate, in the small vertical gap between $H_1(0)$ and $H_2(0)$, P_1 is smaller than P_a . This generates a net force toward the left. Similarly, on the right plate, P_{2L} is larger than P_a such that a net force toward the right is generated. As a result, the two plates repel each other. When the two plates become very close (Fig. 34(b)), the interface in region 2 becomes much higher ($H_2(0) > H_1(0)$ and $H_2(L) > H_3(L)$). The two plates push each other because the pressures in regions 1 and 3 are larger than the pressure between the plates ($P_a > P_2$). Note that when the two plates have opposite wettability and $\theta_1 + \theta_2 > 180^\circ$, the interface in region 2 will be lowered. This results in repulsion at a large separation and attraction at a small separation. Figure 34(c) is the force curve for the plates with opposite wettability ($\theta_1 < 90^\circ$, $\theta_2 > 90^\circ$, and $\theta_1 + \theta_2 \neq 180^\circ$). In the large separation, the force is repulsive and small. It increases as the separation L decreases. Once the repulsive force reaches a peak, it decreases rapidly and becomes attractive when the distance becomes very small. There exists a zero force point at $L = L_0$, which depends on the contact angles on the two plates.

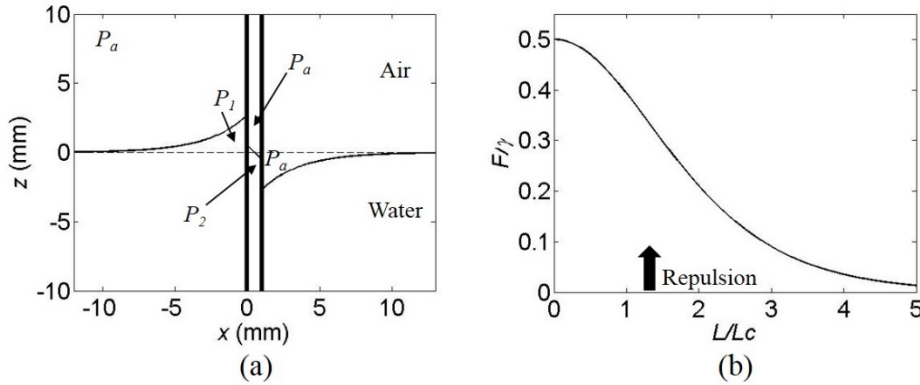


Figure 35. Two vertical plates submerged in water with opposite surface wettability and $\theta_1 + \theta_2 = 180^\circ$. (a) Interface profile; (b) horizontal component of the dimensionless force vs. separation ($\theta_1 = 45^\circ$ and $\theta_2 = 135^\circ$). In (a), the thick solid lines represent the plates; the black dashed line indicates the liquid level at infinity; and the thin solid lines denote the distorted air-water interface.

$\theta_1 + \theta_2 = 180^\circ$ is a special case where the middle point of the interface in region 2 always stays at the zero level no matter how close the two plates are (Fig. 35(a)). Because the pressure in region 2 is always greater than that in regions 1 and 3 ($P_a > P_1$ for the left plate and $P_2 > P_a$ for the right plate), the plates always repel each other (Fig. 35(b)). The repulsive force is small when the two plates are far apart. It increases as the separation L becomes smaller. However, it does not change the sign of the force even when L approaches zero.

In summary, two infinite plates attract each other when both of them are lyophilic or lyophobic, while they repel each other when the surface wettability is opposite and the distance between plates is not very small.

3.1.2 Model of two vertical cylinders

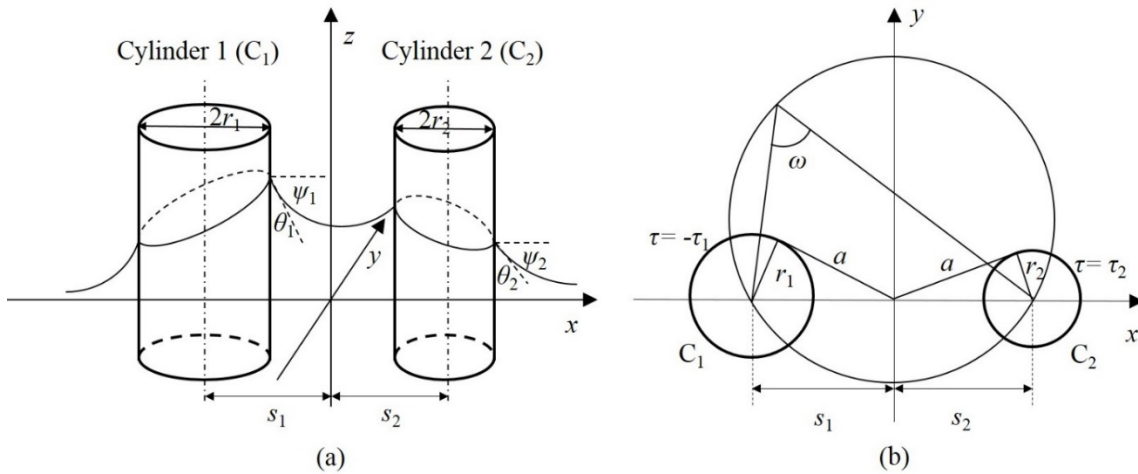


Figure 36. (a) Configuration of two vertical cylinders partially submerged in liquid[97]; (b)

Bipolar coordinates on plane xy [96].

When two cylinders are vertically submerged into liquid, as shown in Fig. 36(a), Eqn. (3-4) can be written as

$$\frac{d^2\xi}{dx^2} + \frac{d^2\xi}{dy^2} = q^2\xi. \quad (3-17)$$

Due to the capillary interaction between the cylinders, the contact lines on the cylinders are not horizontal. Otherwise, no horizontal force could be generated because the integrals in Eqn. (3-6) would be zero. The capillary force calculation can be performed in the following two regimes based on the separation distance between the cylinders: small or moderate separation and large separation.

3.1.2.1 Cylinders spaced at a small or moderate separation

The geometry of the system suggests the use of the bipolar coordinates (τ, ω, z) ([96], Fig. 36(b)):

$$x = a \frac{\sinh \tau}{\cosh \tau - \cos \omega}, \quad y = a \frac{\sin \omega}{\cosh \tau - \cos \omega}, \quad (3-18)$$

where

$$a^2 = s_1^2 - r_1^2 = s_2^2 - r_2^2. \quad (3-19)$$

In the bipolar coordinates, Eqn. (3-17) is converted to

$$(\cosh \tau - \cos \omega)^2 \left(\frac{\partial^2 \xi}{\partial \tau^2} + \frac{\partial^2 \xi}{\partial \omega^2} \right) = (qa)^2 \xi(\tau, \omega). \quad (3-20)$$

Note that τ is mathematically defined in Eqn. (3-18), though it is not easy to show it graphically in Fig. 36. Since only the interface profiles on the cylinder surfaces are required to calculate the lateral capillary force, one can only look for a solution of Eqn. (3-20) in the region close to the cylinders with ignoring the far field.

When two cylinders are spaced at a small or moderate distance ($(qa)^2 \ll 1$), the following mathematical description is valid [97]:

$$(\cosh \tau - \cos \omega)^2 \gg (qa)^2. \quad (3-21)$$

Now Eqn. (3-20) reduces to

$$\frac{\partial^2 \xi}{\partial \tau^2} + \frac{\partial^2 \xi}{\partial \omega^2} = 0. \quad (3-22)$$

On the cylinder surfaces, the boundary conditions in the bipolar coordinates can be expressed as[96]

$$\left. \frac{\partial \xi}{\partial \tau} \right|_{\tau=-\tau_i} = (-1)^i \frac{a}{\cosh \tau - \cos \omega} \Big|_{\tau=-\tau_i} \sin \psi_i, \quad i = 1, 2 \quad (3-23)$$

where ψ_i is the slope angle. For the vertical cylinders, ψ_i equals $(90^\circ - \theta_i)$ which is positive when $\theta_i < 90^\circ$ and is negative when $\theta_i > 90^\circ$. One can obtain a solution of Eqn. (3-22) with Eqn. (3-23) in the form of the Fourier series [97]:

$$\begin{aligned} \xi_i(\tau, \omega) = & C_0 + Q_i \ln(2 \cosh \tau - 2 \cos \omega) \\ & + \sum_{n=1}^{\infty} C_n^{(i)} \cosh n[\tau - (-1)^i \tau_i] \cos n\omega, \quad i = 1, 2 \end{aligned} \quad (3-24)$$

where

$$C_0 = (Q_1 - Q_2)A - (Q_1 + Q_2) \ln(\gamma_e qa) \quad (3-25)$$

$$A = \sum_{n=1}^{\infty} \frac{1 \sinh n(\tau_1 - \tau_2)}{n \sinh n(\tau_1 + \tau_2)} \quad (3-26)$$

$$Q_i = r_i \sin \psi_i \quad (3-27)$$

$$C_n^{(i)} = \frac{2(Q_2 - Q_1) (-1)^i \sinh n\tau_j}{n \sinh n(\tau_1 + \tau_2)}, \quad i, j = 1, 2; i \neq j, n = 1, 2, 3, \dots \quad (3-28)$$

In Eqn. (3-25) the Euler-Mascheroni constant is $\gamma_e = 1.781\dots$ [109].

As shown in Fig. 37[97], let $z = \xi(\varphi)$ be the vertical position of the contact line on the cylinder surface, where φ is the azimuthal angle on the xy plane. The position vector to the contact line is

$$\mathbf{R}(\varphi) = r_i \cos \varphi \mathbf{e}_x + r_i \sin \varphi \mathbf{e}_y + \xi(\varphi) \mathbf{e}_z. \quad (3-29)$$

In the bipolar coordinates, τ is constant on the cylinder surface. ω and φ are related as

$$\tan \omega = \frac{\sin \varphi}{r_i / (s_1 + s_2) - \cos \varphi}. \quad (3-30)$$

The line element along the contact line is

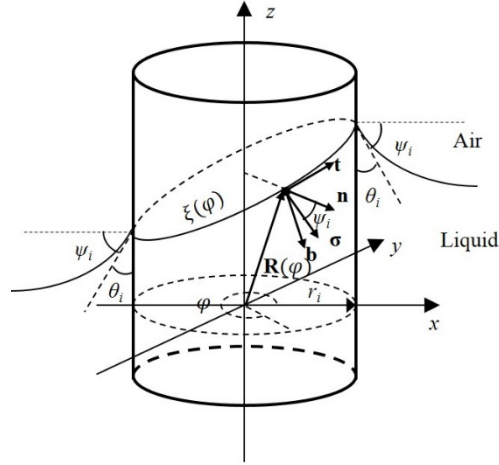


Figure 37. Contact line on the left cylinder when the separation between the two cylinders is small[97]. The second cylinder is located on the right (not shown).

$$dl = \chi d\varphi, \text{ where } \chi = \left| \frac{d\mathbf{R}}{d\varphi} \right| = \sqrt{r_i^2 + \left(\frac{d\xi}{d\varphi} \right)^2}. \quad (3-31)$$

The unit vector tangential to the contact line is described as

$$\mathbf{t} = \frac{1}{\chi} \frac{d\mathbf{R}}{d\varphi} = \frac{1}{\chi} \left(-r_i \sin \varphi \mathbf{e}_x + r_i \cos \varphi \mathbf{e}_y + \frac{d\xi}{d\varphi} \mathbf{e}_z \right), \quad (3-32)$$

the unit vector normal to the cylinder surface is

$$\mathbf{n} = \cos \varphi \mathbf{e}_x + \sin \varphi \mathbf{e}_y, \quad (3-33)$$

and the unit vector \mathbf{b} that is normal to the nt plane can be defined as

$$\mathbf{b} = \mathbf{t} \times \mathbf{n}. \quad (3-34)$$

The vector form of surface tension $\boldsymbol{\gamma}_{al}$, which is placed on the bn plane, can be written as

$$\boldsymbol{\gamma}_{al} = \gamma_{al} (\sin \psi_i \mathbf{b} + \cos \psi_i \mathbf{n}). \quad (3-35)$$

Then the horizontal surface tension is

$$(\boldsymbol{\gamma}_{al})_x = \boldsymbol{\gamma}_{al} \cdot \mathbf{e}_x = \gamma_{al} \left(\cos \varphi \cos \psi_i - \frac{1}{\chi} \frac{d\xi}{d\varphi} \sin \varphi \sin \psi_i \right). \quad (3-36)$$

Substituting Eqn. (3-36) into Eqn. (3-6), one can derive

$$F_x^{(y)} = -2\gamma_{al} \sin \psi_i \int_0^\pi \frac{d\xi}{d\varphi} \sin \varphi d\varphi + 2\gamma_{al} \cos \psi_i \int_0^\pi \chi \cos \varphi d\varphi. \quad (3-37)$$

A numerical calculation shows that for small cylinders $((qr_i)^2 \ll 1)$, the second integral on the right-hand side of Eqn. (3-37) is much smaller than the first integral[97]. By substituting Eqn. (3-24) into Eqn. (3-37), one may obtain $F_x^{(\gamma)}$ for the small or moderate separation. The force due to hydrostatic pressure $F_x^{(P)}$ also needs to be calculated in order to obtain the total horizontal force. The hydrostatic pressure is given as

$$P = P_a - \rho_l g \xi, \quad (3-38)$$

where P_a is the atmospheric pressure. Substituting Eqn. (3-38) into Eqn. (3-6), one can obtain

$$F_x^{(P)} = -\rho_l g r_i \int_0^\pi \xi^2(\varphi) \cos \varphi d\varphi. \quad (3-39)$$

Finally, the horizontal force between two vertical cylinders can be expressed as:

$$\begin{aligned} F_x = & -2\gamma_{al} \sin \psi_i \int_0^\pi \frac{d\xi}{d\varphi} \sin \varphi d\varphi \\ & + 2\gamma_{al} \cos \psi_i \int_0^\pi \chi \cos \varphi d\varphi - \rho_l g r_i \int_0^\pi \xi^2(\varphi) \cos \varphi d\varphi. \end{aligned} \quad (3-40)$$

Kralchevsky *et al.*[97] compared the contributions of hydrostatic pressure and surface tension, and concluded that for small cylinders $((qr_i)^2 \ll 1)$, the ratio below is small:

$$F_x^{(P)} / F_x^{(\gamma)} \ll 1. \quad (3-41)$$

3.1.2.2 Cylinders spaced at a large separation

When two cylinders are apart at a large separation, the capillary interaction between the two cylinders is weak. One can assume that the interface on the cylinder surface is modeled by a linear equation and is a superposition of the interfaces distorted by the two isolated cylinders [98]:

$$\xi = \xi_1 + \xi_2. \quad (3-42)$$

When a single vertical cylinder is isolated, the interface profile can be obtained by solving Eqn. (3-4), which yields a modified Bessel function solution in the cylindrical coordinates as

$$\xi_i = Q_i K_0(qd), \quad (3-43)$$

where K_0 is the modified Bessel function of zeroth order and d is the distance from the cylinder axis. When $d = r_i$, ξ_{i0} denotes the contact line on the cylinder surface. When the two cylinders are far from each other,

$$a \gg r_i \text{ and } s_i \gg r_i. \quad (3-44)$$

Thus,

$$s_1 \approx s_2 = s = \frac{L}{2}. \quad (3-45)$$

So the interface profile on a single cylinder surface (for example, for cylinder 2) is

$$\xi_2 = \xi_{20} + Q_1 K_0(qL), \quad (3-46)$$

where ξ_{20} is the elevation of the contact line on isolated cylinder 2 and L the distance from the axis of cylinder 1. On the cylinder surface, one can derive

$$\frac{d\xi}{d\varphi} = 2qr_1r_2 \sin \psi_1 K_1(qL) \sin \varphi. \quad (3-47)$$

By substituting Eqn. (3-47) into Eqn. (3-40) and neglecting $F_x^{(P)}$ for small cylinders ($(qr_i)^2 \ll 1$), an expression for $F_x^{(\gamma)}$ can be obtained as[99]:

$$F_x \approx F_x^{(\gamma)} \approx -2\pi\gamma_{al}qQ_1Q_2K_1(qL). \quad (3-48)$$

Figures 38 and 39 show comparisons between experimental results[100] and numerical calculations based on Eqns. (3-24), (3-40) and (3-48). As capillary interactions between the two lyophilic cylinders partially submerged into water are shown in Fig. 38(a), the numerical calculation from Eqn. (3-48) fits perfectly at the large separation, and deviates as the separation decreases. The results from Eqns. (3-24) and (3-40), which are obtained with the assumption of small separation distances, fit better when the two cylinders are close to each other. In Fig. 38(b), however, when the two cylinders are in an 8×10^{-2} M sodium dodecyl sulfate (SDS) solution (γ_{SDS}

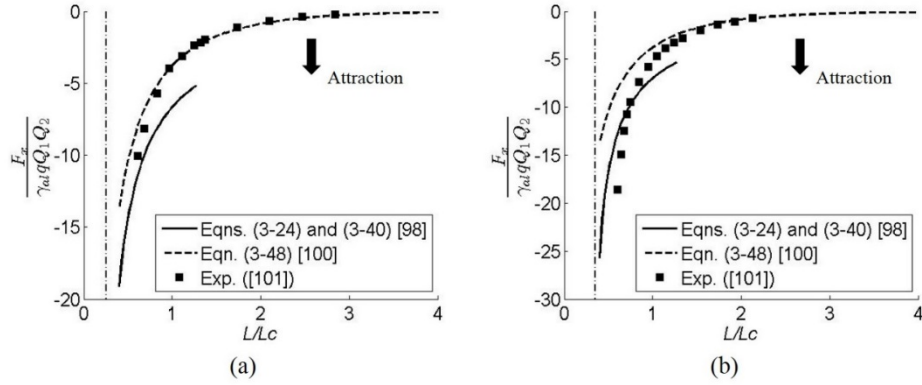


Figure 38. Comparison of theoretical predictions with experimental data for the dimensionless horizontal force between two vertical cylinders. Both cylinders are lyophilic (a) Both cylinders are partially submerged in water; (b) Both cylinders are partially submerged in an 8×10^{-2} M SDS solution. The dash-dot lines show the lower limit for possible separation between the cylinder centers. ($\theta_1 = \theta_2 = 0^\circ$, $r_1 = 370 \mu\text{m}$, $r_2 = 315 \mu\text{m}$, $\gamma_w = 72.4 \text{ mN/m}$, $\rho_w = 1.0 \text{ g/cm}^3$, $\gamma_{SDS} = 36.8 \text{ mN/m}$, and $\rho_{SDS} = 1.01 \text{ g/cm}^3$)

$= 36.8 \text{ mN/m}$, and $\rho_{SDS} = 1.01 \text{ g/cm}^3$), Eqn. (3-48) works only for the large separation and Eqns. (3-24) and (3-40) do not fit very well. Velev *et al.* suggested that this large deviation with the 8×10^{-2} M SDS solution may be caused by a nonlinear effect associated with the dimensionless radii qr_i , which are larger than those in pure water[100].

Figure 39 shows force-separation curves for the two cylinders having opposite wettability ($\theta_1 = 0^\circ$ and $\theta_2 = 99^\circ$). Equation (3-48) agrees well with the experimental data for the large separation. Velev *et al.* found that the measured horizontal force decreases at the small separation and predicted that the force might change from repulsion to attraction at a much smaller separation[100]. However, Eqn. (3-48) does not change sign at any separation because it uses a linear approximation and neglects the contact line elevation caused by the capillary interaction between the cylinders. The numerical calculation using Eqns. (3-24) and (3-40) fairly predicts the

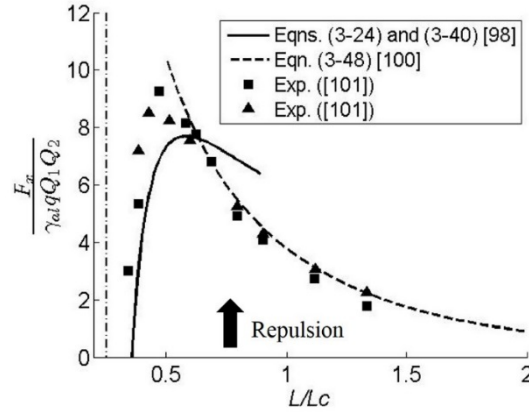


Figure 39. Comparison of theoretical predictions and experimental data for the horizontal force between two vertical cylinders partially submerged in water. The two cylinders have the opposite wettability. The dash-dot line shows the lower limit for possible separation between the cylinder centers. ($\theta_1 = 0^\circ$, $\theta_2 = 99^\circ$, $r_1 = 370 \mu\text{m}$, $r_2 = 315 \mu\text{m}$, $\gamma_w = 72.4 \text{ mN/m}$)

capillary force at small separation. Furthermore, the calculation predicts that the force direction is reversed when the two cylinders come very close to each other.

Comparing Fig. 38 with Fig. 33(c) and Fig. 39 with Fig. 34(c), one can find that the overall trends for the vertical walls model and vertical cylinders model are very similar: objects with similar wettability (lyophilic-lyophilic or lyophobic-lyophobic) attract each other; objects with opposite wettability repel each other at large separation but attract at small or moderate separation. Similar to the results shown in Fig. 35(b), the numerical calculation shows that when $\theta_1 + \theta_2 = 180^\circ$ the force between the two cylinders is always repulsive and does not change its direction no matter how close the two cylinders are.

3.1.3 Model of two floating spherical particles

Consider two small spherical particles with radii of R_1 and R_2 floating at the air-liquid interface ([97], Fig. 40(a)). The radii of the contact lines on the particle surfaces are r_1 and r_2 . Similar to the aforementioned two-cylinder model, $F_x^{(P)}/F_x^{(V)}$ is small for small spheres ($(qR_i)^2 \ll 1$), so $F_x^{(P)}$ can be neglected. If two spherical particles generate the same contact line shape as the cylinders do, the horizontal forces generated by the spherical particles will equal those generated by the cylinders because $F_x^{(V)}$ depends solely on the interface shape close to the cylinders.

In this case, one can imagine that the two spherical particles are replaced by two vertical fictitious cylinders with radii r_1 and r_2 ([97], Fig. 40(b)). As shown in the two-cylinder model, the contact lines are not horizontal. The inclination of the contact line is significant when the two

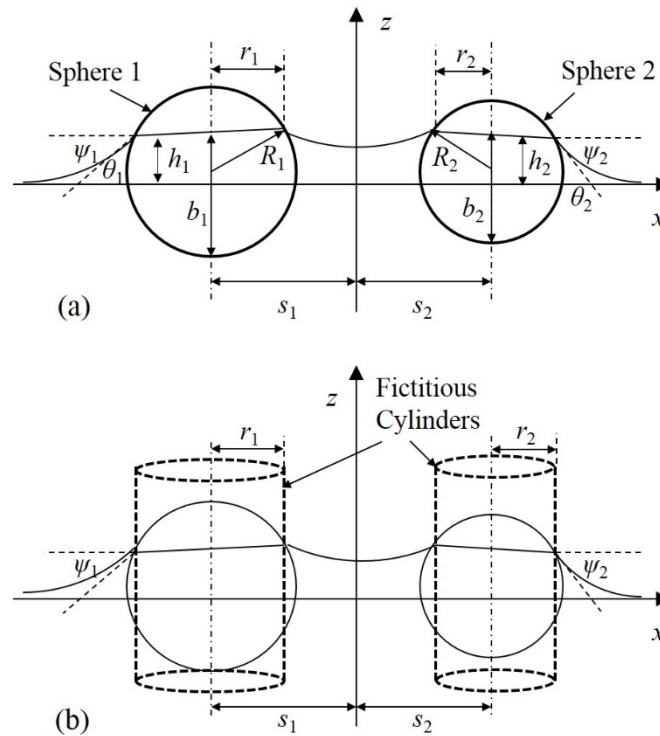


Figure 40. (a) Configuration of two small spherical particles floating at the air-liquid interfaces[97]; (b) The two fictitious cylinders generate the same interface profiles[97].

cylinders are close to each other, even though it becomes small at large separation, because the contact lines have plenty of room to move vertically. However, the inclination of the contact lines for small spherical particles would not be large since it is restricted by the size and curvature of the particles. One can infer that Eqn. (3-48), which is used to calculate the capillary force between the cylinders at large separation, is suitable for calculating the horizontal force between the two floating spherical particles in the entire range of separation distance, as follows:

$$F_x \approx -2\pi\gamma_{al}qQ_1Q_2K_1(qL). \quad (3-49)$$

Kralchevsky et al.[97] also proved from the energy method that Eqn. (3-49) is valid for calculating the horizontal force between the two floating spherical particles. Since r_i is always positive, the sign of capillary charge Q_i depends solely on ψ_i . If both particles have the same sign of ψ_i , the lateral capillary force between the two floating spheres is attractive; otherwise, the force is repulsive.

Since the contact line moves on the curved surface of the sphere, either r_i or ψ_1 is not constant. In order to calculate the capillary charge Q_i in Eqn. (3-49), one needs to use the vertical force balance. Because the inclination of the contact line is not significant, the contact line can be assumed horizontal to obtain geometric relations. The volume of the lower part of the sphere immersed in liquid is

$$V_l^{(i)} = \pi b_i^2(R_i - b_i/3). \quad (3-50)$$

where b_i is the height of the submerged part in liquid. R_i and b_i are related as

$$\frac{b_i - R_i}{R_i} = \cos(\psi_i + \theta_i). \quad (3-51)$$

Using $\beta_i = \psi_i + \theta_i$ and substituting Eqn. (3-51) into Eqn. (3-50) yields

$$V_l^{(i)} = \frac{1}{3}\pi R_i^3(2 + 3\cos\beta_i - \cos^3\beta_i). \quad (3-52)$$

The radius of the contact line can be expressed as

$$r_i = \sqrt{b_i(2R_i - b_i)}. \quad (3-53)$$

According to the vertical force balance, the vertical component of capillary force at the contact line is counterbalanced by the gravitational force, i.e.,

$$F_g^{(i)} = 2\pi\gamma_{al}r_i \sin \psi_i. \quad (3-54)$$

The gravitational force can be expressed as[110]

$$F_g^{(i)} = g[(\rho_l - \rho_i)V_l^{(i)} + (\rho_a - \rho_i)V_u^{(i)} - (\rho_l - \rho_a)\pi r_i^2 h_i], \quad (3-55)$$

where ρ_i is the particle density, $V_u^{(i)}$ the volume of the non-submerged part of the sphere, and h_i the contact line elevation with respect to the interface level at infinity ($x \rightarrow \pm\infty$). The relation for the sphere volume is:

$$V_l^{(i)} + V_u^{(i)} = \frac{4}{3}\pi R_i^3. \quad (3-56)$$

Because $\rho_l \gg \rho_a$, Eqn. (3-54) and Eqn. (3-55) can be combined and transformed to yield

$$Q_i = r_i \sin \psi_i \approx \frac{q^2}{2\pi} [V_l^{(i)} - D_i V^{(i)} - \pi r_i^2 h_i], \quad (3-57)$$

where the density correlation $D_i = \frac{\rho_l - \rho_a}{\rho_l - \rho_a}$. By substituting Eqns. (3-52) and (3-56) into Eqn. (3-

57), Eqn. (3-57) can be further expressed as

$$Q_i \approx \frac{q^2 R_i^3}{6} \left(2 - 4D_i + 3 \cos \beta_i - \cos^3 \beta_i - \frac{3r_i^2 h_i}{R_i^3} \right). \quad (3-58)$$

Due to extremely small weight (note that the particle weight is proportional to the cube of the radius), the interface deformation with small particles is very small. Kralchevsky and Nagayama[111] estimated that particles with a radius of less than 10 μm cannot deform the interface and, as a result, do not generate any horizontal force. As a result, ψ_i is small and $\beta_i \approx \theta_i$.

Eqn. (3-58) becomes

$$Q_i \approx \frac{q^2 R_i^3}{6} \left(2 - 4D_i + 3 \cos \theta_i - \cos^3 \theta_i - \frac{3r_i^2 h_i}{R_i^3} \right). \quad (3-59)$$

For the small particles ($(qR_i)^2 \ll 1$), the last term $\frac{3r_i^2 h_i}{R_i^3}$ in Eqn. (3-59) is small, so it can be neglected. As a result, Eqn. (3-59) finally becomes

$$Q_i \approx \frac{q^2 R_i^3}{6} (2 - 4D_i + 3 \cos \theta_i - \cos^3 \theta_i). \quad (3-60)$$

Combining Eqn. (3-49) with Eqn. (3-60), the horizontal capillary force vs. distance between particles can be calculated. Experimental measurements agree well with this calculation[101, 112].

In Eqn. (3-60), the contact angle θ_i , the particle radius R_i , and the density correlation D_i are the parameters to determine the lateral capillary force. Here, D_i is more important than R_i because it may affect both magnitude and sign of the capillary force while R_i changes only the magnitude. When the contact angle and size of particles are fixed, Q_i may change its sign depending on the particle density. This leads to a direction change in the horizontal force F_x . Figure 41 shows the force vs. separation for three pairs of spherical particles with different density combinations. The particle size and the contact angle are kept constant in calculation ($R_i = 100 \mu\text{m}$, $\theta_i = 60^\circ$). The solid line ($\rho_1 = \rho_2 = 2 \text{ g/cm}^3$) and dash-dot line ($\rho_1 = 2 \text{ g/cm}^3, \rho_2 = 0.5 \text{ g/cm}^3$) show

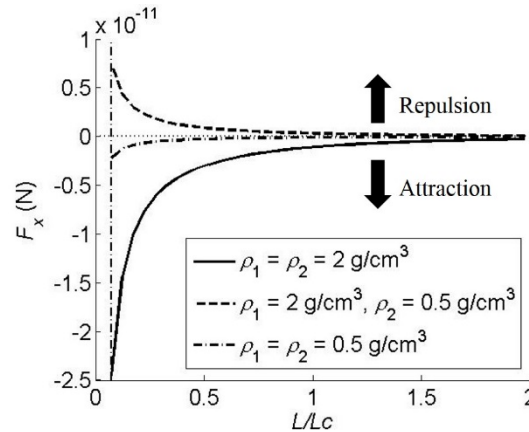


Figure 41. Horizontal force vs. separation for three pairs of spherical particles with different densities. The particle sizes and contact angles are kept constant in calculation ($R_1 = R_2 = 100 \mu\text{m}$, $\theta_1 = \theta_2 = 60^\circ$). The dash-dot line shows the lower limit of possible separation between the centers of the particles.

attraction between the two identical particles. However, between a heavy particle and a light particle ($\rho_1 = 2 \text{ g/cm}^3$ and $\rho_2 = 0.5 \text{ g/cm}^3$), the force becomes repulsive due to the opposite signs of capillary charges.

3.1.4 Model of floating spherical particle and vertical wall

The last configuration for the Cheerios effect in this article is a spherical particle with capillary charge Q floating in the vicinity of an infinite vertical wall. In order to find the horizontal capillary force between the wall and particle, one may first consider a simple case where the contact angle at the wall is fixed at $\theta_w = 90^\circ$, i.e., the boundary condition is

$$\xi_0'(0) = 0 \quad (3-61)$$

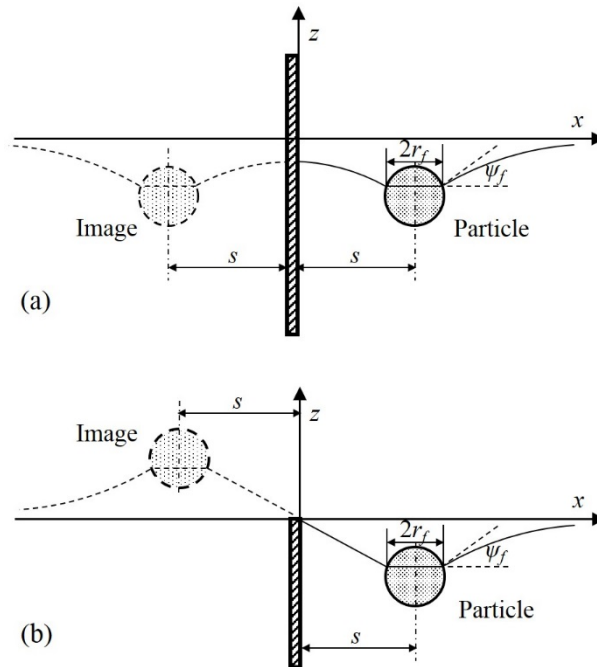


Figure 42. Capillary image force between the floating particle and its image[102]. (a) Fixed contact angle at the wall ($\theta_w = 90^\circ$); (b) Fixed contact line at the wall ($\xi_0'(0) = 0$).

Due to the zero slope at the wall, the mirror image method can be used to find the capillary force: the second identical particle (mirror image) floats at the distance $2s$ from the original one ([102], Fig. 42(a)). If the vertical wall is removed in Fig. 42(a), the interface should not change. Since the two particles (real and imaginary) are identical, the capillary charges of the two particles are also equal to each other ($Q_1 = Q_2 = Q$). As derived in the two-sphere model, the capillary force between these two particles is attractive:

$$F_x = -2\pi\gamma_{al}qQ^2K_1(2qs). \quad (3-62)$$

The capillary charge Q can be calculated by Eqn. (3-59). Since the interface elevation caused by the wall is zero and the elevation caused by the floating particle is negligibly small, the term $\frac{3r_i^2h_i}{R_i^3}$ can be ignored. In addition, ψ_i is small due to the small size and weight of the particle. As a result, Eqn. (3-59) can be reduced to Eqn. (3-60).

One may ask whether the capillary force can become repulsive for the wall-sphere interaction. When the boundary condition becomes

$$\xi_0(0) = 0, \quad (3-63)$$

which means the contact line at the wall is pinned to the zero elevation, the force becomes repulsive. In practice, this boundary condition can be realized when the contact line is attached to the edge of a vertical plate or to the boundary between hydrophilic and hydrophobic regions on the surface of the wall[102]. Using symmetry, one can imagine that the second particle (image) with the opposite capillary charge ($Q_1 = -Q_2 = Q$) is located at the distance $2s$ from the original one (Fig. 42(b)). Similar to the previous case, the interface should not change when the vertical wall is removed. The capillary force becomes repulsive:

$$F_x = 2\pi\gamma_{al}qQ^2K_1(2qs). \quad (3-64)$$

The above two cases are rare and special in reality, and are simply described by ‘Capillary Image Force’ [102]. The above method cannot be directly used for general and realistic conditions where the contact angle is not fixed just to 90° but can be any angle over a wide range and the contact line is positioned to an arbitrary elevation.

The following discussion shows how to find solutions for more general boundary conditions: (1) fixed contact angle at the arbitrary value and (2) fixed contact line at the arbitrary position. Since the current scope is limited to the small interface slope, the Young-Laplace equation can be linearized (Eqn. (3-4)). For the inclined interface, one can seek a superposed solution:

$$\xi = \xi_0 + \xi_1, \quad (3-65)$$

where ξ_0 is the deformation of interface created by the particle when $\theta_w = 90^\circ$ or $\xi_0(0) = 0$ and ξ_1 is the deformation of interface formed near the wall in the absence of the floating particle.

For the fixed contact angle at the wall, the boundary conditions are:

$$\xi_0'(0) = 0, \quad \xi_1'(0) = -\tan \psi_w. \quad (3-66)$$

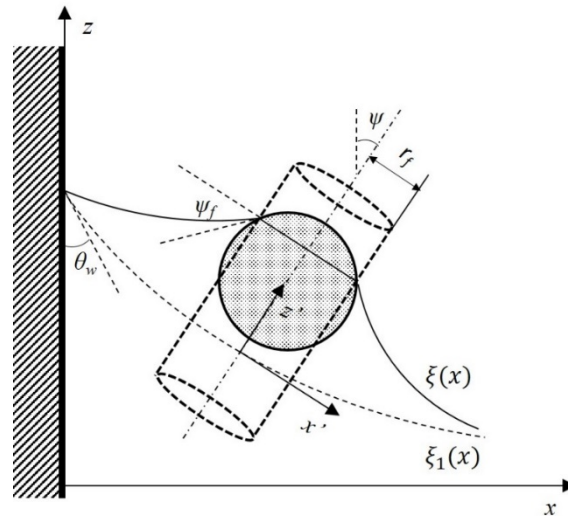


Figure 43. Configuration of the spherical particle and vertical wall [102]. The particle can be modeled and analyzed using the fictitious cylinder.

Similarly, the boundary conditions for the fixed contact line at the wall are:

$$\xi_0(0) = 0, \quad \xi_1(0) = H. \quad (3-67)$$

Then the interfaces formed by the wall without the floating particle can be expressed as:

$$\xi_1(x) = q^{-1} \tan \psi_w e^{-qx} \quad (\text{Fixed contact angle}); \quad (3-68)$$

$$\xi_1(x) = H e^{-qx} \quad (\text{Fixed contact line}). \quad (3-69)$$

One can use the concept of the fictitious cylinder with the radius r_f that is submerged in liquid (Fig. 43). The angle ψ between the centerline of the cylinder and the z axis is the local slope angle of the wall. One can introduce a new coordinate system (x', y', z') where the z' axis coincides with the cylinder axis:

$$\begin{aligned} \mathbf{e}'_x &= \cos \psi \mathbf{e}_x - \sin \psi \mathbf{e}_z; \\ \mathbf{e}'_y &= \mathbf{e}_y; \\ \mathbf{e}'_z &= \cos \psi \mathbf{e}_x + \sin \psi \mathbf{e}_z. \end{aligned} \quad (3-70)$$

Assume that the contact line on the cylinder surface is parallel to the x' axis. Similarly to the deriving procedure from Eqn. (3-29) to Eqn. (3-36), one can obtain $(\gamma_{al})_x$ in the (x', y', z') system as[102]:

$$(\gamma_{al})_x = \gamma_{al} \left[\cos \psi \left(\cos \varphi \cos \psi_f - \frac{1}{\chi} \frac{d\xi_0}{d\varphi} \sin \varphi \sin \psi_f \right) - \frac{1}{\chi} \sin \psi \sin \psi_f \right], \quad (3-71)$$

where ψ_f is the slope angle around the particle in the (x', y', z') coordinate. Substituting Eqn. (3-71) into Eqn. (3-6), one obtains

$$\begin{aligned} F_x^{(\gamma)} &= -2\pi\gamma_{al}r_f \sin \psi_f \sin \psi \\ &\quad - 2\gamma_{al} \sin \psi_f \int_0^\pi \frac{d\xi_0}{d\varphi} \sin \varphi d\varphi + 2\gamma_{al} \cos \psi \cos \psi_f \int_0^\pi \chi \cos \varphi d\varphi. \end{aligned} \quad (3-72)$$

The last term in Eqn. (3-72) is negligible for large separation[102]. Eqn. (3-72) becomes

$$F_x^{(\gamma)} \approx -2\pi\gamma_{al}r_f \sin \psi_f \sin \psi - 2\gamma_{al} \sin \psi_f \int_0^\pi \frac{d\xi_0}{d\varphi} \sin \varphi d\varphi. \quad (3-73)$$

For a small interface elevation,

$$\sin \psi \approx \tan \psi = - \left. \frac{d\xi_1}{dx} \right|_{x=s}. \quad (3-74)$$

Substituting Eqns. (3-68) and (3-69) into Eqn. (3-74), $\sin \psi$ in Eqn. (3-73) becomes

$$\sin \psi \approx \tan \psi_w e^{-qs} \quad (\text{Fixed contact angle}); \quad (3-75)$$

$$\sin \psi \approx qH e^{-qs} \quad (\text{Fixed contact line}). \quad (3-76)$$

To estimate the horizontal force due to the hydrostatic pressure $F_x^{(P)}$, one can use the approximation[102]

$$\xi(\varphi) \approx h_f + \frac{dh_f}{ds} r_f \cos \varphi \quad (3-77)$$

and substitute it into Eqn. (3-39) to obtain

$$F_x^{(P)} \approx \pi \gamma_{al} (qr_f)^2 h_f \frac{dh_f}{ds}. \quad (3-78)$$

ξ_0 , which is the interface deformation created by the floating particle when the imaginary particle floats at $2s$ separation, still needs to be found. Eventually, this information allows for discovery of the contact line elevation h_f and the total capillary force after substituting h_f into Eqns. (3-73) and (3-78). r_f and $\sin \psi_f$ are also required for finding the total horizontal force.

3.1.4.1 Fixed contact angle at the wall

If the elevation of the contact line is zero at the wall, Eqn. (3-59) is valid to calculate the capillary charge Q_f . For the typical inclined interface near the wall, however, the elevation of the contact line on the particle h_f is no longer small. As a result, the term $\frac{3r_i^2 h_i}{R_i^3}$ in Eqn. (3-59) cannot be neglected. The elevation of the contact line on the particle surface h_f can be given as:

$$h_f = q^{-1} \tan \psi_w e^{-qs} + h_{f0}, \quad (3-79)$$

where h_{f0} is the mean elevation of the contact line for a isolated particle floating at the flat air-liquid interface:

$$h_{f0} = \frac{1}{2\pi r_f} \oint_{C_f} \xi_0 dl. \quad (3-80)$$

For the two particles with capillary charges Q_1 and Q_2 , Eqn. (3-24) is used to compute the interface deformation close to the particles for small or moderate inter-particle separation ($(qa)^2 \ll 1$). By setting $Q_1 = Q_2$ in Eqn. (3-24) and using the relations of the bipolar coordinates, one obtains [102]

$$\xi_0^{in}(\omega) = Q_2 \left[\ln \frac{2}{\gamma_e q r_f} + \ln \frac{2}{\gamma_e 2qa^2 / (s - r_f \cos \omega)} \right], \quad (3-81)$$

where superscript 'in' denotes the solution in the inner region (close to the particle, $(qa)^2 \ll 1$).

Substituting Eqn. (3-81) into Eqn. (3-80) yields

$$h_{f0}^{in} = Q_2 \left[\ln \frac{2}{\gamma_e q r_f} + \ln \frac{2}{\gamma_e q (s+a)} \right]. \quad (3-82)$$

For the large inter-particle separation ($(qa)^2 \gg 1$), the superposition and approximation[98] are used to derive the interface shape for the two identical particles, i.e.,

$$\xi_0^{out}(\omega) = Q_f [K_0(qd_1) + K_0(qd_2)], \quad (3-83)$$

where d_i is the horizontal distance from the center of the sphere. Because the modified Bessel function can be written as

$$K_0(x) \approx \ln \frac{2}{\gamma_e x}, \quad (3-84)$$

the inner asymptote ($a \rightarrow 0$) of Eqn. (3-83) for small x is

$$(\xi_0^{out})^{in} \approx Q_f \left[\ln \frac{2}{\gamma_e q d_1} + \ln \frac{2}{\gamma_e q d_2} \right]. \quad (3-85)$$

By substituting Eqn. (3-83) into Eqn. (3-80), one can derive

$$h_{f0}^{out} = h_{f\infty} + Q_f K_0(2qs); \quad h_{f\infty} = Q_f \ln \frac{2}{\gamma_e q r_f}. \quad (3-86)$$

By comparing Eqn. (3-81) with Eqn. (3-85), one obtains a compound expression for ξ_0 :

$$\xi_0 = h_{f\infty} + Q_f K_0 \left(\frac{2qa^2}{s-r_f \cos \omega} \right). \quad (3-87)$$

Similarly, the compound expression for h_{f0} can be obtained by comparing Eqns. (3-82) and (3-86):

$$h_{f0} = h_{f\infty} + Q_f K_0(q(s+a)). \quad (3-88)$$

Then h_f becomes:

$$h_f = q^{-1} \tan \psi_w e^{-qs} + h_{f\infty} + Q_f K_0(q(s+a)). \quad (3-89)$$

From Eqn. (3-57), one can calculate the capillary charge of particle Q_2 as

$$Q_f = \frac{q^2}{6} [(3R_f - b_f)b_f^2 - 4D_f R_f^3 - 3r_f^2 h_f]. \quad (3-90)$$

Combining Eqns. (3-73), (3-75), (3-78), (3-87), (3-89), and (3-90), one can obtain the horizontal force for the fixed contact angle as [102]

$$F_x = -\pi \gamma_{al} \left[2qQ_f^2 K_1(2qs) + 2Q_f \tan \psi_w e^{-qs} + q(r_f \tan \psi_w e^{-qs})^2 \right]. \quad (3-91)$$

3.1.4.2 Fixed contact line at the wall

Similarly to the fixed contact angle at the wall, when the contact line is fixed to an arbitrary position at the wall,

$$h_f = H e^{-qs} + h_{f0}; \quad h_{f0} = \frac{1}{2\pi r_f} \oint_{C_f} \xi_0 dl. \quad (3-92)$$

For the small separation ($(qa)^2 \ll 1$), by setting $Q_1 = -Q_2 = -Q_f$, Eqn. (3-24) becomes

$$\xi_0^{in}(\omega) = Q_f \tilde{\tau}_f(\omega), \quad (3-93)$$

where

$$\tilde{\tau}_f(\omega) = \tau_f + 2 \sum_{n=1}^{\infty} \frac{1}{n} \tanh n\tau_f e^{-n\tau_f} \cos n\omega. \quad (3-94)$$

Similarly to Eqn. (3-81), Eqn. (3-93) can be rewritten in the form [102]:

$$\xi_0^{in}(\omega) = Q_f \left[\ln \frac{2}{\gamma_e q r_f} - \ln \frac{2}{\gamma_e q r_f e^{\tilde{\tau}_f}} \right]. \quad (3-95)$$

Substituting Eqn. (3-95) into Eqn. (3-92), one obtains

$$h_{f0}^{in} = Q_f \tau_f^*, \quad (3-96)$$

where

$$\tau_2^* = \tau_f + 2 \sum_{n=1}^{\infty} \frac{1}{n} e^{-2n\tau_f} \tanh n\tau_f. \quad (3-97)$$

Equation (3-96) can be rewritten in the form[102]

$$h_{f0}^{in} = Q_f \left[\ln \frac{2}{\gamma_e q r_f} - \ln \frac{2}{\gamma_e q r_f e^{\tau_f^*}} \right]. \quad (3-98)$$

When the inter-particle separation is large ($(qa)^2 \gg 1$), again by using the superposition approximation[98], one obtains

$$\xi_0^{out}(\omega) = h_{f\infty} - Q_f K_0(2qs). \quad (3-99)$$

From Eqn. (3-92), one derives

$$h_{f0}^{out} = h_{f\infty} - Q_f K_0(2qs). \quad (3-100)$$

Similarly to the fixed contact angle, one can compare Eqn. (3-95) with Eqn. (3-99) to obtain

$$\xi_0 = h_{f\infty} - Q_f K_0(qr_f e^{\tilde{\tau}_f}) \quad (3-101)$$

and compare Eqn. (3-98) with Eqn. (3-100) to find

$$h_{f0} = h_{f\infty} - Q_f K_0(qr_f e^{\tau_f^*}). \quad (3-102)$$

From Eqn. (3-92), h_f is

$$h_f = H e^{-qs} + h_{f\infty} - Q_f K_0(qr_f e^{\tau_f^*}). \quad (3-103)$$

Combining Eqns. (3-73), (3-76), (3-78), (3-90), (3-101), and (3-103), the horizontal force for the fixed contact line is finally obtained as[102]

$$F_x = -\pi\gamma_{al} \left[-2qQ_f^2 K_1(2qs) + 2Q_f q H e^{-qs} + q(r_f q H e^{-qs})^2 \right]. \quad (3-104)$$

Till now, the horizontal force between the vertical wall and floating sphere for fixed contact angle or fixed contact line boundary conditions has been obtained. The first term in Eqns. (3-91) and (3-104) is the capillary image force, shown as Eqns. (3-62) and (3-64). The second one originates from the superposition of the particle weight and the buoyancy force[102]. And the third term takes into account the pressure jump across the interface encircled by the contact line on the sphere[102].

As discussed in the introduction, contact angles θ_w and θ_f were considered the sole parameters by which to determine the direction of horizontal capillary force (i.e., the sign of F_x in Eqns. (3-91) and (3-104)). However, it's not necessarily true. In Eqns. (3-91) and (3-104), if the second term is divided by the third term, the results yield $\frac{2\sin\psi_f}{qr_f\tan\psi_w} e^{qs}$ and $\frac{2\sin\psi_f}{q^2r_fH} e^{qs}$, which are large for not small separation s . In addition, the absolute values of the second term dividing the first term in Eqns. (3-91) and (3-104) read $\left| \frac{\tan\psi_w e^{-qs}}{qQ_f K_1(2qs)} \right|$ and $\left| \frac{H e^{-qs}}{Q_f K_1(2qs)} \right|$ and are large for large s because the modified Bessel function ($K_1(2qs)$) decreases much faster than e^{-qs} as s increases. As a result, for not small separation s , the second terms in Eqns. (3-91) and (3-104) are dominant to determine the direction and magnitude of the horizontal capillary force. For example, the force is attractive if Q_f and $\tan\psi_w$ in Eqn. (3-91) or Q_f and H in Eqn. (3-104) have the same sign, but is repulsive if they have the opposite sign. Because r_f is always positive, one can make a general conclusion that for not small separation s , the force between a floating sphere and vertical wall is attractive if ψ_f and ψ_w have the same sign and is repulsive if they have the opposite sign.

In addition, ψ_w is solely determined by θ_w for a vertical wall, but θ_f is not the only parameter to determine ψ_f . Because the contact line elevation of the sphere contact line is small when the sphere is not close to the wall, the last term in Eqn. (3-59) is negligible at large s . It can

be observed from Eqn. (3-59) that, except for θ_f , the density correlation D_f (or particle density ρ_f) is another important parameter by which to determine the sign of ψ_f or Q_f . As a result, it can be inferred that, if some properties of the sphere (such as size and contact angle) and the properties of the air-liquid system (such as surface tension and densities of air and liquid) are fixed, contact angle at the wall θ_w (fixed contact angle boundary condition) or contact line elevation at the wall H (fixed contact line boundary condition) and density of the floating sphere ρ_f are both critical parameters in determining the horizontal capillary force between a floating sphere and a vertical wall.

Figure 44 shows the horizontal capillary force between floating spheres (buoyant and dense) and the vertical wall for different contact line elevations at the vertical wall. During calculation, the radius of the sphere R is 1 mm and the contact angle θ_f is 45° . As shown in Fig. 44(a), for a buoyant floating sphere ($\rho_f = 0.58 \text{ g/cm}^3$), the force is attractive when $H > 0$, while it becomes repulsive when $H < 0$. However, for a dense floating sphere ($\rho_f = 1.18 \text{ g/cm}^3$), the force

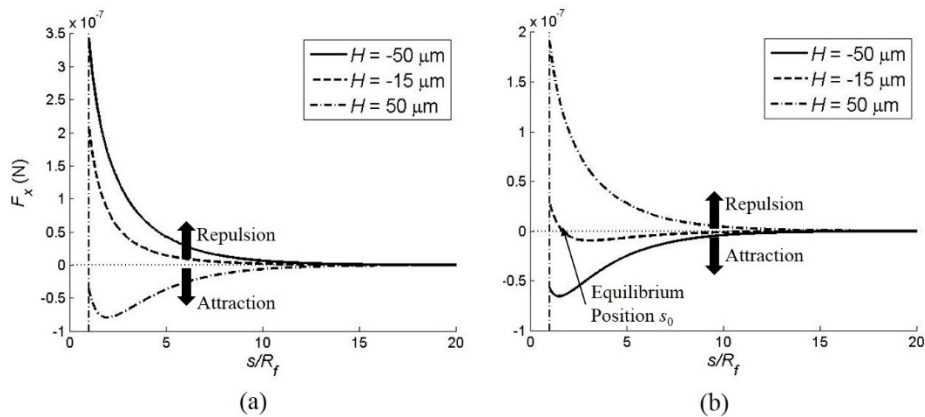


Figure 44. Horizontal force vs. separation in the wall-sphere capillary interaction for different wall contact line elevations. (a) Buoyant sphere ($\rho_f = 0.58 \text{ g/cm}^3$, $R_f = 1 \text{ mm}$, $\theta_f = 45^\circ$); (b) Dense sphere ($\rho_f = 1.18 \text{ g/cm}^3$, $R_f = 1 \text{ mm}$, $\theta_f = 45^\circ$). The dash-dot lines show the smallest separation between the particle center and wall.

direction is reversed for similar boundary conditions at large separation, i.e., repulsion for $H > 0$ and attraction for $H < 0$. When contact line elevation at vertical wall H is close to zero (i.e., dashed line in Fig. 44(b)), the situation is complicated. Due to the repulsive pure capillary image force for the fixed contact line boundary condition, the force may intersect the x -axis at some distance s_0 and become repulsive at smaller separation, which means there is an equilibrium (zero force) point located close to the wall. This point is stable (the particle has a tendency to stay at the zero force point) because the sphere is repelled if separation is smaller than s_0 while it is attracted if separation is larger than s_0 . The measurements (Velev *et al.* [103]) of the equilibrium point for the fixed contact line boundary condition agree with the theory well.

Figure 45 shows horizontal capillary force between floating spheres (buoyant and dense) and vertical wall for different wall contact angles. During calculation, the radius of the sphere R is 1 mm and contact angle θ_f is 45° . For a buoyant floating sphere ($\rho_f = 0.58 \text{ g/cm}^3$), the force is attractive when $\theta_w < 90^\circ$ but becomes repulsive when $\theta_w > 90^\circ$. However, the force direction is reversed for a dense floating sphere ($\rho_f = 1.18 \text{ g/cm}^3$) for similar boundary conditions; the force

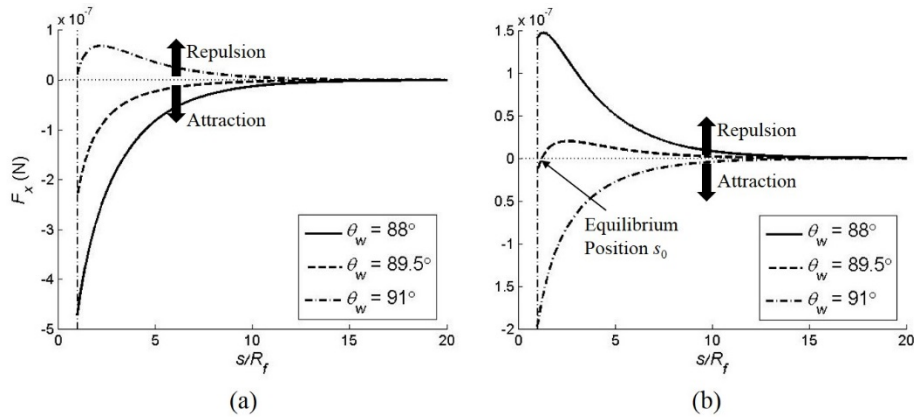


Figure 45. Horizontal force vs. separation in the wall-sphere capillary interaction for different wall contact angles. (a) Buoyant sphere ($\rho_f = 0.58 \text{ g/cm}^3$, $R_f = 1 \text{ mm}$, $\theta_f = 45^\circ$); (b) Dense sphere ($\rho_f = 1.18 \text{ g/cm}^3$, $R_f = 1 \text{ mm}$, $\theta_f = 45^\circ$). The dash-dot lines show the smallest separation between the particle center and wall.

becomes repulsive when $\theta_w < 90^\circ$ and attractive when $\theta_w > 90^\circ$. Similar to fixed contact line boundary condition, there may also exist an equilibrium (zero force) point for a fixed contact angle boundary condition (i.e., dashed line in Fig. 45(b)). But for the fixed contact angle boundary condition, the zero force point is not stable (the particle has tendency to move away from the zero force point) because the force is attractive if separation is smaller than s_0 while is repulsive if separation is larger than s_0 . Note, the surfaces of spheres during calculation in Fig. 45 are kept hydrophilic ($\theta_f = 45^\circ$), which shows that a hydrophilic wall does not guarantee attractive force with a hydrophilic floating sphere.

In summary, when the separation is not too small, the lateral capillary force is attractive if the slope angles at the wall ψ_w and on the floating particle ψ_f have the same sign, otherwise, the force is repulsive. Except for the contact angle of the vertical wall θ_w and that of the sphere θ_f , the sphere density ρ_f is another critical parameter in determining the direction of the capillary force between vertical wall and sphere. When the separation is small, the situation is much more complicated.

3.2 ELECTROWETTING-ASSISTED CHEERIOS EFFECT

3.2.1 Theory validation

Because the contact angle at wall θ_w is a critical parameter by which to determine the direction of the horizontal capillary force when properties of a floating particle are fixed, the EWOD method can be implemented to manipulate the surface wettability and to further control the direction of the horizontal capillary force between the vertical wall and the sphere.

Since Kralchevsky *et al.* [102] developed a theoretical model of horizontal interaction between vertical wall and floating sphere, some experimental results have been reported. Dushkin *et al.* [112] directly measured horizontal force for a fixed contact angle condition by using torsion balance. As discussed in Fig. 44(b), according to the theory, there may exist a stable equilibrium position for a fixed contact line boundary condition where the sphere experiences zero horizontal net force. Velev *et al.* [103] verified the theory by measuring the equilibrium position of the floating sphere for fixed contact line boundary condition. However, for the fixed contact angle boundary condition (for example, the contact angle modulated by EWOD), though there may also exist an equilibrium position, the position is not stable because the force is attractive for $s < s_0$ and repulsive for $s > s_0$. As a result, experimental measurement of the equilibrium position for fixed contact angle boundary condition is difficult. Here, an alternating method to validate the theory by implementing EWOD to the Cheerios effect is introduced. When the separation s between the vertical wall and the sphere is smallest ($s = R_f$ when the sphere contacts the wall), there exists a certain wall contact angle θ_w that results in a zero force between wall and floating sphere. By adjusting the applied voltage to EWOD, this contact angle is experimental compared with theoretical calculation.

Figure 46 shows a comparison between experimental results and theoretical prediction of the equilibrium point for a fixed contact angle boundary condition. The solid line in Fig. 46 is numerical calculation according to Eqn. (3-91). During calculation, the density of the sphere ρ_f sweeps from 1.00 g/cm³ to 1.20 g/cm³ with step of 0.001 g/cm³, while the radius and contact angle are fixed at 1 mm and 45° separately. For a certain sphere density, the contact angle at the vertical wall θ_w decreases from 120° with step of 0.1° and is recorded when the force changes from attractive to repulsive for the first time. During the experiment, in order to have spheres with

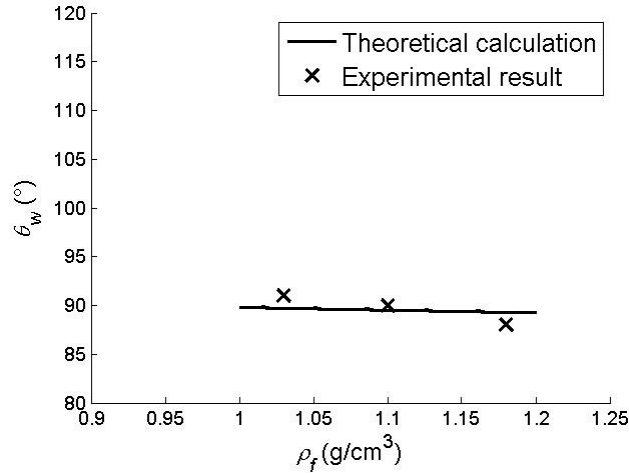


Figure 46. Comparison of experimental data and theoretical prediction of the zero force point for fixed contact angle boundary condition. Separation s is equal to R_f . Contact angle and radius of sphere θ_f and r_f are 45° and 1 mm for both experiment and calculation.

different densities, three resin spheres ($R_f = 1$ mm) with different wall thicknesses are prepared by 3D printing technology. The solid sphere has a density of 1.18 g/cm³, which is the same as the density of the resin. Two hollow spheres with wall thickness of 500 μm and 600 μm have densities of 1.03 g/cm³ and 1.10 g/cm³ separately. All spheres have contact angles of around 45° and negative slope angles at flat air-water interface. A silicon wafer covered by 2.5 μm parylene layer and thin Teflon® AF layer (~ 2000 Å) on the top is inserted into water as a vertical wall. Bare aluminum foil is used as a ground electrode to close the electrical circuit and is attached to the bottom of water container. Since all three spheres are dense and have negative slope angles, the spheres are initially attracted by the hydrophobic vertical wall at no external voltage. As EWOD voltage increases, the contact angle of the wall decreases. At a certain voltage, the force between the sphere and wall becomes zero. A further increase of the voltage results in a lower contact angle that results in repulsive force. The voltages of the zero force are recorded for spheres with different densities. Contact angles corresponding to these voltages are measured on the same EWOD

electrode with a sessile droplet sitting on it (configuration shown in Fig. 6(a)) and shown as cross symbols in Fig. 46. The theory and experimental results agree well.

By changing wall wettability of the vertical electrode by electrowetting, a floating object can be manipulated, i.e., attracted or repelled by the wall. When EWOD is off, the wall surface is hydrophobic, so the meniscus slope angle at the wall is negative ($\psi_w < 0$). As a result, the wall will repel an object with a positive slope angle ($\psi_f > 0$) (Fig. 47(a)) and attract an object with a negative slope angle ($\psi_f < 0$) (Fig. 47(c)). While EWOD is turned on at not low voltage, the wall can be switched to hydrophilic, which results in a positive slope angle ($\psi_w > 0$), so it can attract an object with a positive slope angle ($\psi_f > 0$) (Fig. 47(b)) and repel an object with a negative slope angle ($\psi_f < 0$) (Fig. 47(d)).

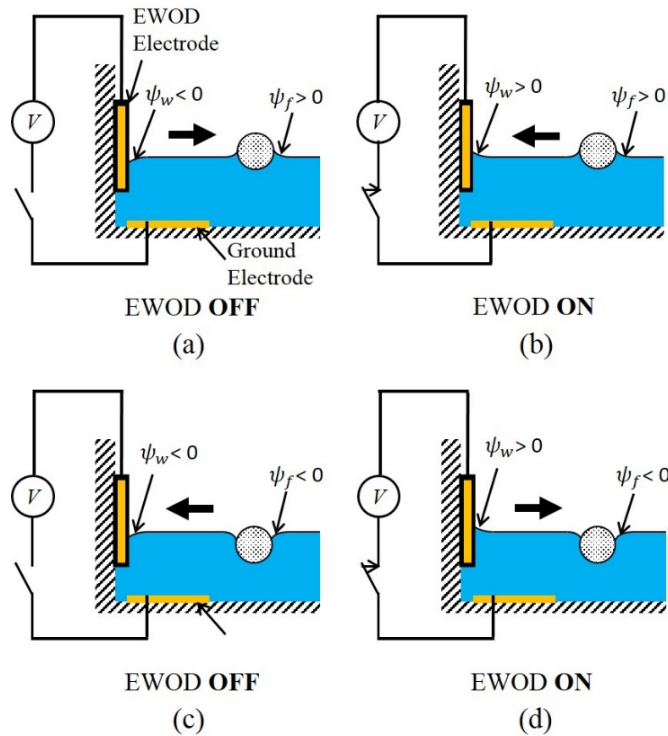


Figure 47. Sketch of EWOD-assisted Cheerios effect. (a) & (b) Floating sphere with a positive slope angle. (a) EWOD is OFF; (b) EWOD is ON. (c) & (d) Floating sphere with a negative slope angle. (c) EWOD is OFF. (d) EWOD is ON.

Figure 48 shows experimental verification of the above prediction. Two resin spheres ($R_f = 1 \text{ mm}$) with different densities are prepared by 3D printing technology. The solid one has a density of 1.18 g/cm^3 and a negative slope angle. The hollow one has $200 \mu\text{m}$ thick wall, which leads to reduced sphere density of 0.58 g/cm^3 and a positive slope angle. The contact angles of the spheres are measured to be about 45° . The vertical EWOD electrode acts as a wall. Bare aluminum foil is attached to the bottom of water container (not shown in Fig. 48). As shown in Fig. 48(a), when EWOD is turned on ($150 \text{ V}_{\text{DC}}$), the wall surface is hydrophilic, so the buoyant sphere (positive slope angle) is attracted and the dense one (negative slope angle) is repelled by the vertical wall. But when EWOD is turned off (Fig. 48(b)), the wall surface changes to hydrophobic, the forces are reversed.

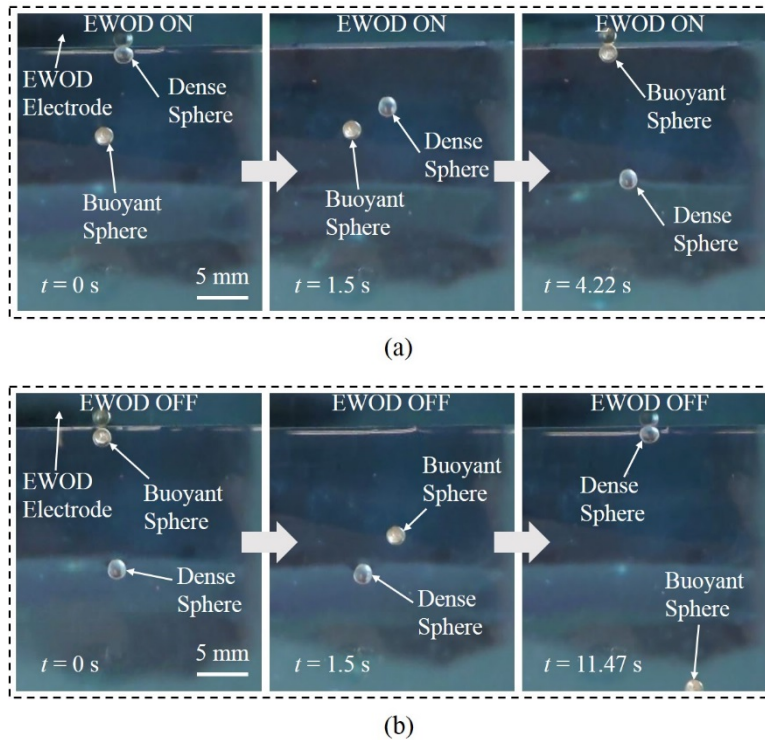


Figure 48. Experimental results for EWOD-assisted Cheerios effect. (a) When EWOD is ON, buoyant sphere is attracted but dense sphere is repelled; (b) When EWOD is OFF, buoyant sphere is repelled but dense sphere is attracted.

The EWOD electrode can also be installed on the floating objects, as shown in Fig. 49. An EWOD electrode and a ground electrode are installed on the sidewall of the boat and at the bottom of the water container separately. In Figs. 49(a) and 49(b), wall surface is hydrophobic ($\theta_w > 90^\circ$ and $\psi_w < 0$). Initially the surface of EWOD electrode is hydrophobic ($\theta_w > 90^\circ$). If the sidewall of the floating object is assumed to be vertical to the horizontal free surface, the slope angle of the EWOD surface is negative ($\psi_w < 0$). As a result, the boat is attracted toward the wall (Fig. 49(a)). When the electrical signal is applied, the EWOD surface becomes hydrophilic ($\psi_w > 0$). The floating object is repelled against the wall (Fig. 49(b)). An opposite case is shown in Figs. 49(c) and 49(d). The wall surface is hydrophilic ($\theta_w < 90^\circ$ and $\psi_w > 0$), so the force is repulsive at first and becomes attractive when EWOD in turned on.

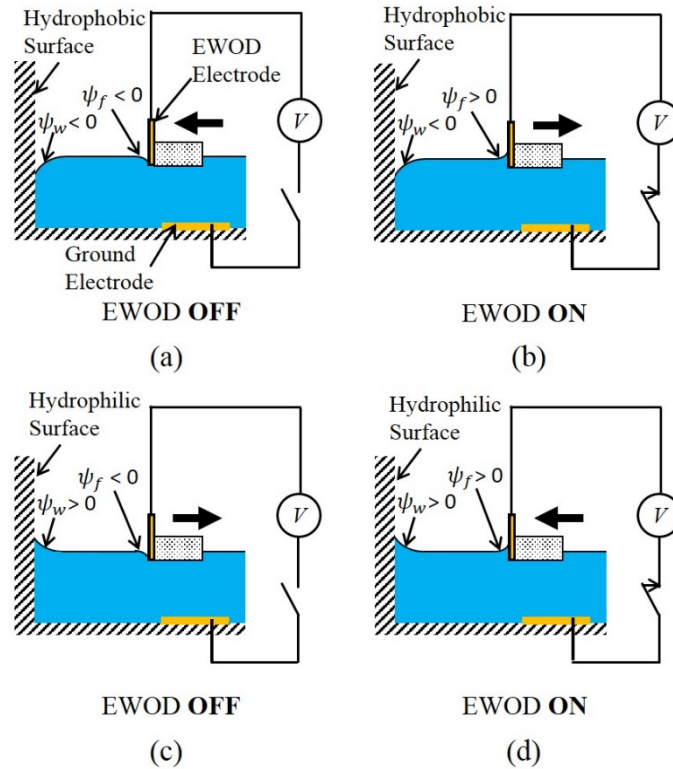


Figure 49. Sketch of EWOD-assisted Cheerios effect with an EWOD electrode installed on the floating object. (a) & (b) Hydrophobic vertical wall. (a) EWOD is OFF; (b) EWOD is ON. (c) & (d) Hydrophilic vertical wall. (c) EWOD is OFF; (d) EWOD is ON.

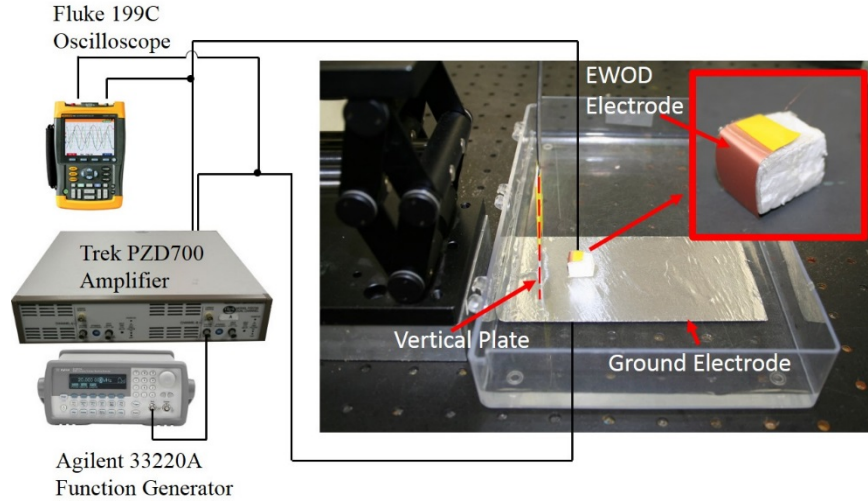


Figure 50. Experimental setup of EWOD-assisted cheerios effect propulsion with an EWOD electrode installed on the boat. The red dashed line shows the vertical wall. An aluminum foil is attached at the bottom of the container as the ground electrode. The inset shows a floating boat used in the experiment. An EWOD electrode is attached at one sidewall of the boat. A thin copper wire ($30\ \mu\text{m}$ in diameter) is used as connection wire.

Figure 50 shows the experimental setup of EWOD-assisted cheerios effect with an EWOD electrode installed on the boat. A foam boat with dimensions of $15\ (\text{L}) \times 10\ (\text{W}) \times 10\ (\text{H})\ \text{mm}^3$ is prepared. An EWOD electrode, which is same with those introduced in AC EWOD propulsion, is glued on one sidewall of the boat. Total weight of boat with EWOD electrode is about $0.1\ \text{g}$. An aluminum foil is attached at the bottom of the container as the ground electrode. A thin copper wire ($30\ \mu\text{m}$ in diameter) is used as connection wire to minimize mechanical disturbance. Figure 51 shows the experimental verification of Fig 50. $120\ \text{V}_{\text{DC}}$ is applied to the EWOD system. The vertical wall in Figs. 51(a) and 51(b) is hydrophobic ($\psi_w < 0$). The boat is attracted toward the wall when EWOD signal is off, while it's repelled against the wall when EWOD is on. The wall surface in Figs. 51(c) and 51(d) is hydrophilic ($\psi_w > 0$), and the force is reversed (i.e. repulsive when EWOD is off and attractive when EWOD is on).

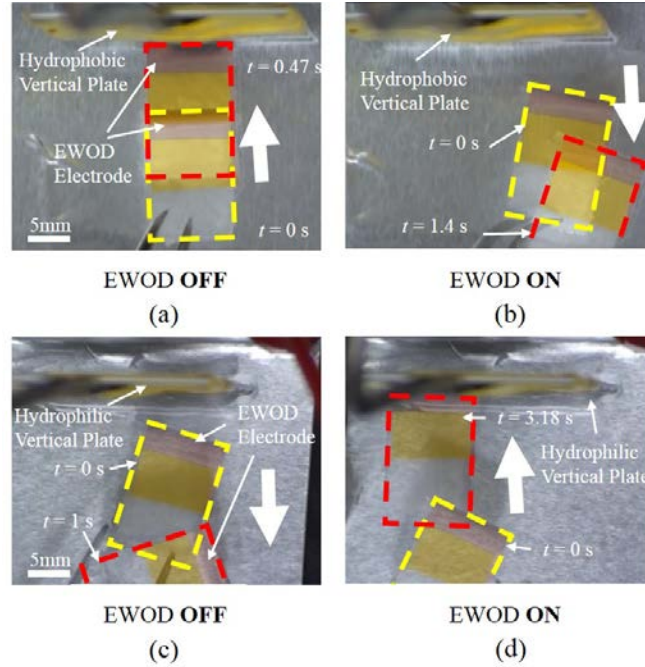


Figure 51. Experimental results for the EWOD-assisted cheerios effect propulsion with an EWOD electrode installed on the boat. (a) & (b) Hydrophobic vertical wall ($\theta_w > 90^\circ$). (a) EWOD is OFF; (b) EWOD is ON. (c) & (d) Hydrophilic vertical wall ($\theta_w < 90^\circ$). (c) EWOD is OFF; (d) EWOD is ON. Yellow dashed line represents initial position while red dashed line is ending position. Thick white arrow indicates floating object moving direction.

3.2.2 EWOD-assisted propulsion

It has been shown in Fig. 47 through Fig. 51 that a floating object can be manipulated by implementing EWOD to the Cheerios effect. However, by simply toggling the EWOD signal with a single EWOD electrode, the motion of floating objects is limited to movement toward or far away from the sidewall, as shown in Fig. 52(a). In other words, no continuous motion can be achieved. In order to realize continuous motions, Fig. 52(b) shows a modified propulsion method in a small channel. When a pair of EWOD electrodes (one in the left wall and the other in the right wall) are activated, the surfaces of electrodes change from hydrophobic to hydrophilic. As a result,

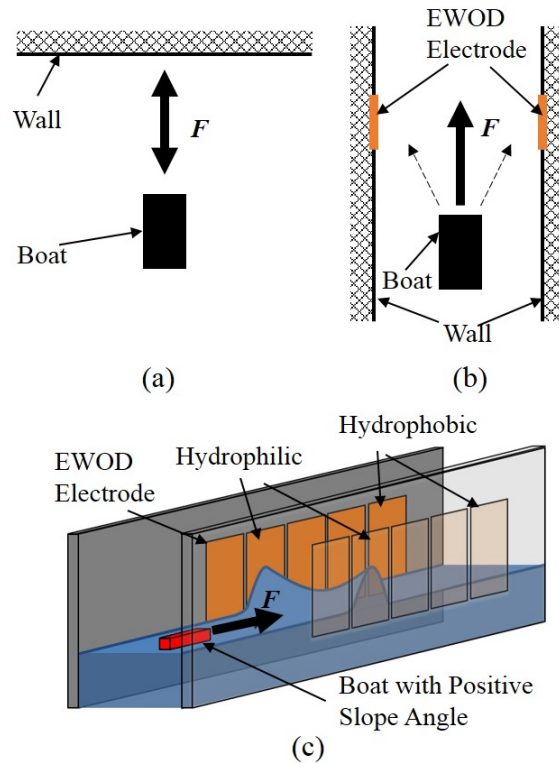


Figure 52. Comparison of Cheerios effect propulsion methods. (a) Boat is attracted toward or repelled against the wall; (b) Boat propulsion in a small channel; (c) 3-D sketch of EWOD-assisted Cheerios effect continuous propulsion. In (b) and (c), the boats have positive slope angles.

the adjacent free surface is distorted and elevated. The distorted interface simulates the wall effect in Figs. 47 and 48 and generates a pulling force on the floating object with a positive slope angle. Due to symmetry, the lateral forces on the object from two sidewalls are cancelled out. Only a net force on the object is toward the elevated interface, so the object is propelled along the channel path. Figure 52(c) shows a 3-D construction of cheerios effect propulsion in a small channel. When an array of EWOD electrodes is attached to each of two vertical sidewalls and partially immersed in water, by shifting the EWOD activation from one pair to the next pair, a continuous movement can be realized.

It's worth mentioning that the sidewalls of the boat in Figs. 52(b) and 52(c) need to have positive slope angles. At the initial state, the surfaces of EWOD electrodes are hydrophobic, repulsive forces from both sides of the channel act on the boat and are cancelled out, so the boat can align itself along the channel direction and stay in the center of the channel. When EWOD electrodes are activated, no lateral net force is generated, so the boat still maintains the position in the center. However, if the boat sidewalls have negative slope angles, forces from sidewalls change to be attractive. There exists an equilibrium point in the center of the channel but it is not stable. So the boat is easily attracted toward either of the sidewalls.

Figure 53 shows the floating object with positive slope angle is propelled in the 15-mm wide channel with two arrays of EWOD electrodes (5 mm width). The boat is made of foam material. Flexible Cu EWOD electrodes are prepared similarly with those introduced in Fig. 13. EWOD electrodes and all channel sidewalls were coated with Teflon to be initially hydrophobic, so the object with positive slope angle automatically aligns and stays in the middle of the channel. A bare aluminum foil acting as the ground electrode is attached to the bottom of the channel. Upon

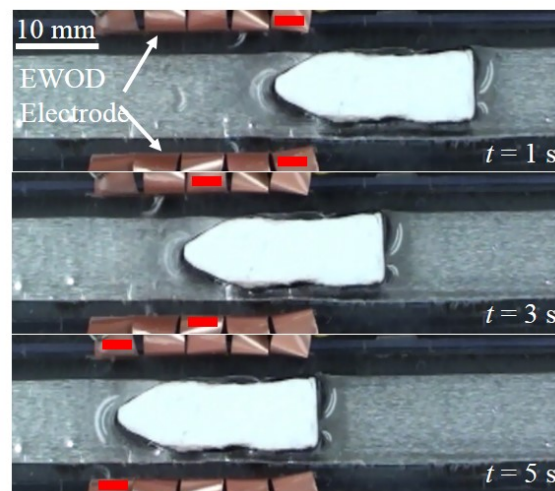


Figure 53. Boat with positive slope angle propelling in a 15 mm wide channel. Pairs of electrodes were activated sequentially from right to left with duration of 1 s. Red bars indicate the activated EWOD electrodes.

shifting activation of EWOD electrode pairs to the left (160 V_{DC} EWOD voltage) with duration of 1 s, the object is step-by-step propelled to the left. A sequential signal is provided by a microcontroller (ATMEL ATtiny24A) and relays (Panasonic AQW614EH).

It's well-known as capillary action or capillarity that when the two walls are sufficiently close, the menisci at each wall may interact with each other. The channel width in Fig. 53 is much larger than the capillary length for the water-air interface (2.7 mm). In order to confirm this principle in scales comparable to or smaller than the capillary length, two arrays of smaller EWOD electrodes (1.5 mm width) are micro-fabricated on a SiO₂ substrate and an ITO glass separately (Fig. 54). The transparent ITO electrodes allow us to visualize motions of objects from the sides. For the SiO₂ wafer, a thin layer of Al is sputter-coated on the SiO₂ substrate. Photoresist (AZ®P4210) is spin-coated on the top. After exposure to UV light, unwanted photoresist and Al are removed by an alkaline based developer simultaneously. As a result, the traditional acid wet etching process is not needed. For the ITO glass, 18% HCl is used to etch the conductive ITO layer after the standard photolithography process. A 2.5 μm thick Parylene layer is coated as the EWOD

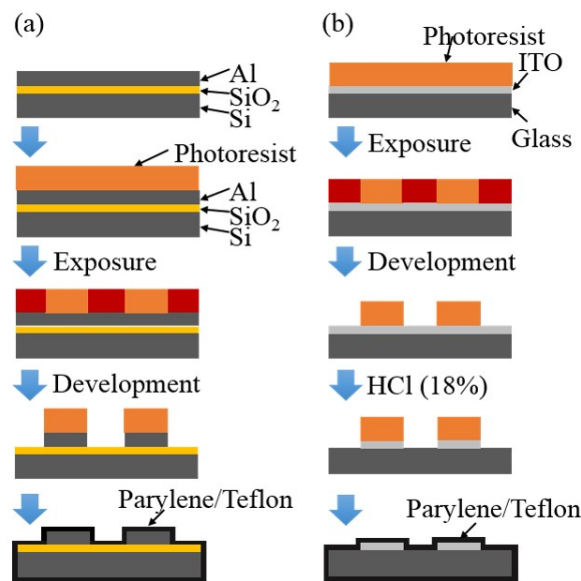


Figure 54. Fabrication process flows for EWOD electrodes on (a) SiO₂ chip; (b) ITO glass chip.

dielectric layer after the photoresist is removed in both chips. Tapes are used to cover and protect the soldering area during the parylene coating process. Because it is necessary for some portion of the soldering area to be immersed in water, silicone is used to cover the soldering area as an insulating layer to avoid any electrical short after the soldering process. After micro-fabrication and the soldering process, two arrays of EWOD electrodes are partially immersed into water vertically and aligned to form a small channel. A ground electrode is attached to the bottom of the water tank (Not shown in Fig. 55). The channel width can be adjusted by a linear traversing stage.

In Fig. 55, the spacing between the two arrays is reduced to 3 mm, which is comparable to the capillary length of the water-air interface. The floating object is made of foam material and

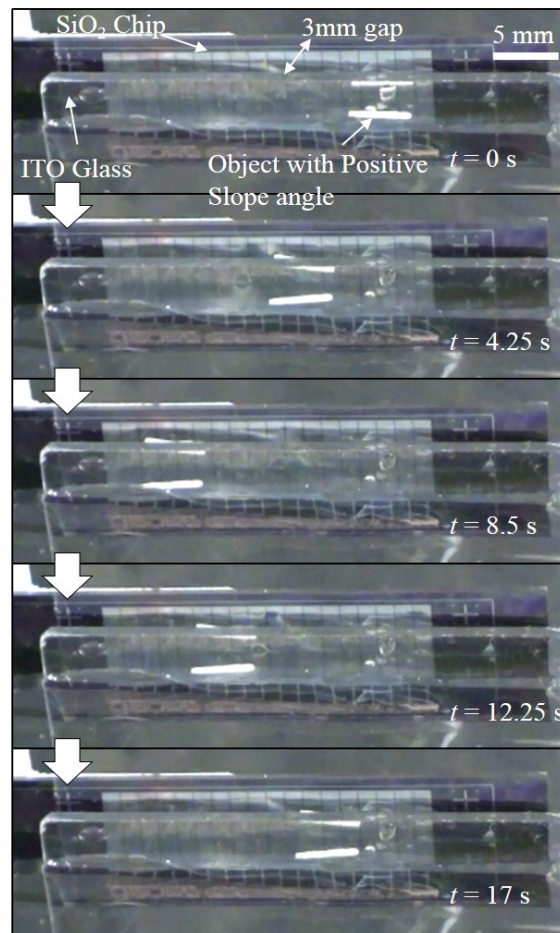


Figure 55. Boat with positive slope angle propelling in two directions in a small channel with microchips. Duration of activation was 0.5 s for each pair of electrodes.

measured at $5.4 \text{ (L)} \times 0.8 \text{ (W)} \times 0.8 \text{ (H)} \text{ mm}^3$. Sequential images (perspective views in Fig. 55) show that the object is moved left first and then right with synchronization with the electrode activation shifts (80 V_{DC} EWOD voltage with duration of 0.5 s).

Finally, a rotational motion is achieved by arranging 10 mm wide EWOD electrodes along the circular path (Fig. 56, 24 mm in radius). The ground electrode that is made of Al foil is attached to the bottom of the circular container. Two foam objects with a positive slope angle are connected by a rod and held in the center. As activations of diagonal electrode pairs are shifted clockwise ($100 \text{ V}_{\text{DC}}$ EWOD voltage with duration of 1.5 s), the net tangential force is generated and pulls and rotates the floating objects. This can be applied to floating micro motors.

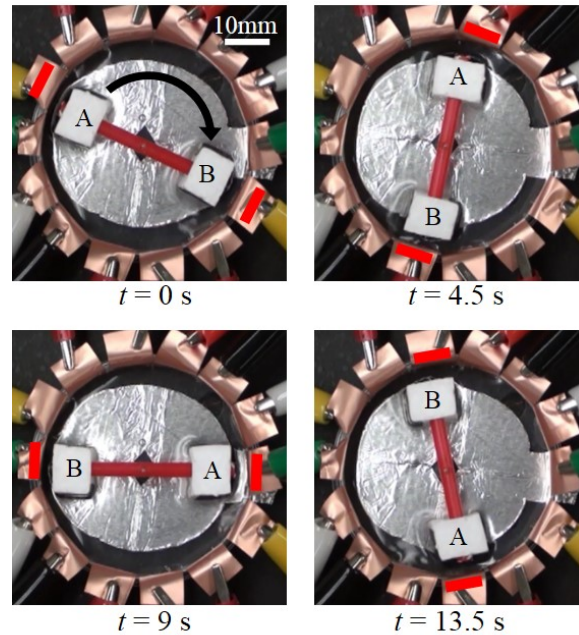


Figure 56. Rotation in a 24 mm radius circular container. Pairs of diagonal electrodes were activated clockwise with duration of 1.5 s . White bars indicate the activated EWOD electrodes.

3.3 DIELECTROWETTING-ASSISTED CHEERIOS EFFECT

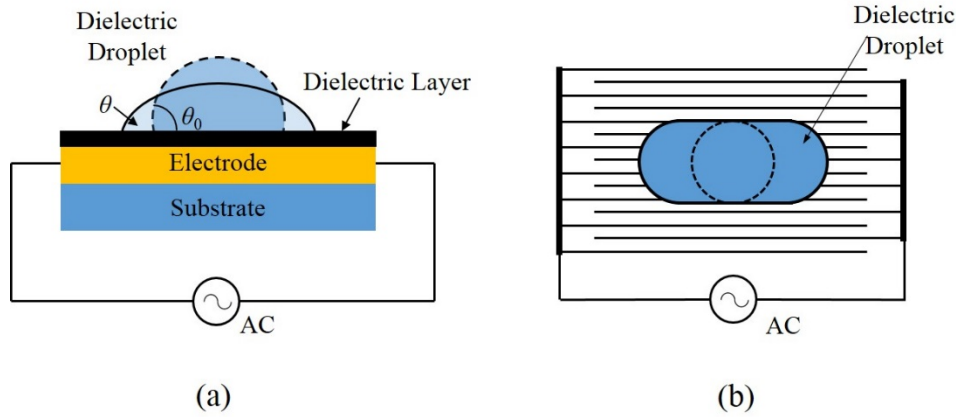


Figure 57. Sketch of dielectrowetting setup. (a) Side view; (b) Top view. Dashed line represents droplet original shape; solid line denotes droplet shape after actuation.

The electrowetting method works well with conductive liquids but is not directly applicable for non-conductive (dielectric) liquids since electrowetting is mainly effective for conductive liquids. In order to manipulate the contact angle of dielectric liquids, another method is needed. McHale *et al.* [113, 114] reported a contact angle manipulation method of dielectric liquid by using interdigitated electrodes and an AC input of high frequency. Dielectrowetting has the advantages of wide contact angle manipulation range and low degree of contact angle hysteresis. Figure 57 shows a sketch of the side view and top view of a typical dielectrowetting setup. When an AC input is applied to the dielectrowetting electrodes, the contact angle θ_0 will decrease to θ and the droplet will spread on the electrode surface along the electrode direction. The droplet will return to its initial shape when the input signal is removed.

Figure 58(a) shows the fabrication flow of dielectrowetting electrodes. A thin, flexible sheet with a Cu layer of 9 μm in thickness (DuPont Pyralux® flexible Cu product) is patterned by standard lithography and a wet etching process and is then coated with 3 μm of Parylene layer for

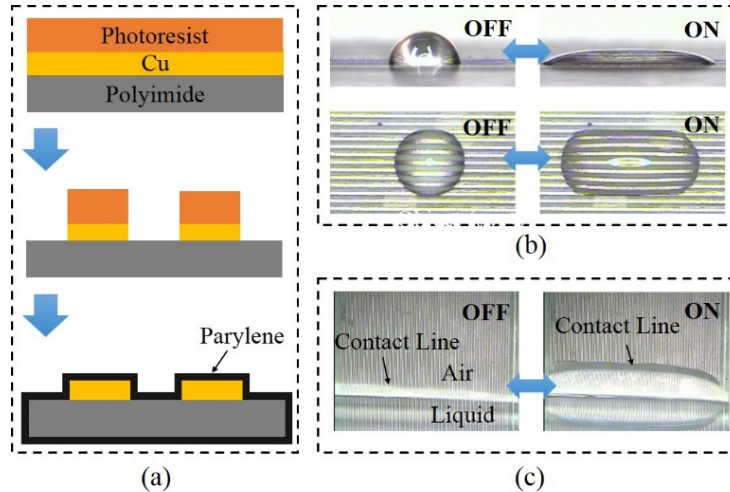


Figure 58. (a) Fabrication process flow of dielectrowetting electrodes; (b) Side and top view images of droplet actuated by dielectrowetting ($V = 300 \text{ V}_{\text{RMS}}$, $f = 10 \text{ kHz}$); (c) Contact line climbs vertically submerged dielectrowetting electrodes ($V = 300 \text{ V}_{\text{RMS}}$, $f = 10 \text{ kHz}$).

the dielectric layer. Both width of and spacing between interdigitated electrodes are $75 \mu\text{m}$. On the top of the surface, a thin Teflon layer is dip-coated. Figure 58(b) shows the side view and top view of reversible spreading and contracting of the propylene carbonate droplet under $300 \text{ V}_{\text{RMS}}$ and 10 kHz AC signal. Because dielectric fluid with low viscosity is preferable for reduced flow resistance, propylene carbonate is selected for the dielectric testing fluid (its viscosity is about 20 times lower than that of 1,2 propylene glycol used in Refs. [113, 114]). The change in the contact angle is large (over 50° , even initially lyophilic), which is larger than that by typical electrowetting (about 40°). When the interdigitated dielectrowetting electrodes vertically and partially submerge in the dielectric liquid, the contact line quickly and reversibly climbs up upon dielectrowetting activation (Fig. 58(c), $300 \text{ V}_{\text{RMS}}$ and 10 kHz AC signal).

Similar to the electrowetting assisted Cheerios effect (Fig. 47), the dielectrowetting electrode can be installed on the sidewall to control the Cheerios effect. In subsection 3.1.4.1, lateral capillary force between the wall and floating sphere for fixed contact angle boundary

condition has been derived as Eqn. (3-91). The attraction and repulsion behavior between the wall and floating object is mainly determined by interface slopes near the wall (ψ_w) and floating object (ψ_f). For a vertical wall, the slope angle at the wall ψ_w equals $(90^\circ - \theta_w)$. So for lyophobic wall surface ($\theta_w > 90^\circ$), $\psi_w < 0$, but $\psi_w > 0$ for lyophilic wall surface ($\theta_w < 90^\circ$). However, for dielectric liquid, ψ_w near the vertical wall is always positive since most of dielectric fluids have contact angles of less than 90° due to the low air-liquid surface tension. In this case, the contact angle decreases to an even lower value upon dielectrowetting actuation. As a result, the sign of ψ_w cannot be reversed by dielectrowetting, so the capillary force cannot switch between attraction and repulsion. This problem is resolved by tilting the wall by angle β , as shown in Fig. 59. Now, the slope angle ψ_w becomes $(90^\circ - \theta_w - \beta)$ and can be initially negative with a proper value of β even if θ_w is less than 90° . As a result, the wall will initially repel an object with a positive slope

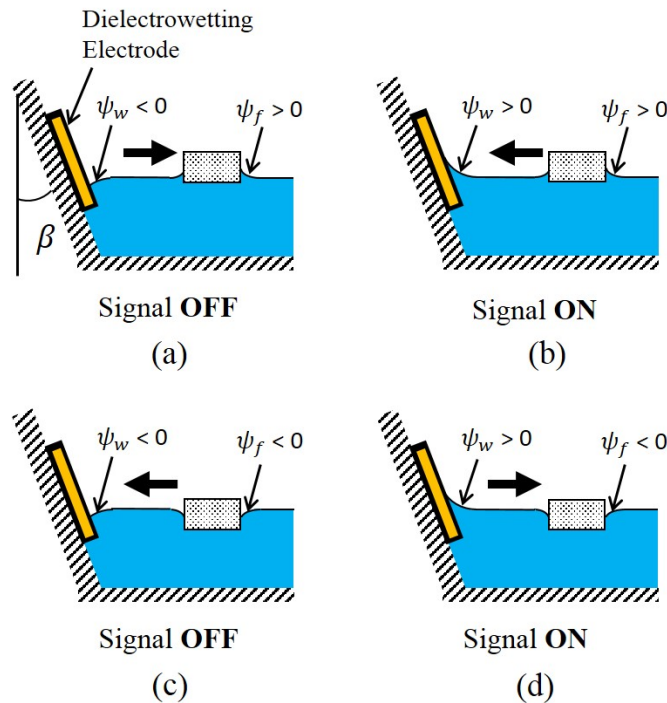


Figure 59. Sketch of dielectrowetting-assisted Cheerios effect. (a) & (b) Floating object with a positive slope angle. (a) Signal is OFF; (b) Signal is ON. (c) & (d) Floating object with a negative slope angle. (c) Signal is OFF. (d) Signal is ON.

angle ($\psi_f > 0$) (Fig. 59(a)) and attract an object with negative slope angle ($\psi_f < 0$) (Fig. 59(c)). While the dielectrowetting signal is turned on, ψ_w switches to be positive because the contact angle decreases. So the wall can attract objects with a positive slope angle ($\psi_f > 0$) (Fig. 59(b)) and repel objects with a negative slope angle ($\psi_f < 0$) (Fig. 59(d)).

Experimental verifications of Fig. 59 are shown in Fig. 60. Dielectrowetting electrodes are attached to tilted sidewalls ($\beta = 30^\circ$). When the dielectrowetting signal is off, $\psi_w < 0$, so a low-density floating object ($\rho_f \approx 0.1 \text{ g/cm}^3$) with positive meniscus slope ψ_f is initially repelled (Fig. 60(a)). When the dielectrowetting signal ($V = 300 \text{ V}_{\text{RMS}}, f = 10 \text{ kHz}$) is turned on (Fig. 60(b)), the contact angle reduces and the meniscus slope ψ_w becomes positive. As a result, the capillary force is changed to attraction. On the contrary, when a high-density floating object ($\rho_f \approx 1.5 \text{ g/cm}^3$) is used, the slope angle ψ_f is negative. The initial attraction (Fig. 60(c)) is switched to repulsion (Fig.

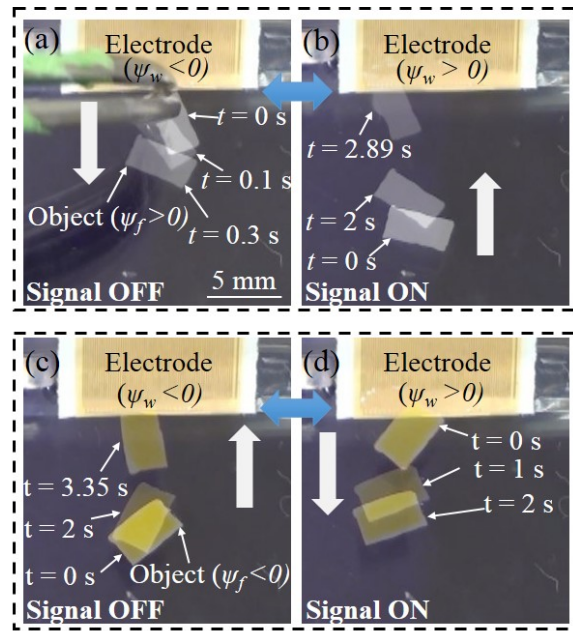


Figure 60. Experimental results for dielectrowetting-assisted Cheerios effect. Floating object with a positive slope angle is repelled when dielectrowetting signal is OFF ((a)) and is attracted when signal is ON ((b)); Floating object with a negative slope angle is attracted when signal is OFF ((c)) and is repelled when signal is ON ((d)).

60(d)) by dielectrowetting ($V = 300 \text{ V}_{\text{RMS}}$, $f = 10 \text{ kHz}$). All these switching operations are reversible.

Figures 61 and 62 show comparisons between experimental results and theoretical calculations according to Eqn. (3-91). A rectangular floating object with low density ($\rho_f \approx 0.1 \text{ g/cm}^3$) is used in the experiments. It is initially repelled by the sidewall. When dielectrowetting is turned on, the movement is recorded by a high-speed camera. Then the acceleration of the object is obtained from the second time-derivative of the displacement field. The width of the floating

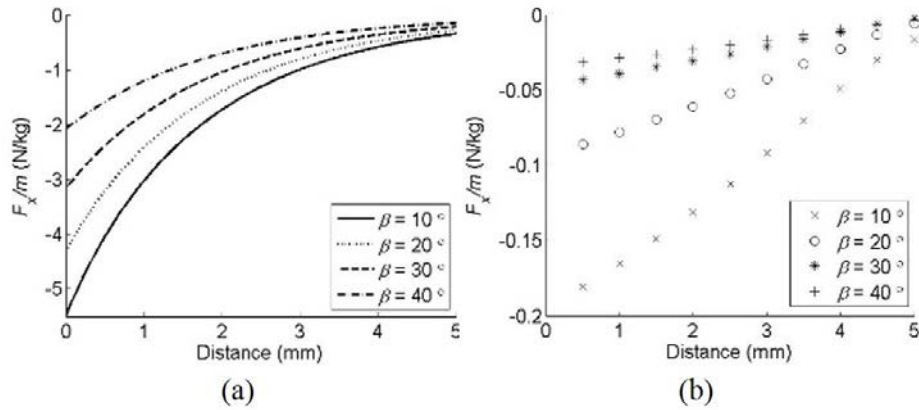


Figure 61. Force/object mass vs. tilting angle β . (a) Theoretical prediction; (b) Experimental result. ($V = 300 \text{ V}_{\text{RMS}}$, $f = 10 \text{ kHz}$)

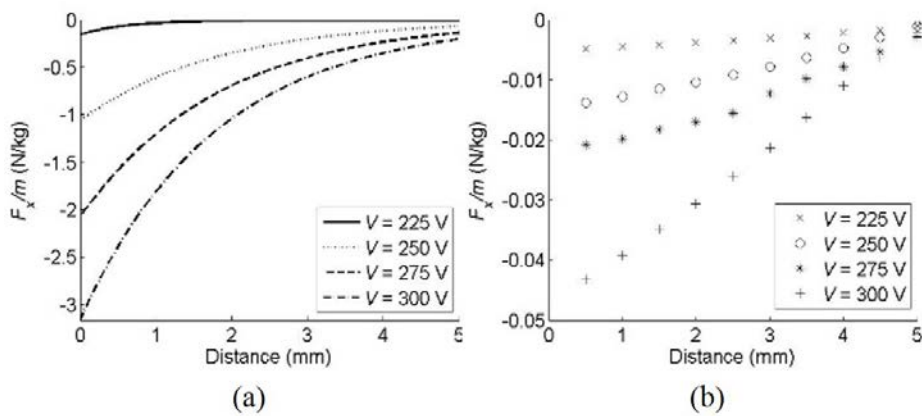


Figure 62. Force/object mass vs. applied voltage. (a) Theoretical prediction; (b) Experimental result. ($f = 10 \text{ kHz}$, $\beta = 30^\circ$)

object is measured and equivalently converted to the particle radius R_f in the theoretical calculation. The overall trend shown in Figs. 61 and 62 is that the capillary force increases when the distance decreases. As shown in Fig. 61, as the tilting angle β increases, the attraction force on the object of positive ψ_f decreases. If the tilting angle is fixed, for example $\beta = 30^\circ$ in Fig. 62, as the applied voltage increases, the lateral capillary force increases. It is easy to understand these two effects that the sum of θ_w and β is important to determine the direction of the lateral capillary force. The effect of increasing β is equivalent to the effect of increasing θ_w (which corresponds to lowering the applied voltage). The reason for quantitative discrepancy between experiment and theoretical calculation is that the theory does not take viscous drag into account. However, during the experiment, the object experiences a large viscous force due to the large contact area and high viscosity of the propylene carbonate (~ 2.5 times larger than that of water).

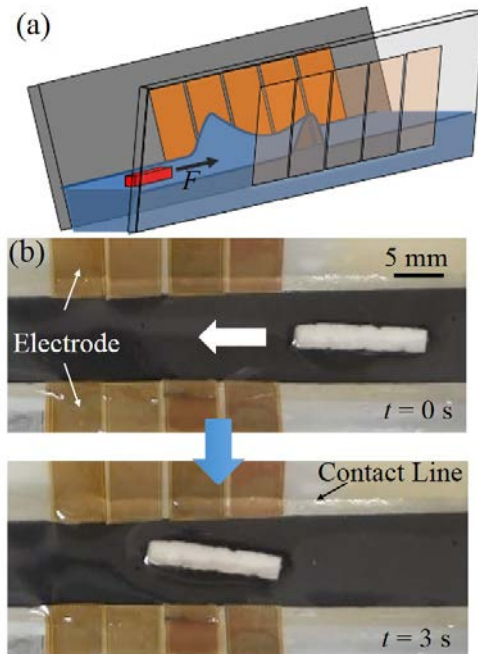


Figure 63. (a) 3-D sketch of dielectrowetting-assisted Cheerios effect continuous propulsion; (b) Top view snapshots of continuous propulsion in a channel. Pairs of electrodes are activated sequentially from right to left with duration of 0.7 s. ($V = 300 \text{ V}_{\text{RMS}}$, $f = 10 \text{ kHz}$, $\beta = 30^\circ$)

Similar to the discussion in Fig. 52, Fig. 63(a) illustrates how to continuously transport a floating object in a channel by dielectrowetting. An array of electrodes is attached to each of two tilted sidewalls. ψ_w is initially negative, so the object with positive ψ_f automatically stays in the middle of the channel due to symmetric repulsion by both sidewalls. When a pair of electrodes (one on each sidewall) is activated together, the meniscus slopes ψ_w switch from negative to positive. As a result, the distorted interface simulates the wall effect in Fig. 59 and generates a pulling force on the floating object toward the activated electrodes. Due to symmetry, the lateral forces on the object are cancelled out. Only a net force on the object is toward the elevated interface (along the channel), so the object is propelled along the channel path. By shifting the activation to the next pair, a continuous movement is achieved.

Figure 63(b) shows a low-density object ($\psi_f > 0$) is propelled in the channel with two arrays of dielectrowetting electrodes (5 mm width). Upon shifting activations of electrode pairs to the left ($V = 300 \text{ V}_{\text{RMS}}, f = 10 \text{ kHz}$) with duration of 1 s, the object is step-by-step propelled to the left. A sequential signal is provided by a microcontroller (ATMEL ATtiny24A). Relays (Panasonic AQW614EH) are used for transmitting a high AC voltage from the amplifier to the electrodes.

3.4 SUMMARY

This paper first reviewed theoretical models of the Cheerios effect for four different physical configurations. The first configuration consists of two infinite vertical plates, which is two-dimensional and the simplest. The horizontal force is not directly generated from the interfacial tension but by the hydrostatic pressure difference across the plates. The second configuration is composed of two vertical cylinders. Although this configuration needs the three-dimensional

Young-Laplace equation to describe the interface profile, it does not require the analysis for the vertical force balance. Comparisons between numerical calculation of the lateral capillary force and experimental data show that calculations predict better for the small separation than the asymptotic solution does. The third configuration is for two floating spherical particles. A linear approximation for the contact line is used, and the equation of the interface profiles derived for the two cylinders separated by a large distance is adopted to calculate the lateral capillary force between the two floating spherical particles. The last configuration is a spherical particle floating in the vicinity of a vertical wall. The expressions for the lateral capillary force for fixed contact angle or fixed contact line boundary conditions are derived with aid of the concept of the image capillary force.

In general, the capillary force between two vertical walls or between two vertical cylinders is attractive when they have similar wettability (lyophilic-lyophilic or lyophobic-lyophobic) and are repulsive when they have opposite wettability (lyophilic-lyophobic). However, this statement is not applicable for the latter two configurations (i.e., between two floating spheres and between a spherical particle and a vertical wall). The slope angle ψ is found to be the most important parameter for the capillary interaction of the latter two models. Additional parameters (for example, the size and the density of floating spheres) are crucially important to determine the slope angle of the floating particle. Because the slope angle of the vertical wall or the vertical cylinder is solely determined by the wettability of the surface, it can be found that slope angle ψ is the most important parameter for the lateral capillary force. A general rule for the Cheerios effect is that the lateral capillary force is attractive if the slope angles of both objects (two vertical walls, two vertical cylinders, two floating spheres, or a floating sphere and a wall) have the same sign,

otherwise the force is repulsive. The effect of the floating object density is particularly discussed for the latter two configurations.

In order to control the Cheerios effect, electrowetting-on-dielectric (EWOD) on the vertical plate and dielectrowetting on the tilted plate are implemented. By simply turning on/off the EWOD/dielectrowetting signal, the contact angle on the plate can be adjusted. As a result, the capillary force between the plate and the floating object can be reversed. This results in reversing of attraction and repulsion behaviors between the plate and the object. In addition, a continuous propulsion method in a small channel is then realized by both EWOD and dielectrowetting actuation. By sequentially activating micro-fabricated EWOD/dielectrowetting electrodes, linear translations of floating objects in the small scale channel are accomplished. A continuous rotational motion of the floating rod is achieved in a circular container by the EWOD method.

4.0 CONCLUSION REMARKS

This thesis reports theoretical studies and experimental proofs of the propulsion of mini-/micro-scale floating objects that propel on air-liquid interface by using AC EWOD and electrowetting-/dielectrowetting-assisted Cheerios effect. The operational concepts, device fabrications, experimental proofs, propulsion mechanisms, and parameter effects are presented throughout the chapters. The devices for propulsion are extremely simple and do not include any moving parts.

The first principle takes advantage of three-phase contact line oscillation that is activated by AC EWOD signal to propel the floating object. The oscillating free surface generates a surface wave traveling away from the electrode. The wave patterns are visualized using the Free-Surface Synthetic Schlieren (FS-SS) method, and the overall velocity field in the wake region of the floating object is visualized and measured by a PIV system. A 3-D flow field sketch is constructed based on the flow visualizations and PIV measurements, which show that near a free surface a streaming flow outgoing from the electrode is generated and below the free surface two counter-rotating spiral vortices are generated. These flows induce a momentum exchange with the floating object and generate a propulsion force. The overall flow field and trajectories of seeded particles suggest that Stokes drift is the responsible mechanism for the propulsion. The propulsion speed of the floating object highly depends on the amplitude, frequency, and shape of the EWOD signal. There exists an optimal frequency and amplitude that maximizes the propulsion speed. These behaviors can be qualitatively explained using a scaling analysis between the propulsion speed and

Stokes drift. Among the three signal shapes (sinusoidal, triangular, and modified square signals) of the same RMS value, the modified square signal shows the fastest propulsion speed throughout the tested frequency range (10 Hz ~ 1 kHz). These phenomena are also explained by the measured oscillation amplitudes and Stokes drift relations. Additionally, it is shown that a wider EWOD electrode generates a faster propelling speed. Finally, a wireless powering method for EWOD by utilizing magnetic induction is introduced. With stacked planar receiver coils and an amplitude modulated signal, a wirelessly powered EWOD propulsion is realized.

The second principle to propel floating objects is the Cheerios effect, which is also generally known as lateral capillary force. Four common physical configurations (interactions between two infinite vertical walls, two vertical circular cylinders, two spheres, and a sphere and a vertical wall) are first reviewed. Through theoretical analysis, it has been revealed that not the wettability of the surface but the slope angle of the object is the most important parameter for the Cheerios effect. For example, a lyophilic object does not necessarily attract another lyophilic object. A general rule for this effect is that the lateral capillary force is attractive if the slope angles of the interacting objects have the same sign, otherwise the force is repulsive. In addition to the surface wettability, the size and the density of floating spheres are also important for the slope angle. With aid of EWOD, the effects of the surface wettability and the density of floating spheres are experimentally illustrated. Active control of the Cheerios effect is achieved by implementing EWOD and dielectrowetting methods to adjust the surface wettability. By toggling the electrical signal, the floating objects can be attracted or repelled by the sidewall. A linear translation of floating objects in a small channel is proposed and realized. By sequentially activating micro-fabricated EWOD/dielectrowetting electrodes on sidewalls, floating object can be linearly

propelled in the small channel. A continuous rotational motion of the floating rod is achieved in a circular container by the EWOD method.

BIBLIOGRAPHY

- [1] Y.S. Song and M. Sitti, Surface-tension-driven biologically inspired water strider robots: theory and experiments, *IEEE Trans. Robot.*, **23**: 578-589 (2007).
- [2] S.K. Chung, K. Ryu, and S.K. Cho, Electrowetting propulsion of water-floating objects, *Appl. Phys. Lett.*, **95**: 014107 (2009).
- [3] O. Ozcan, H. Wang, J.D. Taylor, and Metin Sitti, Surface tension driven water strider robot using circular footpads, *IEEE Trans. Robot. Autom.*, 3799-3804, Anchorage, AK 2010.
- [4] D.L. Hu, B. Chan, and J.W. Bush, The hydrodynamics of water strider locomotion, *Nature*, **424**: 663-666 (2003).
- [5] J.W. Glasheen and T.A. McMahon, A hydrodynamic model of locomotion in the basilisk lizard, *Nature*, **380**: 340-342 (1996).
- [6] R. Baudoin, La physico-chimie des surfaces dans la vie des Arthropodes aeriens des miroirs d'eau, des rivages marins et lacustres et de la zone intercotidale, *Bull. Biol. France Belg.*, **89**: 16-164 (1955).
- [7] S.T. Hsieh, Three-dimensional hindlimb kinematics of water running in the plumed basilisk lizard (*Basiliscus plumifrons*), *J. Exp. Biol.*, **206**: 4363-4377 (2003).
- [8] S.T. Hsieh and G.V. Lauder, Running on water: Three-dimensional force generation by basilisk lizards, *Proc. Natl. Acad. Sci.*, **101**: 16784-16788 (2004).
- [9] J.W. Glasheen and T.A. McMahon, Size-dependence of water-running ability in basilisk lizards (*Basiliscus basiliscus*), *J. Exp. Biol.*, **199**: 2611-2618 (1996).
- [10] M. Dickinson, Animal locomotion: how to walk on water, *Nature*, **424**: 621-622 (2003).
- [11] X. Gao and L. Jiang, Biophysics: water-repellent legs of water striders, *Nature*, **432**: 36 (2004).
- [12] X.Q. Feng, X. Gao, Z. Wu, L. Jiang, and Q.S. Zheng, Superior water repellency of water strider legs with hierarchical structures: experiments and analysis, *Langmuir*, **23**: 4892-4896 (2007).

- [13] Y. Su, B. Ji, Y. Huang, and K.C. Hwang, Nature's design of hierarchical superhydrophobic surfaces of a water strider for low adhesion and low-energy dissipation, *Langmuir*, **26**: 18926-18937 (2010).
- [14] X.Y. Ji, J.W. Wang, and X.Q. Feng, Role of flexibility in the water repellency of water strider legs: Theory and experiment, *Phys. Rev. E*, **85**: 021607 (2012).
- [15] R.B. Suter, G.E. Stratton, and P.R. Miller, Taxonomic variation among spiders in the ability to repel water: surface adhesion and hair density, *J. Arachnology*, **32**: 11-21 (2004).
- [16] M. Prakash and J.W.M. Bush, Interfacial propulsion by directional adhesion, *INT. J. NONLINEAR MECH.*, **46**: 607-615 (2011).
- [17] M.A. Caponigro and C.H. Eriksen, Surface film locomotion by the water strider, *Gerris remigis* Say, *AM. MIDL. NAT.*, **95**: 268-278 (1976).
- [18] O. Bühler, Impulsive fluid forcing and water strider locomotion, *J. Fluid Mech.*, **573**: 211-236 (2007).
- [19] P. Gao and J.J. Feng, A numerical investigation of the propulsion of water walkers, *J. Fluid Mech.*, **668**: 363-383 (2011).
- [20] D.L. HU and J.W.M. BUSH, The hydrodynamics of water-walking arthropods, *J. Fluid Mech.*, **644**: 5-33 (2010).
- [21] R.B. Suter and H. Wildman, Locomotion on the water surface: hydrodynamic constraints on rowing velocity require a gait change, *J. Exp. Biol.*, **202 (Pt 20)**: 2771-2785 (1999).
- [22] R.B. Suter and J. Gruenwald, Predator avoidance on the water surface? Kinematics and efficacy of vertical jumping by *Dolomedes* (ARANEAE, PISAURIDAE), *J. Arachnology*, **28**: 201-210 (2000).
- [23] R.B. Suter, Trichobothrial mediation of an aquatic escape response: directional jumps by the fishing spider, *Dolomedes triton*, foil frog attacks, *J. Insect. Sci.*, **3**: 19 (2003).
- [24] G.S. Deshefy, 'Sailing' behaviour in the fishing spider, *Dolomedes triton* (Walckenaer), *Anim. Behav.*, **29**: 965-966 (1981).
- [25] R.B. Suter, Cheap transport for fishing spiders (Araneae, Pisauridae): The physics of sailing on the water surface, *J. Arachnology*, **27**: 489-496 (1999).
- [26] M. Denny, The role of gastropod pedal mucus in locomotion, *Nature*, **285**: 160-161 (1980).
- [27] S. Lee, J.W. Bush, A.E. Hosoi, and E. Lauga, Crawling beneath the free surface: Water snail locomotion, *Phys. Fluids*, **20**: 082106 (2008).
- [28] D.L. Hu and J.W. Bush, Meniscus-climbing insects, *Nature*, **437**: 733-736 (2005).

- [29] J.W. Bush and D.L. Hu, Walking on water: Biocomotion at the interface, *Annu. Rev. Fluid Mech.*, **38**: 339-369 (2006).
- [30] S. Floyd, T. Keegan, J. Palmisano, and M. Sitti, A novel water running robot inspired by basilisk lizards, in: *Proceedings of the 2006 IEEE/RSJ, International Conference on Intelligent Robots and Systems*, 5430-5436 (2006).
- [31] S. Floyd, S. Adilak, S. Ramirez, R. Rogman, and M. Sitti, Performance of different foot designs for a water running robot, *IEEE International Conference on Robotics and Automation*, 244-250 (2008).
- [32] S. Floyd and M. Sitti, Design and development of the lifting and propulsion mechanism for a biologically inspired water runner robot, *IEEE Trans. Robot.*, **24**: 698-709 (2008).
- [33] H.S. Park, S. Floyd, and M. Sitti, Dynamic modeling and analysis of pitch motion of a basilisk lizard inspired quadruped robot running on water, *IEEE International Conference on Robotics and Automation*, 2655-2660 (2009).
- [34] H.S. Park, S. Floyd, and M. Sitti, Dynamic modeling of a basilisk lizard inspired quadruped robot running on water, *IEEE/RSJ International Conference on Intelligent Robots and Systems*, 3101-3107, 2008.
- [35] H.S. Park, S. Floyd, and M. Sitti, Roll and pitch motion analysis of a biologically inspired quadruped water runner robot, *Int. J. Robot. Res.*, **29**: 1281-1297 (2010).
- [36] X. Zhang, J. Zhao, Q. Zhu, N. Chen, M. Zhang, and Q. Pan, Bioinspired aquatic microrobot capable of walking on water surface like a water strider, *ACS Appl. Mater. Inter.*, **3**: 2630-2636 (2011).
- [37] S.H. Suhr, Y.S. Song, S.J. Lee, and M. Sitti, Biologically inspired water strider robot, *Robotics Science and Systems I*, MIT, Boston 2005.
- [38] D.L. Hu, M. Prakash, B. Chan, and J.W.M. Bush, Water-walking devices, *Exp. Fluids*, **43**: 769-778 (2007).
- [39] H. Takonobu, K. Kodaira, and H. Takeda, Water strider's muscle arrangement-based robot, *IEEE/RSJ International Conference on Intelligent Robots and Systems*, 1754-1759, 2005.
- [40] Y.S. Song and M. Sitti, STRIDE: A highly maneuverable and non-tethered water strider robot, *IEEE International Conference on Robotics and Automation*, 980-984 (2007).
- [41] K. Suzuki, H. Takanobu, K. Noya, H. Koike, and H. Miura, Water strider robots with microfabricated hydrophobic legs, *Proceedings of the 2007 IEEE/RSJ, International Conference on Intelligent Robots and Systems*, 590-595 (2007).
- [42] L. Wu, Z. Lian, H. Yuan, S. Wang, and G. Yang, A non-tethered telecontrollable water strider robot prototype, *International Conference on Intelligent Control and Information Processing*, 792-797 (2010).

- [43] L. Wu, Z. Lian, G. Yang, and M. Ceccarelli, Water Dancer II-a: a Non-tethered Telecontrollable Water Strider Robot, *Int. J. Adv. Robot. Sy.*, **8**: 10-17 (2011).
- [44] B. Shin, H.-Y. Kim, and K.-J. Cho, Towards a biologically inspired small-scale water jumping robot, *Proceedings of the 2nd Biennial IEEE/RAS-EMBS International Conference on Biomedical Robotics and Biomechanics*, 127-131 (2008).
- [45] C. Luo, H. Li, and X. Liu, Propulsion of microboats using isopropyl alcohol as a propellant, *J. Micromech. Microeng.*, **18**: 067002 (2008).
- [46] N.J. Suematsu, Y. Miyahara, Y. Matsuda, and S. Nakata, Self-motion of a benzoquinone disk coupled with a redox reaction, *J. Phys. Chem. C*, **114**: 13340-13343 (2010).
- [47] E. Hendaro and Y.B. Gianchandani, Marangoni-driven micromotor in liquid medium, *Solid-State Sensors, Actuators and Microsystems Conference (TRANSDUCERS), 2011 16th International*, 246-249, 2011.
- [48] J.M. Won, J.H. Lee, K.H. Lee, K. Rhee, and S.K. Chung, Propulsion of water-floating objects by acoustically oscillating microbubbles, *Int. J. Precis. Eng. Manuf.*, **12**: 577-580 (2011).
- [49] Y. Mita, Y. Li, M. Kubota, S. Morishita, W. Parkes, L.I. Haworth, B.W. Flynn, J.G. Terry, T.-B. Tang, A.D. Ruthven, S. Smith, and A.J. Walton, Demonstration of a wireless driven MEMS pond skater that uses EWOD technology, *Solid-State Electron.*, **53**: 798-802 (2009).
- [50] M.G. Lippmann, Relations entre les phénomènes électriques et capillaires, *Ann. Chim. Phys. Fluids*, **5**: 494-549 (1875).
- [51] B. Berge, Electrocapillarity and wetting of insulator films by water, *Comptes rendus de l'Académie des Sciences, Séries II*, **317**: 157-163 (1993).
- [52] M. Vallet, B. Berge, and L. Vovelle, Electrowetting of water and aqueous solutions on poly(ethylene terephthalate) insulating films, *Polymer*, **37**: 2465-2470 (1996).
- [53] S.H. Ko, H. Lee, and K.H. Kang, Hydrodynamic flows in electrowetting, *Langmuir*, **24**: 1094-101 (2008).
- [54] J.S. Hong, S.H. Ko, K.H. Kang, and I.S. Kang, A numerical investigation on AC electrowetting of a droplet, *Microfluid Nanofluid*, **5**: 263-271 (2008).
- [55] D. Klarman, D. Andelman, and M. Urbakh, A model of electrowetting, reversed electrowetting, and contact angle saturation, *Langmuir*, **27**: 6031-41 (2011).
- [56] M. Vallet, B. Berge, and L. Vovelle, Electrowetting of water and aqueous solutions on poly(ethylene terephthalate) insulating films, *Polymer*, **37**: 2465-2470 (1996).

- [57] M. Vallet, M. Vallade, and B. Berge, Limiting phenomena for the spreading of water on polymer films by electrowetting, *Eur. Phys. J. B*, **11**: 583-591 (1999).
- [58] Y. Higashiyama, T. Yamada, and T. Sugimoto, Vibration of water droplet located on a hydrophobic sheet under the tangential ac field, *Conf. Rec. IEEE-IAS Annu. Meeting*, 1825–1830 (1999).
- [59] J.M. Oh, S.H. Ko, and K.H. Kang, Shape Oscillation of a drop in ac electrowetting, *Langmuir*, **24**: 8379-86 (2008).
- [60] F. Li and F. Mugele, How to make sticky surfaces slippery: Contact angle hysteresis in electrowetting with alternating voltage, *Appl. Phys. Lett.*, **92**: 244108 (2008).
- [61] D.J.C.M.t. Mannelje, C.U. Murade, D.v.d. Ende, and F. Mugele, Electrically assisted drop sliding on inclined planes, *Appl. Phys. Lett.*, **98**: 014102 (2011).
- [62] R. Miraghaie, J.D. Sterling, and A. Nadim, Shape Oscillation and Internal Mixing in Sessile Liquid Drops Using Electrowetting-on-Dielectric (EWOD), *Nanotech*, **2**: 610-613 (2006).
- [63] F. Mugele, J.C. Baret, and D. Steinhauser, Microfluidic mixing through electrowetting-induced droplet oscillations, *Appl. Phys. Lett.*, **88**: 204106 (2006).
- [64] R. Malk, Y. Fouillet, and L. Davoustb, Rotating flow within a droplet actuated with AC EWOD, *Sensors and Actuators B*, **154**: 191-198 (2011).
- [65] F. Mugele, A. Staicu, R. Bakker, and D. van den Ende, Capillary Stokes drift: a new driving mechanism for mixing in AC-electrowetting, *Lab Chip*, **11**: 2011-6 (2011).
- [66] H. Lee, S. Yun, S.H. Ko, and K.H. Kang, An electrohydrodynamic flow in ac electrowetting, *Biomicrofluidics*, **3**: 44113 (2009).
- [67] P. Garcia-Sanchez, A. Ramos, and F. Mugele, Electrothermally driven flows in ac electrowetting, *Phys. Rev. E*, **81**: 015303 (2010).
- [68] S.K. Chung, Y. Zhao, U.-C. Yi, and S.K. Cho, Micro Bubble Fluidics by EWOD and Ultrasonic Excitation for Micro Bubble Tweezers, *MEMS IEEE 20th International Conference*, 31-34, 2007.
- [69] S.H. Ko, Seung Jun Lee, and K.H. Kang, A synthetic jet produced by electrowetting-driven bubble oscillations in aqueous solution, *Appl. Phys. Lett.*, **94**: 194102-3 (2009).
- [70] F. Moisy, M. Rabaud, and K. Salsac, A synthetic Schlieren method for the measurement of the topography of a liquid interface, *Exp. Fluids*, **46**: 1021-1036 (2009).
- [71] L.M. Hocking, Waves produced by a vertically oscillating plate, *J. Fluid Mech.*, **179**: 267-281 (1987).

- [72] R. Ramshankar, D. Berlin, and J.P. Gollub, Transport by capillary waves. Part I. Particle trajectories, *Phys. Fluids*, **2**: 1955-1965 (1990).
- [73] O.N. Mesquita, S. Kane, and J.P. Gollub, Transport by capillary waves: Fluctuating Stokes drift, *Phys. Rev. A*, **45**: 3700-3705 (1992).
- [74] O.M. Phillips, *The dynamics of the upper ocean*, 2nd edition, Cambridge University Press, Cambridge U.K. (1977).
- [75] A.D.D. Craik, *Wave interactions and fluid flows*, Cambridge University Press, Cambridge U.K. (1985).
- [76] S.A. Thorpe, Langmuir circulation, *Annu. Rev. Fluid Mech.*, **36**: 55-79 (2004).
- [77] A.E. Tejada-Martínez, I. Akkerman, and Y. Bazilevs, Large-eddy simulation of shallow water Langmuir turbulence using isogeometric analysis and the residual-based variational multiscale method, *J. Appl. Mech.*, **79**: 010909 (2011).
- [78] P.K. Kundu, I.M. Cohen, and D.R. Dowling, *Fluid Mechanics, 5th ed.*, Elsevier, Amsterdam (2011).
- [79] J. Billingham and A.C. King, *Wave motion*, Cambridge University Press, Cambridge (2000).
- [80] P. Sen and C.J. Kim, Capillary spreading dynamics of electrowetted sessile droplets in air, *Langmuir*, **25**: 4302-5 (2009).
- [81] M.G. Pollack, R.B. Fair, and A.D. Shenderov, Electrowetting-based actuation of liquid droplets for microfluidic applications, *Appl. Phys. Lett.*, **77**: 1725-1726 (2000).
- [82] S.K. Cho, H. Moon, and C.J. Kim, Creating, transporting, cutting, and merging liquid droplets by electrowetting-based actuation for digital microfluidic circuits, *J. Microelectromech. Syst.*, **12**: 70-80 (2003).
- [83] S.H. BYUN and S.K. CHO, Electrowetting-on-Dielectric by Wireless Powering, *Heat Transfer Eng.*, **34**: 140-150 (2012).
- [84] S.H. Byun, M.-G. Yoon, and S.K. Cho, WIRELESS EWOD (ELECTROWETTING-ON-DIELECTRIC) DEVICE USING PLANAR COILS, *16th International Conference on Miniaturized Systems for Chemistry and Life Sciences*, 344-346, Okinawa, Japan 2012.
- [85] M.G. Yoon, S.H. Byun, and S.K. Cho, Inherent amplitude demodulation of an AC-EWOD (electrowetting on dielectric) droplet, *Lab Chip*, **13**: 662-8 (2013).
- [86] D. Vella and L. Mahadevan, The "Cheerios effect", *Am. J. Phys.*, **73**: 817-825 (2005).
- [87] J. Walker, *The Flying Circus of Physics*, second edition, Wiley, New York (2007).

- [88] J. Yuan and S.K. Cho, Bio-inspired micro/mini propulsion at air-water interface: A review, *J. Mech. Sci. Technol.*, **26**: 3761-3768 (2012).
- [89] S. Biswas and L.T. Drzal, A novel approach to create a highly ordered monolayer film of graphene nanosheets at the liquid-liquid interface, *Nano Lett.*, **9**: 167-172 (2009).
- [90] N. Bowden, F.A. Arias, T. Deng, and G.M. Whitesides, Self-assembly of microscale objects at a liquid/liquid interface through lateral capillary forces, *Langmuir*, **17**: 1757-1765 (2001).
- [91] N. Bowden, A. Terfort, J. Carbeck, and G.M. Whitesides, Self-assembly of mesoscale objects into ordered two-dimensional arrays, *Science*, **276**: 233-235 (1997).
- [92] G.K. Batchelor, *An Introduction to Fluid Dynamics*, Cambridge University Press, Cambridge, U.K. (1967).
- [93] D.J. Campbell, E.R. Freidinger, J.M. Hastings, and M.K. Querns, Spontaneous assembly of soda straws, *J. Chem. Educ.*, **79**: 201-202 (2002).
- [94] J.C. Berg, *An Introduction to Interfaces & Colloids: The Bridge to Nanoscience*, World Scientific, Singapore (2009).
- [95] B.V. Derjaguin and V.M. Starov, Capillary interaction between solid bodies, *Colloid J. USSR (Engl. Transl.)*, **39**: 383-386 (1977).
- [96] P.A. Kralchevsky, V.N. Paunov, I.B. Ivanov, and K. Nagayama, Capillary meniscus interactions between colloidal particles attached to a liquid-fluid interface, *J. Colloid Interface Sci.*, **151**: 79-94 (1992).
- [97] P.A. Kralchevsky, V.N. Paunov, N.D. Denkov, I.B. Ivanov, and K. Nagayama, Energetical and force approaches to the capillary interactions between particles attached to a liquid-fluid interface, *J. Colloid Interface Sci.*, **155**: 420-437 (1993).
- [98] M.M. Nicolson, The interaction between floating particles, in: *Mathematical Proceedings of the Cambridge Philosophical Society*, 288-295 (1949).
- [99] D.Y.C. Chan, J.D. Henry Jr., and L.R. White, The Interaction of colloidal particles collected at fluid interfaces, *J. Colloid Interface Sci.*, **79**: 410-418 (1981).
- [100] O.D. Velev, N.D. Denkov, V.N. Paunov, P.A. Kralchevsky, and K. Nagayama, Direct measurement of lateral capillary forces, *Langmuir*, **9**: 3702-3709 (1993).
- [101] C.D. Dushkin, P.A. Kralchevsky, H. Yoshimura, and K. Nagayama, Lateral capillary forces measured by torsion microbalance, *Phys. Rev. Lett.*, **75**: 3454-3457 (1995).
- [102] P.A. Kralchevsky, V.N. Paunov, N.D. Denkov, and K. Nagayama, Capillary image forces: I. Theory, *J. Colloid Interface Sci.*, **167**: 47-65 (1994).

- [103] O.D. Velev, N.D. Denkov, V.N. Paunov, P.A. Kralchevsky, and K. Nagayama, Capillary image forces: II. Experiment, *J. Colloid Interface Sci.*, **167**: 66-73 (1994).
- [104] E.H. Mansfield, H.R. Sepangi, and E.A. Eastwood, Equilibrium and mutual attraction or repulsion of objects supported by surface tension, *Phil. Trans. R. Soc. Lond. A*, **355**: 869-919 (1997).
- [105] W.A. Gifford and L.E. Scriven, On the attraction of floating particles, *Chem. Eng. Sci.*, **26**: 287-297 (1971).
- [106] C. Allain and M. Cloitre, Interaction between particles trapped at fluid interfaces, I. Exact and asymptotic solutions for the force between horizontal cylinders, *J. Colloid Interface Sci.*, **157**: 261-268 (1993).
- [107] H.N. Dixit and G.M. Homsy, Capillary effects on floating cylindrical particles, *Phys. Fluids*, **24**: 122102 (2012).
- [108] R. Finn, *Equilibrium Capillary Surfaces*, Springer, New York (1986).
- [109] G.A. Korn and T.M. Korn, *Mathematical Handbook for Scientists and Engineers*, McGraw-Hill, New York (1968).
- [110] I.B. Ivanov, P.A. Kralchevsky, and A.D. Nikolov, Film and line tension effects on the attachment of particles to an interface: I. conditions for mechanical equilibrium of fluid and solid particles at a fluid interface, *J. Colloid Interface Sci.*, **112**: 97-107 (1986).
- [111] P.A. Kralchevsky and K. Nagayama, *Particles at Fluid Interfaces and Membranes: Attachment of Colloid Particles and Proteins to Interfaces and Formation of Two-Dimensional Arrays*, Elsevier, Amsterdam, Netherlands (2001).
- [112] C.D. Dushkin, P.A. Kralchevsky, V.N. Paunov, H. Yoshimura, and K. Nagayama, Torsion balance for measurement of capillary immersion forces, *Langmuir*, **12**: 641-651 (1996).
- [113] G. McHale, C.V. Brown, M.I. Newton, G.G. Wells, and N. Sampara, Dielectrowetting driven spreading of droplets, *Phys. Rev. Lett.*, **107**: 186101 (2011).
- [114] G. McHale, C.V. Brown, and N. Sampara, Voltage-induced spreading and superspreading of liquids, *Nat. Commun.*, **4**: 1605 (2013).